UNIVERSITÀ DEGLI STUDI DI TRIESTE

XXXV CICLO DEL DOTTORATO DI RICERCA IN

NANOTECNOLOGIE

OPERANDO SOFT X-RAY ABSORPTION SPECTROSCOPY APPLICATIONS FOR THE INVESTIGATION OF SURFACE REACTIVITY OF HETEROGENEOUS CATALYSTS FOR METHANOL VALORIZATION

SETTORE scientifico-disciplinare: **FIS/03**

DOTTORANDA
SILVIA MAURI

COORDINATORE
PROF. ALBERTO MORGANTE Alberto Morgante

SUPERVISORE DI TESI
DR. PIERO TORELLI

ANNO ACCADEMICO 2021/2022

"If you only read the books that everyone else is reading, you can only think what everyone else is thinking."

Haruki Murakami

Norvegian Wood

Contents

Chapter 1

Abstract

Given the urgency of achieving the forthcoming zero emission targets, the research of green fuels and efficient catalysts able to easily convert them in other valuable compounds is fundamental. The work presented in this thesis is focused on the application of an innovative spectroscopic technique, the *operando* Soft X-Rays NEXAFS spectroscopy, in order to investigate the surface reactivity of heterogeneous catalysts. In fact, it is well known the importance that *operando* characterizations have acquired in recent years, allowing to study a material at its working conditions. Since the technique requires the use of Synchrotron Radiation and a specific experimental setup, all the measurements reported in this thesis have been performed exploiting a home made reaction cell developed at the APE-HE beamline, at Elettra Synchrotron (Trieste). In this thesis work, we investigated the possibility of coupling the *operando* NEXAFS technique with other *in situ* spectroscopies, together with standard *ex situ* characterizations and computational simulations. This multitechnique approach allowed to extract the maximum potential of the technique, addressing its role as a key tool in the optic of speeding up the design of efficient heterogeneous catalysts.

The catalytic reactions investigated in this thesis are focused on methanol valorization, given its great potential in numerous applications related to the energy

transition. In detail, we focused our first investigation on methanol production through the direct partial oxidation of methane, catalysed by a CeO_2/CuO composite synthesized using a scalable and green milling process. We exploited the combination of *in situ* DRIFT and *operando* Soft X-Ray NEXAFS spectroscopies to monitor at the same time the electronic structure modifications occurring at the catalyst surface and the adsorbates evolution during the different reaction steps. The *operando* analysis of the Cu $L_{2,3}$ and Ce $M_{4,5}$ edges during the catalyst thermal activation allowed us to detect a charge transfer from Ce^{3+} surface sites to Cu^{2+} atoms, resulting in the formation of reactive sites close to the CeO_2/CuO interface. When the sample was exposed to CH_4 at 250°C and at a pressure of 1 bar, a $Cu^{2+} \rightarrow Cu^{+}$ reduction was observed, indicating that the catalyst is able to activate the methane molecule. At the same time, DRIFT spectra shown the formation of methoxy and formate species, that are products of methane activation on the surface. Adding an oxidizing agent (O_2), Cu^{+} sites were re-oxidized to Cu^{2+}, together with the disappearing of the methoxy and formate related structures in the DRIFT spectra. The results indicated the reversibility of the chemical modifications occurring at the catalyst surface. During the *operando* NEXAFS experiment, the reaction products were monitored with an online micro-GC: the main products observed during the reaction were CO_2, H_2O, CH_2O and CH_3OH, indicating that total and partial oxidation of methane were occurring. As a comparison, an equivalent experiment has been conducted on a similar CeO_2/CuO catalyst synthetized with a conventional impregnation method. In this case, no spectroscopic modification were observed with both NEXAFS and DRIFT techniques, confirming that the synthetic method used is crucial in creating specific active sites for methane activation and oxidation. The experimental results have been validated through DFT calculations, which confirmed that when CuO and CeO_2 surfaces merge during the synthesis, a net charge transfer from Ce to Cu atoms occurs in proximity of the $CeO_2 - CuO$ interface.

Another promising route to valorize methanol is represented by its catalytic decomposition to syngas mixture ($H_2 + CO$), whose reaction mechanism was investigated in the second part of the thesis. Indeed, one major challenge for this reaction is related to the quest for stable, cost-effective, and selective catalysts operating below 400 °C. In the present study, we illustrate a surface reactivity study of a Ni_3Sn_4 catalyst working at 250 °C, by combining density functional theory (DFT), *operando* NEXAFS at ambient pressure, *in situ* XPS and high-resolution transmission electron microscopy (HR-TEM). For Ni_3Sn_4, we discovered that the catalytic reaction is driven by surface tin-oxide phases, able to protect the underlying Ni atoms from irreversible chemical modifications, increasing the catalyst durability. Moreover, exploiting the online micro-GC connected to the *operando* NEXAFS reaction cell and by comparing the results with a Ni_3Sn_2 compound, we found that Sn content plays a key role in enhancing the H_2 selectivity, with respect to secondary products such as CO_2. These findings open new perspectives for the engineering of scalable and low-cost catalysts for hydrogen production.

Chapter 2

Introduction

2.1 Overview

The fight against climate change is set to be one, if not the most, important challenge of this century for the global community. Since the famous Kyoto protocol of 1997, the continuous global temperature rise due to greenhouse gas emissions has led to the definition, during the last Conference of the Parties (COP) held in Glasgow in 2022, of the commitment by the entire international community to maintain the average temperature increase below 2°C (and possibly below 1.5°C)[1]. In order to achieve this goal, countries are committed to reach the net zero emissions target by 2050 (i.e. producing less carbon than we take out of the atmosphere). Up to now, around 70% of the world economy is covered by net zero targets. The European Union, with the Next Generation Eu Project[2] has defined the goal of cutting 55% of greenhouse gas emissions by 2030. Among the strategies reported to achieve this ambitious objective, in addition to the direct use of renewable energy and electrification, there is also the need to resort to renewable hydrogen to replace fossil fuels in some carbon-intensive industrial processes. As for transport, in 2015 only 6% of the cars were powered by renewable sources; the goal is to reach the 24% by 2030, through the further development and diffusion of electric vehicles, parallel to the implementation of advanced biofuels and other renewable or low-C (or high-H) fuels. In this context, catalysis has acquired a fundamental importance, becoming a key component for the pursuit of the aforementioned objectives. A catalytic material is able to change the path of a chemical reaction without itself being expended. In an ideal catalyst, a small amount of material can convert a large quantity of reactants under milder conditions than would be required by the stoichiometric reaction pathway. Moreover, a catalyst can drive the reaction path to specific reaction products, the so-called selectivity[3]. The branch of heterogeneous catalysis aims to develop efficient materials able to catalyse chemical reactions occurring in a phase different from the one of the catalyst (for example a solid state material catalysing a gas phase reaction). The major advantage of heterogeneous catalysis compared to homogeneous catalysis is the fact that the catalyst, being in a phase different from that of the reactants, can be recovered and reused much more easily[4]. At the moment, the way to establish an efficient protocol for the design of functional, industrially scalable and cost-effective catalysts is still a long and winding one[5]. The objective of this thesis work was, in generic terms, devolved to the finalization of an efficient strategy that allows to identify promising catalysts not only on pure empirical bases (catalytic efficiency tests), but also from the nanostructural and electronic structure point of view. In fact, we believe that this approach, described in detail in the next sections, allows to speed up and implement enormously the identification and design of new efficient catalysts, since knowing the fundamental physical and chemical properties that underlie the efficient functioning of a catalyst takes to the natural consequence of understanding how to improve its performance. Up to date, one of the most advanced tool to pursue this goal is to exploit one or more so-called *operando* techniques, which aim to characterize a catalyst at its operating conditions, monitoring the reaction products. The developement of *operando* techniques started in the early 2000s[6], following the development of the older *in situ* techniques. In the *in situ* characterizations, the catalysts are studied under conditions similar to those of the reaction, but without the detection of the reaction products. While technical considerations will be done in detail in the next chapters, Fig.2.1(a) allow to highlight the importance that *operando* techniques are acquiring over time. The scientific articles containing the keywords "operando" and "catalyst" have experienced a surge in the last seven years. At the same time, articles referred to *in situ* characterization, that started to grow much earlier, in recent years have slowed down, while maintaining the lead in terms of absolute numbers. The observation of these trends highlights two important factors: firstly, the impressive instrumental development of the recent years due to the outstanding progress of information technologies, but also in the field of materials engeneering. Secondly, the fact that the scientific community have realized the importance and great potential that *operando* techniques are bringing to catalysis. Moreover, looking at Fig.2.1(b), the weight that X-Ray Absorption Spectroscopy (XAS) is acquiring in the context of the *operando* techniques is undeniable; in 2022, the articles containing the keyword "XAS" and "operando" has reached almost the 25% of the total *operando* studies [1].

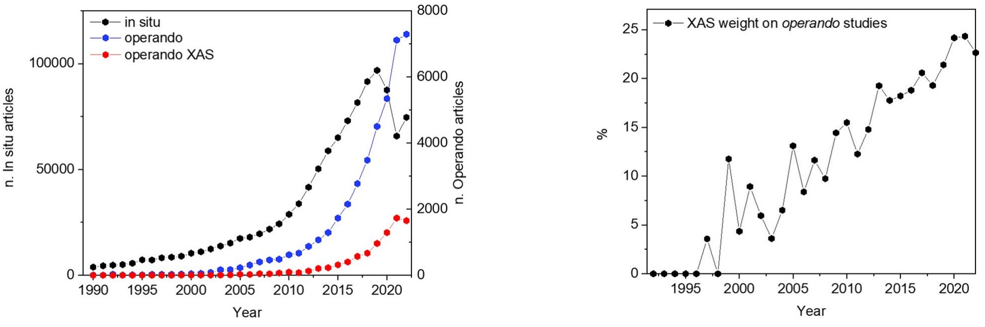

(a)

(b)

Figure 2.1: a) Growth over time of scientific articles containing the following keywords: "in situ" and "catalyst" (black), "operando" and "catalyst" (blue), "operando" and "catalyst" and "XAS" (red) . b) Growth over time of the % of articles with the keywords "operando" and "catalyst" and "XAS" with respect to the total "operando" studies. The % indicates the weight that *operando* XAS is acquiring over time. Source: Google Scholar[7].

---

[1] It must be said that this calculation could be slightly overestimated, since it also takes into account the articles where *ex situ* XAS spectroscopy is combined with other *operando* techniques.

2.2 New challenges for heterogeneous catalysis: knowledge-based approach based on *operando* techniques

The advantages that heterogeneous catalysis has brought to the everyday life and to industrial processes in the last 100 years is undeniable[8,9]; on the other hand, given the complexity of the aspects ruling a catalytic process, the approach that has been given to the study of catalytic and functional materials is most often empirical. This means that a material is engineered, tested, and once its efficiency and/or selectivity is ascertained, it is characterized in order to unveil its kinetic, chemical and structural properties. This approach not only makes the development of new catalysts very slow, but also leads to the impossibility of directing research on catalysis towards a so-called *knowledge-based* method[5]. The first scientist who tried to apply a "molecular oriented" approach by exploiting spectroscopic techniques was the engineer Michel Boudart[10–13]. Unfortunately, until a few years ago the technologies necessary to develop a similar strategy were not yet at the forefront or were very expensive, and for this reason the current chemical industry is still largely dependent on the empiric approach. Given the global urgency mentioned in the overview and since nowadays state-of-the-art technologies allow it, it becomes necessary to speed up the process of identifying the optimal structure of efficient catalysts, modifying the aforementioned empirical approach. We are nowadays at the beginning of this change of perspective, which probably needs further technological development to be implemented efficiently, both experimentally and theoretically.

One of the main problems facing the investigation of a catalyst and what makes it much more complex to study than for example a semiconductor, is that the functioning of the latter depends solely on the variation of its electronic structure, while the chemical and geometric structure remains mostly static. In the case of a catalyst, the chemical, geometric and electronic structure of the system is affected at each catalytic cycle. Most of the time, these modifications are reversible, and thus very difficult to detect with standard characterization techniques. If the changes were irreversible, the catalyst would be deactivated and therefore its functioning would no longer be the same as in the previous cycle. These are some of the most important aspects that led to the need to develop techniques where the catalyst can be monitored in its working conditions (*operando* techniques). Such investigations combine an analysis of geometric or electronic structure with the simultaneous proof of catalytic activity. Moreover, the combination of more *operando* techniques would take to a stronger evidence for the correctness of the described chemical reaction. The possibility of exploiting these techniques and combining them together would make it possible to bridge the gap between the two schools of thought described above, the "empirical" and the "knowledge-based"[5,14,15]. This thesis works aims to show some applications in which a similar gap can be filled. The adopted strategy is schematically represented in Fig.2.2.

As shown in the figure, the process is iterative; the starting point is the synthesis of a material, based on the desired catalytic reaction. Literature is fundamental at this stage: in fact, the studies that have already been performed on similar materials are an important guide for the definition of a target catalyst. Equally important are the theoretical simulations carried out before synthesis, in such a way as to be able to predict the type of structure to be obtained for a precise catalytic reaction step. Once defined the material, it is necessary to operate on different levels, which can also be performed in parallel to speed up the characterization. At this stage the *operando* techniques proved to be fundamental, because they allow, together with the classical characterization techniques (such as X-ray diffraction, or electron microscopy) and computational simulations, to define a possible reaction mechanism. The detection of reaction products in the *operando* experiments allows to directly correlate the proposed reaction mechanism to the catalytic tests results

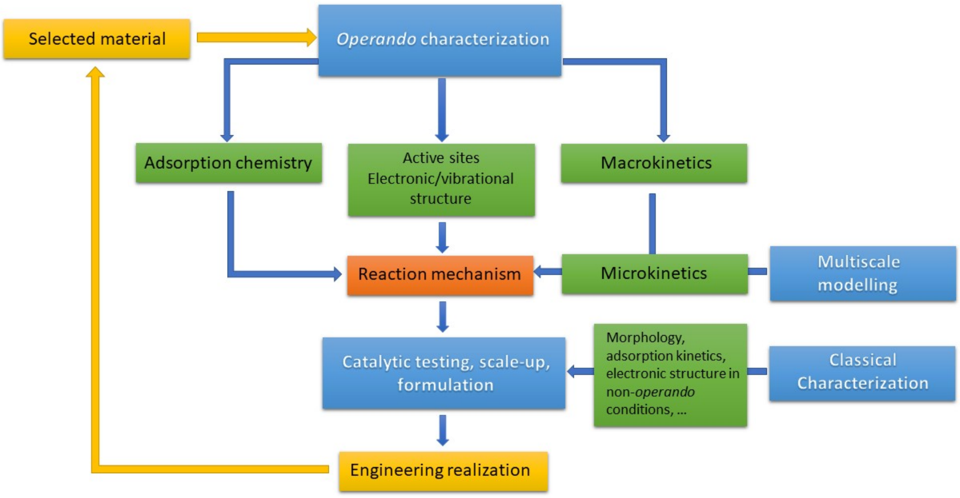

Figure 2.2: Schematic representation of the knowledge-based iterative strategy used in this thesis to investigate catalytic reactions. The scheme is inspired by Professor Schlogl's review[5]. The arrows show the iterative process that must be followed in order to fully optimize a new catalyst. Blue boxes: Experimental and theoretical tools; Green boxes: information obtained; Yellow boxes: First and last step of the optimization (being the process iterative, their direct connection is crucial); Red box: The most important step in the optimization, i.e. the definition of the catalytic reaction mechanism.

that can be conducted in parallel with dedicated setups. At the end of the overall characterization, the researcher will have a complete knowledge of the mechanisms related to a specific activity and selectivity for the chosen catalytic reaction, for a specific material; the knowledge-based study will allow to modify the starting material taking into account all the important information obtained, synthesizing a new material oriented towards a better performance of the catalyst. At this point, the pattern repeats itself. It is important to underline that the more effective the *operando* characterization is, the less times it will be necessary to repeat the process. This thesis work, with the two studies that will be presented in the results and discussion chapters, highlights the merits of this approach, but also the issues that will have to be addressed in the future to improve it. In detail, in both studies we managed to perform almost a complete iteration of the scheme reported in Fig.2.2, by combining the use of the *operando* NEXAFS setup of APE-HE beamline (described in section 3.2.1.3) with other *in situ* spectroscopies, DFT calculations and standard characterization techniques. We elucidated in both cases the catalytic reaction mechanism leading to the formation of a particular reaction product, also obtaining fundamental information regarding the relation between a specific material design and its catalytic activity and selectivity. Unfortunately, it cannot be stated that the iteration entirely concluded because we managed to obtain only semi-quantitative results, while quantitative catalytic tests have not yet been performed. This aspect could be one of the possible future instrumental developments of the *operando* NEXAFS setup of APE-HE beamline. Until this milestone is achieved, separated catalytic tests can be conducted in order to obtain quantitative information and complete an entire knowledge-based iteration.

2.3 Methanol and its leading role for the future

The two studies presented in this thesis are focused on methanol valorization. This section therefore gives an overview on the global importance that this compound assumes today, dealing with its synthesis processes and its main uses at present and for a possible future "methanol economy". A graphic representation of the economic impact of methanol is shown in Fig.2.3. Asia Pacific region is the larger consumer and producer, followed by North America; from 2018 to the projection of 2026, the market is almost tripled globally.

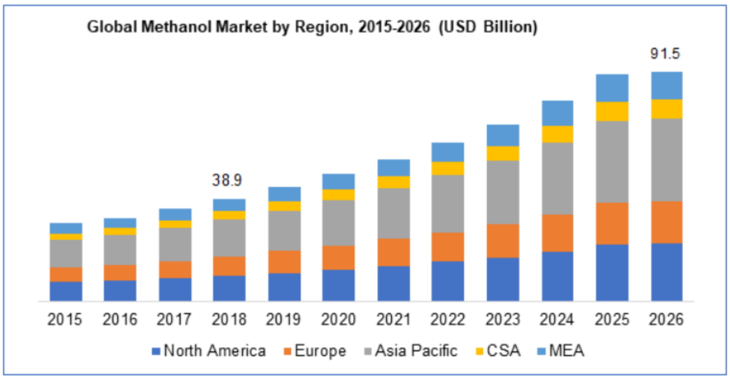

Figure 2.3: Graph reporting historical data and forecast for the 2015-2026 global methanol market[16]. *CSA* = Central and South America; *MEA* = Middle East and Africa.

Methanol is an alcohol liquid at ambient pressure and temperature. Since its boiling point is at 65°C, it can be transported and distributed through pipelines. It posesses an energy density of 22.7 MJ/kg[17], making it convenient to use as energy storage compound. To give a comparison, the Li-ion batteries have an energy density of 0.5–3.6 MJ/kg. Moreover, the growing demand for oil and gas in emerging economies and the severe shortage in oil and gas supply at economically reasonable prices is expected to affect the chemical industry in the next years. Therefore, it is necessary to think about compounds that could easily substitute classic petrochemicals, minimizing the need to upset the existing infrastructures and systems. These requirements are perfectly fullfilled by methanol. Fig.2.4 shows a scheme representing how methanol can be exploited as a chemical raw materials for industrial purposes. As it can be observed, the use of methanol as a raw chemical material mainly starts from synthesis gas (also called syngas, i.e. CO/H_2 mixture) or from a CO_2/H_2 mixture. Syngas gas plays a fundamental role in the synthesis of methanol, described in detail later in the discussion. Moreover, the double arrow in the diagram between syngas and methanol highlights that it can also be useful to convert methanol into syngas, that can be exploited for other purposes, such as hydrogen production. Concerning the chemical products obtained directly from methanol in Fig.2.4, the variety of possibilities that the compound offers is evident, revealing how important petrochemical products can be substituted by C1-based chemistry. Some of the processes reported have always been used in the chemical industry, while others are totally new. It is important to specify that all the products shown in the diagram can be obtained from both methanol and crude oil.

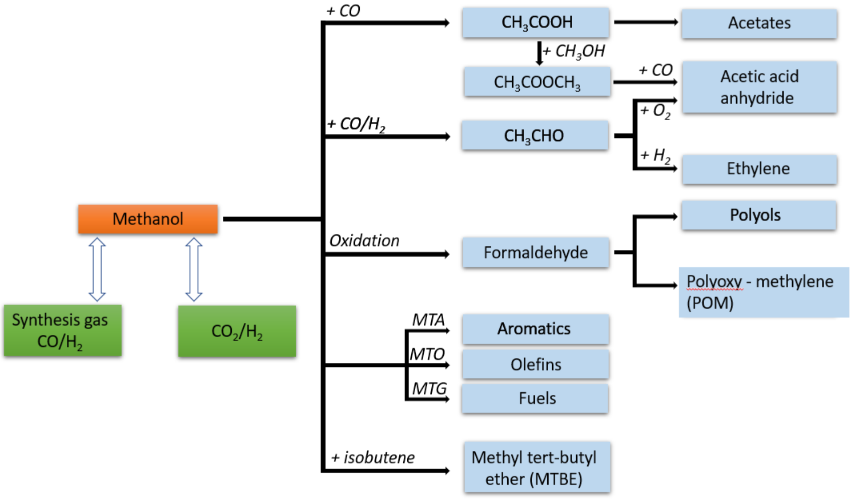

Figure 2.4: Scheme illustrating the different methanol processing as a chemistry raw material.

Despite the multiplicity of uses that we have just seen at an industrial level, the versatility of methanol allows it to be used also as an energy feedstock. These two important applications (chemical and fuel) open up the possibility of a "methanol economy"[18]. Fig.2.5 shows its schematic representation: methanol can be exploited in both chemistry and energy sectors, implying that from a single source both chemical feedstocks and combustibles for power generation can be produced at a large scale.

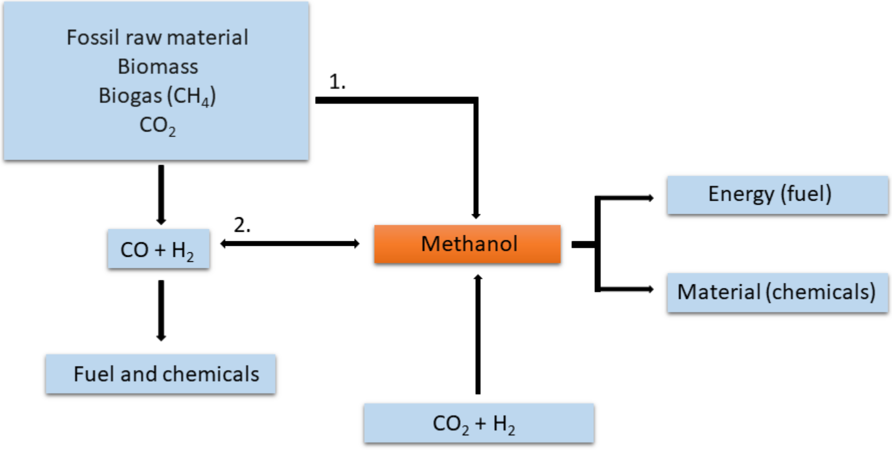

Figure 2.5: Scheme representing the main routes of a possible methanol economy[17].

At the date, the main building block for methanol production is syngas mixture, as already mentioned. Synthesis gas can be produced from any carbon containing source. Enzymatic routes for direct methanol production from biomass exist in nature (route 1. in Fig.2.5): at the industrial level they are not employed because the mechanisms underlying the cataytic paths in the enzymes are still not clearly understood; thus, efficient and selective catalysts do not exist at the moment for this reaction. The solution of this problem would fill the missing link to realistically achieve a methanol-based economy. Another alternative would be the methanol production starting from CO_2 and H_2, that would provide an unlimited feedstock and at the same time would be useful for the CO_2 emissions problem. Unfortunately, this route would require an high hydrogen demand.

This section gave an overview on the importance of methanol in the actual and future global economy. The next sections are devoted to explain in detail the two catalytic reactions investigated in this thesis work, which are the direct methane to methanol synthesis and the methanol decomposition to syngas. Indeed, the research of materials able to efficiently catalyse these reactions, represented by routes 1. and 2. respectively in Fig.2.5, would allow to easily interplay between the three main actors of the possible methanol economy (biomass, syngas and methanol), greatly facilitating the possibility of its success in the near future.

2.3.1 Direct methane to methanol partial oxidation

To date, at the industrial level there are two processes exploited for the production of liquid hydrocarbons starting from methane, namely the methane-to-gasoline and the Fischer-Tropsch synthesis. They are both two-step reactions involving firstly the production of syngas mixture, followed by its conversion to the desired product. Steam reforming of methane to syngas is an endothermic process (eq.2.1):

$$CH_4 + H_2O \rightleftharpoons CO + 3H_2 \qquad \Delta H^0_{298K} = +206.2 \quad kJmol{-}1. \tag{2.1}$$

Usually, Ni/Al_2O_3 catalyst are industrially employed, working at elevated temperatures ($>$ 800°C). The unreacted syngas can be exploited to produce methanol:

$$CO + 2H_2 \rightleftharpoons CH_3OH \qquad \Delta H^0_{298K} = -90.7 \quad kJmol{-}1. \tag{2.2}$$

This two step synthetic way to synthetize methanol starting from methane is called *indirect* route, and as it can be seen from eq.2.1 is energetically demanding. The so-called *direct* route imply the direct partial methane oxidation to methanol (DMTM), an exothermic process:

$$CH_4 + 1/2O_2 \rightleftharpoons CH_3OH \qquad \Delta H^0_{298K} = -126.2 \quad kJmol{-}1. \tag{2.3}$$

The direct route is energetically convenient and it would allow to convert and valorize a greenhouse gas in a "Waste to Wealth" process[19]. Practically, DMTM is not exploited at the industrial level, since a material that is able to catalyze the reaction efficiently has not yet been designed. This is due to two main encountered issues: the first is the activation of methane molecule on the catalyst surface. This important step is often difficult to achieve because the C-H bond in methane is the strongest in nature (440 kJ/mol), due to the perfect tetrahedral simmetry of the molecule. The second issue is that when methane is oxidized to methanol, usually the latter encounters a further oxidation to CO_2 and H_2O. This occurs because the dissociation energy of the C-H bond in methanol is lower than in methane (393 kJ/mol). A catalyst able to activate methane at the same time avoiding the over-oxidation of methanol has not been designed yet, leading to the fact that currently the active catalysts for this reaction lead to low methane conversions and selectivities.

2.3.1.1 Heterogeneous catalysts for DMTM reaction

At the state of the art, the most widely studied catalysts for the DMTM reaction in heterogeneous catalysis are based on Mo, V, Fe and Cu. Molybdenum catalysts[20] were the first to be investigated, already in the 1980s. They were considered the most active catalysts for the partial oxidation of methane until the end of the century, even if the reaction was carried out at high temperatures and pressures[21–24]. The impossibility of using these catalysts at the industrial level lay in the fact that at high temperatures (above 700°C) humidity promotes the volatility of Mo atoms, undergoing the formation of hydroxylated species in gaseous phase[25]. Vanadium based materials represented an alternative to Molybdenum catalysts[26–28]. Their utilization can lead to maximum methanol selectivities of 57%, and their difference in catalytic properties with respect to Mo-based catalyst reside in the fact that the methane total oxidation to CO_2 passes through the production of an intermediate, the formaldehyde.

More recently, Fe and Cu have been extensively employed in the design of novel catalysts for the DMTM reaction, in particular exploited in the form of oxides or as dopants in porous materials, such as zeolites or Metal Organic Frameworks

(MOFs). The idea behind the design of these materials is based on the attempt to replicate the functioning of an enzyme called methane monooxygenase (MMO), which is able to convert methane into methanol with very high selectivity and conversions, at ambient temperature[29]. There are two types of MMO enzymes (Fig. 2.6), the sMMO (soluble, containing di-iron sites), and the pMMO (particulate, containing oxo-dicopper sites).

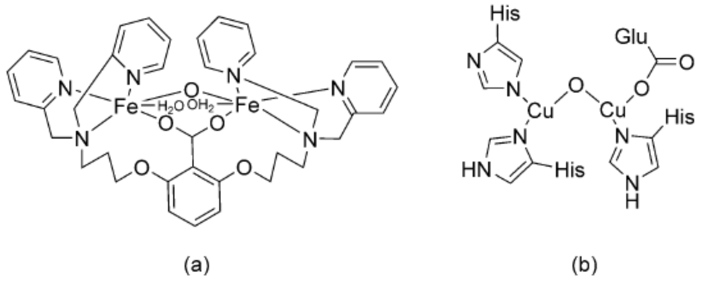

Figure 2.6: Proposed structures of the active sites in a) sMMO and b) pMMO enzymes[19].

For the sMMO, the active sites nature, the reaction mechanism and the enzyme composition have already been elucidated[30–32]; concerning the pMMO, the nature of the active sites is still debated, as for the mechanism concerning the methane activation and conversion. Looking at the catalysts performances, both Cu and Fe based zeolites are able to mimic the functioning of MMO enzymes, obtaining very high selectivities for methanol ($> 90\%$)[33–36], but with methane conversions of about 1%. A 10% methane conversion with high methanol selectivity was obtained for Fe and Cu silicalites[33]: the major drawback in this case was the utilization of H_2O_2, that is corrosive and more expensive than methanol.

Among the most innovative and recent approaches, we mention the work of Zuo et al.[37], which was the starting point of inspiration for one of the two topics that will be treated in this thesis. In this study, a model system based on CeO_2 islands deposited on a metallic Cu(111) substrate by means of pulsed laser deposition (PLD) technique has been synthesized. The obtained $CeO_2/Cu(111)$ material is a so-called *inverse* catalyst, because usually in heterogeneous catalysis metal particles are supported by oxide substrates. Inverse catalysts are synthesized in order to maximize the OMI (oxide-metal interactions)[38]. As a consequence of these interactions, a Cu_2O monolayer is formed at the interface between the oxide and the metal. The Cu_2O monolayer exposes reactive oxygen atoms able to activate the methane molecule at low temperatures (170°C) and ambient pressures, as depicted in Fig.2.7(a). Moreover, if water is predosed with a defined partial pressure, a methanol selectivity of 70% is obtained[39]. Through a combined *in situ* XPS and DFT calculation investigation, they proposed a mechanism model to explain the role of water in promoting the methanol selectivity, which consists in the H_2O dissociation on the catalyst surface, forming surface hydroxyles able to activate methane, and consequently desorbed as a CH_3OH molecule (see Fig.2.7(b)).

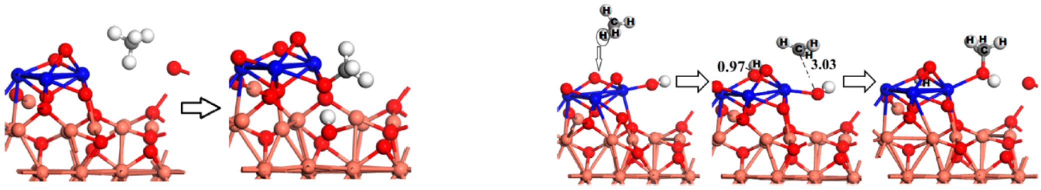

(a)

(b)

Figure 2.7: Methane activation over $CeO_2/Cu_2O/Cu(111)$ inverse catalyst a) without and b) in presence of water[37,39].

As it can be seen from Fig.2.7(a), Cu^+ atoms in the system have the important role to be the responsible of the methane deprotonation. The investigation of the role of Cu^+ as active site, formed subsequently to an interaction with another reducible oxide such as CeO_2, is assuming an important relevance in heterogeneous catalysis research[40,41], and will be deeply analyzed in the discussion of the first case study of this thesis work.

2.3.2 Methanol decomposition to Syngas

Hydrogen production from direct methanol decomposition reaction (eq.2.4) is a valuable alternative to the commonly industrially exploited steam reforming of methane reaction (eq.2.1)[42], which is strongly endothermic.

$$CH_3OH \rightleftharpoons 2H_2 + CO \qquad \Delta H^0_{298K} = +90.36 \quad kJmol{-}1. \tag{2.4}$$

Industrially, the major advantage of the methanol decomposition reaction lies in avoiding an external steam and heat source, thus reducing the operating and infrastructure costs. Methanol decomposition reaction brings to the production of the syngas ($H_2 + CO$) with a 2:1 ratio. As already introduced in Fig.2.5, the possibility to easily switch between syngas mixture and methanol would make it possible to achieve great strides forward towards a methanol-based economy: for example, it would drastically reduce the problems related to the transport of hydrogen in H_2-fuelled vehicles. Moreover, syngas can be used industrially for a wide range of applications[43], ranging from the synthesis of valuable chemicals to energy applications, for example as a fuel in Solid Oxide Fuel Cells (SOFCs)[44]. H_2 and CO can be separated in a controlled environment, in order to exploit them individually[45,46]: the produced hydrogen is widely used for ammonia synthesis; in the optic of the zero-emissions targets, hydrogen has unique applications as electrical energy storage or as a fuel in vehicles, since the only product coming from the hydrogen combustion is water[47]. Unfortunately, methanol decomposition reaction can be accompanied by a series of parallel reactions, such as Boudouard reaction (eq.2.5), methanation (eq.2.6) and reverse water-gas shift (eq.2.7). These reactions take to secondary products, namely CO_2, H_2O and C.

$$2CO \rightleftharpoons C + CO_2 \qquad \Delta H^0_{298K} = +172 \quad kJmol{-}1. \tag{2.5}$$

$$CO + 3H_2 \rightleftharpoons CH_4 + H_2O \qquad \Delta H^0_{298K} = -206 \quad kJmol{-}1. \tag{2.6}$$

$$CO_2 + H_2 \rightleftharpoons CO + H_2O \qquad \Delta H^0_{298K} = +42.1 \quad kJmol{-}1. \tag{2.7}$$

In particular, Boudouard reaction takes to the formation of C which can poison the catalyst surface, deactivating it. Hence arises the research of stable and cost-effective catalysts capable of: *i)* Decreasing the activation energy for the syngas production; *ii)* selectively favour the syngas production, suppressing the occurrence of the secondary reactions mentioned above.

2.3.2.1 Heterogeneous catalysts for methanol decomposition reaction

State-of-the-art catalysts for methanol decomposition reaction are mainly based on Cu, Pt, Pd, and Ni. In detail, Cu-based catalysts are unstable, owing to C poisoning, with the consequent fast deactivation[48, 49]. Moreover, Pt- and Pd-based electrodes, though being stable, are expensive and they could be activated only at temperatures above 400°C[50, 51]. Concerning Ni-based catalysts, they potentially can combine stability, efficient catalytic activity, and cheapness of raw materials, thus representing good candidates for industrial scale-up[52–55]. Hence, one of the major challenges regards the optimization of the catalytic activity and selectivity of Ni-based materials. In this context, intermetallic compounds (IMCs)[56–63] are particularly relevant due to their peculiar electronic structure, originated from the atomic arrangement in ordered structures, differently from ordinary closed-packed metallic compounds. Precisely, IMCs are composed of different elements located near the Zintl line (e.g., the line dividing metallic and non-metallic elements in the periodic table), whose relative ratio can be used to tune their structural, electronic, and physicochemical properties. Recently, high selectivity to H_2 and CO has been reported for IMCs with respect to the undesired secondary reactions reported in eq.2.5, 2.6 and 2.7[64, 65]. Among the various Ni-based alloys, Ni-Sn compounds deserve particular attention, considering that the incorporation of Sn atoms can be beneficial for hydrogen selectivity[64–66] and making CO adsorption energetically unfavorable, thus preventing the methanation reaction[64] and improving the catalyst durability. It must be specified that the studies reported in the literature focus the catalytic tests at temperatures > 400°C. To our knowledge, the effect produced by the addition of Sn at temperatures lower than 400°C has never been investigated from the point of view of the catalytic mechanism, reaction paths and thus selectivity to syngas. For this reason, this last point has been the object of the second part of this thesis work.

2.4 Scope of this work

The main aim of this thesis project was to apply and show the potentialities of the *knowledge-based* approach (described in detail in section 2.2) to investigate two catalytic reactions related to methanol valorization, with the common denominator residing in the use of the *operando* Soft X-ray absorption spectroscopy as main investigation tool. Exploiting the experimental setup designed at the APE-HE beamline of Elettra Synchrotron (Trieste), described in detail in section 2.2, combined with other *in situ* and *ex situ* characterization techniques and with the fundamental help of DFT calculations, we were able to obtain key information regarding the catalytic reaction mechanisms under investigation; the possibility to study the catalysts at their operating conditions allowed us to provide new tools to improve their design of the catalysts, with the final aim to achieve better catalytic performances.

We investigated the catalytic direct partial oxidation of methane to methanol reaction on a CeO_2/CuO powder composite, exploiting an innovative ball milling synthesis, which is scalable and solvent free. The aim of the synthetic approach was to reproduce a system similar to the one of Zuo et al. described in detail in section 2.3.1.1[37,39], with the main difference residing in its potential scalability at the industrial level. For the synthesis, we established a collaboration with the University of Udine (prof. Alessandro Trovarelli's group). The *operando* soft X-ray NEXAFS analysis of the Cu $L_{2,3}$ and Ce $M_{4,5}$ edges allowed us firstly to understand the electronic structure modifications occurred during the ball milling synthesis, and secondly to monitor the spectroscopic modifications occurring during the catalyst exposure to CH_4 and O_2 reagents. The use of an online micro gas chromatograph allowed to detect the reaction products, performing a complete *operando* experiment. Under the same experimental conditions, we repeated the experiment exploiting the *in situ* DRIFT technique, in order to obtain information about the different intermediate species adsorbed on the catalyst surface during the subsequent reaction steps. The DRIFT experiments have been performed at the University of Udine (Prof. Alessandro Trovarelli's group). The combination of the *operando* soft X-ray NEXAFS and the *in situ* DRIFT results allowed to obtain a clear view of the reaction mechanisms occurring on the catalyst surface during the different reaction steps. Finally, we performed DFT calculations carried out in collaboration with the group of Dr. Stefano Fabris (SISSA- CNR-IOM), in order to validate the proposed mechanism model.

The catalytic methanol decomposition to syngas is the other reaction investigated in this thesis project. In detail, we aimed to elucidate the effect that different Sn content has in Ni-Sn intermetallic compounds on the selectivity to H_2 with respect to secondary undesired products. The samples (Ni_3Sn_4 and Ni_3Sn_2) were synthetized using an innovative flux method, in collaboration with the group of prof. Antonio Politano (University of L'Aquila). In this case, we combined the *in situ* X-Ray Photoemission Spectroscopy (XPS) with *operando* soft X-ray NEXAFS technique. XPS analysis allowed to investigate the surface composition and reactivity of the Ni-Sn compounds, while the NEXAFS investigation, during which the samples were exposed to methanol at ambient pressure and at different temperatures, gave important elucidations on how methanol molecules interact differently with Ni atoms by changing the Sn content, the reaction conditions and the surface pretreatments. In this study, the online micro gas chromatograph data were analyzed with the aim to obtain a semi-quantitative comparison about the different catalysts selectivity to syngas, upon different Sn content and experimental conditions. DFT calculations (carried out by Prof. D. W. Boukhvalov, Nanjing Forestry University, College of Science) allowed to validate the data obtained experimentally and to propose a possible reaction mechanism model.

2.5 Bibliography

[1] `https://ukcop26.org/cop26-goals/`.

[2] `https://eur-lex.europa.eu/legal-content/IT/TXT/HTML/?uri=CELEX:52020DC0562&from=EN`.

[3] Robert K Grasselli and AW Sleight. *Structure-activity and selectivity relationships in heterogeneous catalysis.* Elsevier, 1991.

[4] Erica Farnetti, Roberta Di Monte, and Jan Kašpar. Homogeneous and heterogeneous catalysis. *Inorganic and bio-inorganic chemistry*, 2(6):50–86, 2009.

[5] Robert Schlögl. Heterogeneous catalysis. *Angewandte Chemie International Edition*, 54(11):3465–3520, 2015.

[6] Anisha Chakrabarti, Michael E. Ford, Daniel Gregory, Rongrong Hu, Christopher J. Keturakis, Soe Lwin, Yadan Tang, Zhou Yang, Minghui Zhu, Miguel A. Bañares, and Israel E. Wachs. A decade + of operando spectroscopy studies. *Catalysis Today*, 283:27–53, 2017. Operando V - 5th International Conference on Operando Spectroscopy, Deauville (FR) May 2015.

[7] `https://scholar.google.com/schhp?hl=it&as_sdt=0,5`.

[8] Hironori Arakawa, Michele Aresta, John N. Armor, Mark A. Barteau, Eric J. Beckman, Alexis T. Bell, John E. Bercaw, Carol Creutz, Eckhard Dinjus, David A. Dixon, Kazunari Domen, Daniel L. DuBois, Juergen Eckert, Etsuko Fujita, Dorothy H. Gibson, William A. Goddard, D. Wayne Goodman, Jay Keller, Gregory J. Kubas, Harold H. Kung, James E. Lyons, Leo E. Manzer, Tobin J. Marks, Keiji Morokuma, Kenneth M. Nicholas, Roy Periana, Lawrence Que, Jens Rostrup-Nielson, Wolfgang M. H. Sachtler, Lanny D. Schmidt, Ayusman Sen, Gabor A. Somorjai, Peter C. Stair, B. Ray Stults, and William Tumas. Catalysis research of relevance to carbon management:

progress, challenges, and opportunities. *Chemical Reviews*, 101(4):953–996, 2001. PMID: 11709862.

[9] Gabriele Centi and Siglinda Perathoner. Opportunities and prospects in the chemical recycling of carbon dioxide to fuels. *Catalysis Today*, 148(3):191–205, 2009. Special Issue of the 10th International Conference on CO2 Utilization, Tianijn, China, May 17-21, 2009.

[10] W. Nicholas Delgass and Michel Boudart. Application of Mössbauer spectroscopy to the study of adsorption and catalysis. *Catalysis Reviews*, 2(1):129–160, 1969.

[11] R.A. Dalla Betta, R.L. Garten, and M. Boudart. Infrared examination of the reversible oxidation of ferrous ions in Y zeolite. *Journal of Catalysis*, 41(1):40–45, 1976.

[12] R.A. Dalla Betta, M. Boudart, K. Foger, D.G. Löffler, and J. Sánchez-Arrieta. Cell fitted with thin Beryllium windows for X-Ray Absorption under pressures up to 14 MPa and temperatures up to 700 K. *Review of Scientific Instruments*, 55(12):1910 – 1913, 1984. Cited by: 39.

[13] M. Boudart, R.A. Dalla Betta, K. Foger, D. G. Löffler, and M. G. Samant. Study by Synchrotron Radiation of the structure of a working catalyst at high temperatures and pressures. *Science*, 228(4700):717–719, 1985.

[14] Francisco Zaera. In-situ and operando spectroscopies for the characterization of catalysts and of mechanisms of catalytic reactions. *Journal of Catalysis*, 404:900–910, 2021.

[15] Staci L. Wegener, Tobin J. Marks, and Peter C. Stair. Design strategies for the molecular level synthesis of supported catalysts. *Accounts of Chemical Research*, 45(2):206–214, 2012. PMID: 22004451.

[16] `https://www.polarismarketresearch.com/industry-analysis/methanol-market`.

[17] Arno Behr. Methanol: The basic chemical and energy feedstock of the future. Asinger's vision today. Edited by Martin Bertau, Heribert Offermanns, Ludolf Plass, Friedrich Schmidt and Hans-Jürgen Wernicke. *Angewandte Chemie International Edition*, 53(47):12674–12674, 2014.

[18] George A. Olah. Beyond oil and gas: The methanol economy. *Angewandte Chemie International Edition*, 44(18):2636–2639, 2005.

[19] Manoj Ravi, Marco Ranocchiari, and Jeroen A. van Bokhoven. The direct catalytic oxidation of methane to methanol - a critical assessment. *Angewandte Chemie International Edition*, 56(52):16464–16483, 2017.

[20] Y. Barbaux, A.R. Elamrani, E. Payen, L. Gengembre, J.P. Bonnelle, and B. Grzybowska. Silica supported Molybdena catalysts: Characterization and methane oxidation. *Applied Catalysis*, 44:117–132, 1988.

[21] M.R. Smith and U.S. Ozkan. The partial oxidation of methane to formaldehyde: Role of different crystal planes of MoO_3. *Journal of Catalysis*, 141(1):124–139, 1993.

[22] Tomomi Sugino, Ayako Kido, Naoto Azuma, Akifumi Ueno, and Yasuo Udagawa. Partial oxidation of methane on silica-supported silicomolybdic acid catalysts in an excess amount of water vapor. *Journal of Catalysis*, 190(1):118–127, 2000.

[23] Kiyoshi Otsuka and Masaharu Hatano. Boron, Phosphorus, and Alkaline earth-metal mixed oxides as active catalysts in partial oxidation of methane into Formaldehyde. *Chemistry Letters*, 21(12):2397–2400, 1992.

[24] T. Weng and Eduardo E. Wolf. Partial oxidation of methane on Mo/Sn/P silica supported catalysts. *Applied Catalysis A: General*, 96(2):383–396, 1993.

[25] T. Millner and Jenö Neugebauer. Volatility of the oxides of Tungsten and Molybdenum in the presence of water vapour. *Nature*, 163:601–602, 1949.

[26] Nicholas D. Spencer and Carmo J. Pereira. V_2O_5/SiO_2-catalyzed methane partial oxidation with molecular oxygen. *Journal of Catalysis*, 116(2):399–406, 1989.

[27] Shang Yang Chen and David Willcox. Effect of Vanadium oxide loading on the selective oxidation of methane over vanadium oxide (V_2O_5)/silica. *Industrial & Engineering Chemistry Research*, 32(4):584–587, 1993.

[28] J. A. Barbero, M. C. Alvarez, M. A. Bañares, M. A. Peña, and J. L. G. Fierro. Breakthrough in the direct conversion of methane into C1-oxygenates. *Chem. Commun.*, pages 1184–1185, 2002.

[29] AC Rosenzweig, CA Frederick, SJ Lippard, and P Nordlund. Crystal structure of a bacterial non-haem iron hydroxylase that catalyses the biological oxidation of methane. *Nature*, 366(6455):537—543, December 1993.

[30] J Colby and H Dalton. Resolution of the methane mono-oxygenase of Methylococcus capsulatus (Bath) into three components. Purification and properties of component C, a flavoprotein. *Biochemical Journal*, 171(2):461–468, 05 1978.

[31] Simone Friedle, Erwin Reisner, and Stephen J. Lippard. Current challenges of modeling diiron enzyme active sites for dioxygen activation by biomimetic synthetic complexes. *Chem. Soc. Rev.*, 39:2768–2779, 2010.

[32] Christine E. Tinberg and Stephen J. Lippard. Dioxygen activation in soluble methane monooxygenase. *Accounts of Chemical Research*, 44(4):280–288, 2011. PMID: 21391602.

[33] Ceri Hammond, Michael M. Forde, Mohd Hasbi AbRahim, Adam Thetford, Qian He, Robert L. Jenkins, Nikolaos Dimitratos, Jose A. Lopez-Sanchez,

Nicholas F. Dummer, Damien M. Murphy, Albert F. Carley, Stuart H. Taylor, David J. Willock, Eric E. Stangland, Joo Kang, Henk Hagen, Christopher J. Kiely, and Graham J. Hutchings. Direct catalytic conversion of methane to methanol in an aqueous medium by using Copper-Promoted Fe-ZSM-5. *Angewandte Chemie International Edition*, 51(21):5129–5133, 2012.

[34] Jun Xu, Robert D. Armstrong, Greg Shaw, Nicholas F. Dummer, Simon J. Freakley, Stuart H. Taylor, and Graham J. Hutchings. Continuous selective oxidation of methane to methanol over Cu- and Fe-modified ZSM-5 catalysts in a flow reactor. *Catalysis Today*, 270:93–100, 2016. C1 Catalytic Chemistry.

[35] Marijke H. Groothaert, Pieter J. Smeets, Bert F. Sels, Pierre A. Jacobs, and Robert A. Schoonheydt. Selective oxidation of methane by the Bis(-oxo)dicopper core stabilized on ZSM-5 and Mordenite zeolites. *Journal of the American Chemical Society*, 127(5):1394–1395, 2005. PMID: 15686370.

[36] Evalyn Mae Alayon, Maarten Nachtegaal, Marco Ranocchiari, and Jeroen A. van Bokhoven. Catalytic conversion of methane to methanol over Cu–mordenite. *Chem. Commun.*, 48:404–406, 2012.

[37] Zhijun Zuo, Pedro J. Ramírez, Sanjaya D. Senanayake, Ping Liu, and José A. Rodriguez. Low-temperature conversion of methane to methanol on CeO_x/Cu_2O catalysts: Water controlled activation of the C–H bond. *Journal of the American Chemical Society*, 138(42):13810–13813, 2016.

[38] Yangyang Li, Yunshang Zhang, Kun Qian, and Weixin Huang. Metal–support interactions in Metal/Oxide catalysts and Oxide–Metal interactions in Oxide/Metal inverse catalysts. *ACS Catalysis*, 12(2):1268–1287, 2022.

[39] Zongyuan Liu, Erwei Huang, Ivan Orozco, Wenjie Liao, Robert M. Palomino, Ning Rui, Thomas Duchoň, Slavomir Nemšák, David C. Grinter, Mausumi Mahapatra, Ping Liu, José A. Rodriguez, and Sanjaya D. Senanayake. Water-

promoted interfacial pathways in methane oxidation to methanol on a $CeO_2 - Cu_2O$ catalyst. *Science*, 368(6490):513–517, 2020.

[40] Liqun Kang, Bolun Wang, Qiming Bing, Michal Zalibera, Robert Büchel, Ruoyu Xu, Qiming Wang, Yiyun Liu, Diego Gianolio, Chiu C Tang, et al. Adsorption and activation of molecular oxygen over atomic Copper (I/II) site on Ceria. *Nature communications*, 11(1):1–11, 2020.

[41] Liqun Kang, Bolun Wang, Andreas T Güntner, Siyuan Xu, Xuhao Wan, Yiyun Liu, Sushila Marlow, Yifei Ren, Diego Gianolio, Chiu C Tang, et al. The electrophilicity of surface carbon species in the redox reactions of $CuO - CeO_2$ catalysts. *Angewandte Chemie International Edition*, 60(26):14420–14428, 2021.

[42] Gabriel Garcia, Emmanuel Arriola, Wei-Hsin Chen, and Mark Daniel De Luna. A comprehensive review of hydrogen production from methanol thermochemical conversion for sustainability. *Energy*, 217:119384, 2021.

[43] Antonius Indarto and Jelliarko Palgunadi. *Syngas: Production, Applications and Environmental Impact.* 11 2012.

[44] Yixing Li, Yin Pang, Hengyong Tu, Federica Torrigino, Serge M.A. Biollaz, Zhuo Li, Yanqin Huang, Xiuli Yin, Fabian Grimm, and Jürgen Karl. Impact of syngas from biomass gasification on solid oxide fuel cells: A review study for the energy transition. *Energy Conversion and Management*, 250:114894, 2021.

[45] Jeeban Poudel, Ja Hyung Choi, and Sea Cheon Oh. Process design characteristics of Syngas (CO/H_2) separation using composite membrane. *Sustainability*, 11(3), 2019.

[46] S.P. DiMartino, J.L. Glazer, C.D. Houston, and M.E. Schott. Hydrogen/carbon monoxide separation with cellulose acetate membranes. *Gas Separation Purification*, 2(3):120–125, 1988.

[47] Ankica Kovač, Matej Paranos, and Doria Marciuš. Hydrogen in energy transition: A review. *International Journal of Hydrogen Energy*, 46(16):10016–10035, 2021. Hydrogen and Fuel Cells.

[48] Wu-Hsun Cheng. Controlled-environment XRD study of CuZnO related to activity in methanol decomposition. *Materials chemistry and physics*, 41(1):36–40, 1995.

[49] Wu-Hsun Cheng. Reaction and XRD studies on Cu based methanol decomposition catalysts: Role of constituents and development of high-activity multicomponent catalysts. *Applied Catalysis A: General*, 130(1):13–30, 1995.

[50] Chung Lee, Hyung-Kee Yoon, Seung-Hyun Moon, and Ki June Yoon. Methanol decomposition over supported Palladium and Platinum. *Korean Journal of Chemical Engineering*, 15(6):590–595, 1998.

[51] Wu-Hsun Cheng. Development of methanol decomposition catalysts for production of H_2 and CO. *Accounts of chemical research*, 32(8):685–691, 1999.

[52] Ya Xu, Satoshi Kameoka, Kyosuke Kishida, Masahiko Demura, An-pang Tsai, and Toshiyuki Hirano. Catalytic properties of Ni_3Al intermetallics for methanol decomposition. *Materials transactions*, 45(11):3177–3179, 2004.

[53] Toshimasa Ohashi, Yuting Wang, and Shiro Shimada. Preparation and high catalytic performance of hollow BN spheres-supported Ni for hydrogen production from methanol. *Journal of Materials Chemistry*, 20(24):5129–5135, 2010.

[54] Tanya Tsoncheva, Veselina Mavrodinova, Ljubomira Ivanova, Momtchil Dimitrov, Stavry Stavrev, and Christo Minchev. Nickel modified ultrananosized

diamonds and their application as catalysts in methanol decomposition. *Journal of Molecular Catalysis A: Chemical*, 259(1-2):223–230, 2006.

[55] Yasuyuki Matsumura, Koji Tanaka, Naoki Tode, Tetsuo Yazawa, and Masatake Haruta. Catalytic methanol decomposition to carbon monoxide and hydrogen over nickel supported on silica. *Journal of Molecular Catalysis A: Chemical*, 152(1):157–165, 2000.

[56] Marc Armbrüster. Intermetallic compounds in catalysis-A versatile class of materials meets interesting challenges. *Science and Technology of Advanced Materials*, 21(1):303–322, 2020.

[57] Shinya Furukawa and Takayuki Komatsu. Intermetallic compounds: promising inorganic materials for well-structured and electronically modified reaction environments for efficient catalysis. *ACS Catalysis*, 7(1):735–765, 2017.

[58] Anish Dasgupta and Robert M Rioux. Intermetallics in catalysis: an exciting subset of multimetallic catalysts. *Catalysis Today*, 330:2–15, 2019.

[59] Vijaykumar S Marakatti and Sebastian C Peter. Synthetically tuned electronic and geometrical properties of intermetallic compounds as effective heterogeneous catalysts. *Progress in Solid State Chemistry*, 52:1–30, 2018.

[60] Marta Michalska-Domańska, Jerzy Bystrzycki, Bartłomiej Jankiewicz, and Zbigniew Bojar. Effect of the grain diameter of Ni-based catalysts on their catalytic properties in the thermocatalytic decomposition of methanol. *Comptes Rendus Chimie*, 20(2):156–163, 2017.

[61] AP Tsai, S Kameoka, K Nozawa, M Shimoda, and Y Ishii. Intermetallic: a pseudoelement for catalysis. *Accounts of Chemical Research*, 50(12):2879–2885, 2017.

[62] Marc Armbrüster, Robert Schlögl, and Yuri Grin. Intermetallic compounds in heterogeneous catalysis—a quickly developing field. *Science and Technology of Advanced Materials*, 2014.

[63] Ayumu Onda, Takayuki Komatsu, and Tatsuaki Yashima. Characterization and catalytic properties of Ni-Sn intermetallic compounds in acetylene hydrogenation. *Physical Chemistry Chemical Physics*, 2(13):2999–3005, 2000.

[64] Meiqiang Fan, Ya Xu, Junya Sakurai, Masahiko Demura, Toshiyuki Hirano, Yuden Teraoka, and Akitaka Yoshigoe. Spontaneous activation behavior of Ni_3Sn, an intermetallic catalyst, for hydrogen production via methanol decomposition. *International Journal of Hydrogen Energy*, 40(37):12663–12673, 2015.

[65] Ya Xu, Huixin Jin, Toshiyuki Hirano, Yoshitaka Matsushita, and Jianxin Zhang. Characterization of Ni_3Sn intermetallic nanoparticles fabricated by thermal plasma process and catalytic properties for methanol decomposition. *Science and Technology of Advanced Materials*, 20(1):622–631, 2019.

[66] Meiqiang Fan, Ya Xu, Junya Sakurai, Masahiko Demura, Toshiyuki Hirano, Yuden Teraoka, and Akitaka Yoshigoe. Catalytic performance of Ni_3Sn and Ni_3Sn_2 for hydrogen production from methanol decomposition. *Catalysis letters*, 144(5):843–849, 2014.

Chapter 3

Methods

This chapter gives an overview of the main experimental techniques that have been exploited in this thesis work. Large space has been given to the description of X-ray absorption spectroscopy and to its use in *operando* conditions, since most of the thesis project has been developed around its application in the field of heterogeneous catalysis. A detailed description is also given for the X-Ray Photoemission Spectroscopy, since it gives complementary information to the XAS technique, and being the pillar technique at the APE-HE beamline (where most of the thesis work was conducted). Other characterization techniques exploited to give a clearer interpretation of the results and a complete characterization of the studied catalysts are mentioned in this chapter in order to report the technical specifics related to the experiments described in the Results and Discussion chapter. The description is limited to the techniques directly used by the thesis author.

3.1 Experimental Tecnhiques

3.1.1 X-Ray Absorption Spectroscopy (XAS)

The absorption of an electro-magnetic radiation is a phenomenon which can be exploited in a wide variety of applications, providing a vast amount of information

about the physical and chemical properties of a material. In the electro-magnetic radiation spectrum, X-Rays fall between the UV and the γ-Rays frequencies. The X-Rays region is further divided in the so-called *soft X-Rays* (100 eV- 3 keV range) and *hard X-Rays*, with energies above 3 keV[1]. Clearly, absorption processes depend on the photon energy of the incident radiation; X-Rays, in particular, are able to interact with the most internal electrons of the material (i.e. the *core* electrons): the *absorption* is the consequent electronic excitation of the *core* electron towards an empty molecular orbital, leaving a *core-hole* (see Fig.3.1(a)). Thus, an X-Ray absorption spectrum (i.e. a scan of the absorption intensity in a defined photon energy range) acquired in promixity of a specific absorption edge gives a representation of the electronic structure of the empty states of the absorbing atom, related to specific electronic transitions. This allows, for example, to obtain information about the oxidation state of the absorbing atom.
Another fundamental advantage of XAS spectroscopy is the strong localization of the *core* electron on the absorbing atom, which makes the absorption process strongly dependent on its local surroundings. This makes core spectroscopies particularly informative, because they can provide detailed information about the local chemical and geometrical environment of the atom in which the hole is created. This feature allows to study also not ordered systems[2].

Experimentally, X-Ray Absorption Spectroscopy (XAS) measures the absorption coefficient μ of a sample as a function of the incident radiation energy (I_0), that for a homogeneous isotropic material follows the Lambert-Beer equation:

$$I = I_0 e^{-\mu D} \tag{3.1}$$

where D is the thickness of the sample and I is the transmitted beam intensity. The coefficient μ, for a crystalline solid, is given by the sum of the *absorption cross section* σ_i related to the n different chemical elements of the unit cell:

$$\mu = \frac{1}{V}\sum_{i=1}^{n}\sigma_i \tag{3.2}$$

where V is the volume of the unit cell. Experimentally, μ can be determined as the ratio of the beam intensities with and without the sample.

In non resonant regions the absorption coefficient decreases with increasing photon energy, but when the excitation energy is comparable to the binding energy of core electrons, there is a net absorption increase, which gives rise to the *absorption edges* (Fig.3.1(b)).

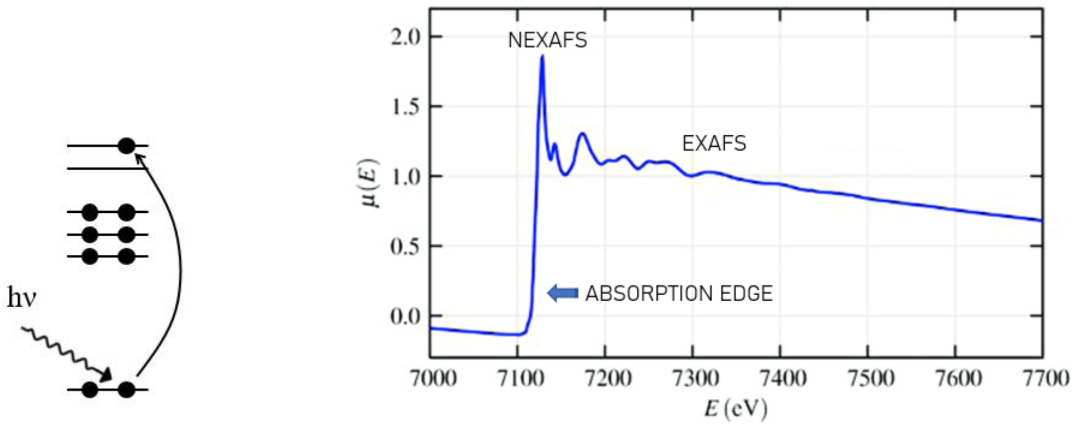

(a) (b)

Figure 3.1: a) Schematic description of the *absorption* process. b) X-ray absorption spectrum of FeO with the NEXAFS and EXAFS regions[3].

Thus, every *core* electron will generate a different absorption edge, depending on its energetic starting point in the electronic structure. This fact takes to one of the most important features of XAS: by tuning the incident photon energy it is possible to select a single absorption edge. Since the absorption edges of the elements are most of the time energetically separated, even having a sample consisting of different chemical species it is possible to isolate the XAS spectrum of a single element. Moreover, it is also possible to identify different absorption edges for the same element depending on what is the initial *core* level of the excitation;

Table 3.1: Absorption edges IUPAC nomenclature[4].

Edge	Electronic configuration	Edge	Electronic configuration	Edge	Electronic configuration
K	$1s^{-1}$	N_1	$4s^{-1}$	O_1	$5s^{-1}$
L_1	$2s^{-1}$	N_2	$4p^{-1}_{1/2}$	O_2	$5p^{-1}_{1/2}$
L_2	$2p^{-1}_{1/2}$	N_3	$4p^{-1}_{3/2}$	O_3	$4p^{-1}_{3/2}$
L_3	$2p^{-1}_{3/2}$	N_4	$4d^{-1}_{3/2}$	O_4	$4d^{-1}_{3/2}$
M_1	$3s^{-1}$	N_5	$4d^{-1}_{5/2}$	O_5	$4d^{-1}_{5/2}$
M_2	$3p^{-1}_{1/2}$	N_6	$4f^{-1}_{5/2}$	O_6	$4f^{-1}_{5/2}$
M_3	$3p^{-1}_{3/2}$	N_7	$4f^{-1}_{7/2}$	O_7	$4f^{-1}_{7/2}$
M_4	$3d^{-1}_{3/2}$				
M_5	$3d^{-1}_{5/2}$				

in this sense IUPAC defined a specific nomenclature (see Tab.3.1): for example, an electronic excitation starting from a $1s$ orbital will give rise to a $K - edge$.

According to X-Ray photon energy, XAS is divided in two regions: the *Near Edge X-Ray Absorption Fine Structure* (NEXAFS or XANES), which covers the energetic range starting from few eV before the absorption edge to 50 eV above it, and the *Extended X-Ray Absorption Fine Structure* (EXAFS), which goes from the upper limit of the NEXAFS region to few hundreds of eV above the absorption edge (Fig.3.1(b)). The NEXAFS region is further divided in *pre-edge*, *main-edge* and *post-edge* regions, each of them providing different information about the electronic structure of the sample, as explained in detail in section 3.1.1.3.

3.1.1.1 Theoretical description of the X-Ray Absorption Process

Let's consider the incoming radiation as a plane wave propagating in the x direction[1]: one can define the vector potential $\boldsymbol{A}$, the electric field $\boldsymbol{E}$ and the magnetic field $\boldsymbol{B}$ as follows:

$$\boldsymbol{A}(\boldsymbol{r},t) = A_0(ae^{i(\boldsymbol{k}\cdot\boldsymbol{r}-\omega t)} + a^{+}e^{-i(\boldsymbol{k}\cdot\boldsymbol{r}-\omega t)}\epsilon^{*}) \tag{3.3}$$

$$\boldsymbol{E}(\boldsymbol{r},t) = -i\omega A_0(ae^{i(\boldsymbol{k}\cdot\boldsymbol{r}-\omega t)}\epsilon - a^+e^{-i(\boldsymbol{k}\cdot\boldsymbol{r}-\omega t)}\epsilon^*) \tag{3.4}$$

$$\boldsymbol{B}(\boldsymbol{r},t) = iA_0(ae^{i(\boldsymbol{k}\cdot\boldsymbol{r}-\omega t)}\boldsymbol{k}\times\epsilon - a^+e^{-i(\boldsymbol{k}\cdot\boldsymbol{r}-\omega t)}\boldsymbol{k}\times\epsilon^*) \tag{3.5}$$

where A_0 is an amplitude related to the photon energy $\hbar\omega$, a and a^+ are the photon annihilation and creation operators, and ϵ and $\boldsymbol{k}$ are the photon polarization and wave vector.

The Hamiltonian related to the interaction of atomic electrons bound by a potential $V(\boldsymbol{r})$ with the X-Rays can be defined as:

$$H = H_{rad} + H_{atom} + H_{int} \tag{3.6}$$

H_{rad} and H_{atom} are the non-interacting part, while H_{int} is related to the interaction between the electro-magnetic field and the electron charge $-e$:

$$H_{int} = \frac{e}{m}\boldsymbol{p}\cdot\boldsymbol{A} + \frac{e}{m}\boldsymbol{S}\cdot\boldsymbol{B} + \frac{e^2}{2m}\boldsymbol{A}^{\boldsymbol{2}} \tag{3.7}$$

In this equation the first term takes into account the interaction between the electron momentum operator $\boldsymbol{p}$ and the vector potential, while the second is referred to the interaction between the electron spin ($\boldsymbol{S}$) and the magnetic field. The third is related to the Thomson scattering, which will not be treated in this discussion. From eq.3.7 we can define a transition operator:

$$T = \frac{e}{m}(\boldsymbol{p}\cdot\boldsymbol{A} + \boldsymbol{S}\cdot\boldsymbol{B}) \tag{3.8}$$

In the absorption process, in first approximation we can use the one-particle model, i.e. we assume that the core excitation and the consequent core hole formation do not modify the remaining electronic structure of the system. In other words, we do not consider the electronic correlation and the relaxation effects. In this way, we can easily define the $|i\rangle$ and $|f\rangle$ states:

$$\begin{array}{rll} |i\rangle = |\phi_i; \epsilon, \boldsymbol{k}\rangle & \text{where} & \phi_i = \text{one particle core electron state} \\ & & |\epsilon, \boldsymbol{k}\rangle = \text{incoming photon} \\ & & E_i = \epsilon_i + \hbar\omega \\ |f\rangle = |\phi_f; 0\rangle & \text{where} & \phi_i = \text{one particle photoelectron state} \\ & & E_f = \epsilon_f \end{array} \tag{3.9}$$

This description allows to define the well-known *Fermi Golden Rule*, which gives the absorption rate (in s^{-1}):

$$R_{fi} = \frac{2\pi}{\hbar} |\,\langle f|T|i\rangle\,|^2 \delta(\epsilon_f - \epsilon_i - \hbar\omega) \tag{3.10}$$

For a plane wave, R_{fi} can be related to the *cross-section*:

$$\sigma_{fi} = \frac{\hbar\omega}{I} R_{fi} \tag{3.11}$$

The radiation intensity I is defined as:

$$I = \frac{c\epsilon_0 n}{2} |E|^2 \tag{3.12}$$

where ϵ_0 is the permittivity. From equations 3.10, 3.11 and 3.12, we can rewrite the absorption cross section σ_{fi} as:

$$\sigma_{fi} = \frac{2\phi\alpha}{\omega m^2} |\,\langle \phi_f|\hat{O}|\phi_i\rangle\,|^2 \delta(\epsilon_f - \epsilon_i - \hbar\omega) \tag{3.13}$$

where

$$\alpha = \frac{e^2}{2hc\epsilon_0} \tag{3.14}$$

In this equation, σ_{fi} depends only on the electron states and no more on the incident photons. In eq.3.13 also the new operator $\hat{O}$ is defined:

$$\hat{O} = (\epsilon \cdot \boldsymbol{p} + i\boldsymbol{S} \cdot (\boldsymbol{k} \times \epsilon))e^{i\boldsymbol{k} \cdot r} \tag{3.15}$$

Applying $\hat{O}$ to $|\phi_i\rangle$ and $|\phi_f\rangle$, one can define the matrix element:

$$\langle\phi_f|\hat{O}|\phi_i\rangle = i\frac{m}{\hbar}(\epsilon_f - \epsilon_i)\,\langle\phi_f|\hat{o}|\phi_i\rangle \tag{3.16}$$

where $\hat{o}$ is expanded as the sum:

$$\hat{o} = \hat{o}_{E_1} + \hat{o}_{E_2} + \hat{o}_{E_3} + \hat{o}_{M_1} + ... \tag{3.17}$$

E_1, E_2 and E_3 represent respectively the dipole, quadrupole and octupole electric transition channels, while M_1 is related to the dipole magnetic transition channel. For photon energies up to 4500 eV, E_1 is the dominant term, while above that energy also E_2 term has to be taken into account; E_2 can be relevant also for the $L_{2,3}$ edges, because for this channel the selection rules are different, as we will see more in detail later. From eq.3.13 and 3.16 we can obtain the final formulation for the cross section:

$$\sigma_{fi} = 4\pi^2\alpha\hbar\omega|\,\langle\phi_f|\hat{o}|\phi_i\rangle\,|^2\delta(\epsilon_f - \epsilon_i - \hbar\omega) \tag{3.18}$$

The dipole approximation and selection rules The expansion terms of eq. 3.17, can also be defined as follows:

$$\begin{aligned}
\hat{o}_{E_1} &= \epsilon \cdot \boldsymbol{r} \\
\hat{o}_{E_2} &= \frac{i}{2}(\epsilon \cdot \boldsymbol{r})(\boldsymbol{k} \cdot \boldsymbol{r}) \\
\hat{o}_{E_3} &= -\frac{1}{6}(\epsilon \cdot \boldsymbol{r})(\boldsymbol{k} \cdot \boldsymbol{r})^2 \\
\hat{o}_{M_1} &= C_m(\boldsymbol{k} \times \epsilon) \cdot (\boldsymbol{L} + 2\boldsymbol{S})
\end{aligned} \tag{3.19}$$

where $C_m = \frac{\hbar}{2m(\epsilon_f - \epsilon_i)}$. As it can be seen, $\hat{o}_{E_2}$ contains the $\boldsymbol{k} \cdot \boldsymbol{r}$ factor. For X-Rays photon energies below a few tens of keV the latter is on the magnitude order of $\simeq 10^{-2}$, so when it is squared to calculate the transition probability $(|\,\langle\phi_f|\hat{O}|\phi_i\rangle\,|^2)$ it can be neglected. When, as in this case, only the E1 term is taken into account to evaluate the cross section, it falls within the so-called *dipole* *approximation*, valid mainly for the K edges of the low Z elements. For the $L_{2,3}$ and $M_{4,5}$ edges, when they fall in the soft X-Rays (200 eV- few keV) the dipole component E1 is still prevailing, but also quadrupole transitions can be observed.

The next step of the discussion arises the question of how to calculate the integral $\langle \phi_f|\hat{o}|\phi_i\rangle$, that we defined in eq.3.16. Firstly, we have to consider the bahaviour resulting from the different absorption edges; in the case of the K edge, the excited core electron is highly localized, thus the integral can be approximated to a small sphere inside the absorbing atom. On the contrary, when we consider excitations starting from less localized orbitals (for example related to the $L_{2,3}$ or $M_{4,5}$ edges) the above mentioned approximation loses its validity, because the spin-orbit coupling has to be taken into account. So, the general formulation of the wave functions which comprise also the spin-orbit coupling can be expressed using an expansion in complex spherical waves:

$$\phi = \sum_{lms} a_{l,m+\frac{1}{2}-s,s} \sum_{\sigma} b_{l,m+\frac{1}{2}-\sigma,s,\sigma}(r) Y_l^{m+\frac{1}{2}-\sigma} \chi_\sigma \tag{3.20}$$

where l, m, and s are the usual quantum numbers, $\sigma = \pm\frac{1}{2}$ is the spin and χ_σ are the spin states. Without the spin-orbit coupling (K edge), $s = \sigma$ and eq. 3.20 becomes:

$$\phi = \sum_{lm\sigma} a_{l,m,\sigma} b_{l,\sigma}(r) Y_l^m \chi_\sigma \tag{3.21}$$

Now that we defined the wave functions ϕ, we have to consider the $\hat{o}$ operator. The latter can be also expanded in spherical harmonics:

$$\hat{o} = \sum_{l_0,m_0} c_{l_0,m_0} (ik)^{l_0-1} r^{l_0} Y_{l_0}^{m_0}(\Omega) \tag{3.22}$$

where c_{l_0,m_0} are coefficients depending on l_0 and m_0, and $l_0 = 1$ for E1, $l_0 = 2$ for E2 and $l_0 = 3$ for E3. Now we have all the elements to calculate the $\langle \phi_f|\hat{o}|\phi_i\rangle$ integral, combining eq.3.20 and 3.22:

$$\langle \phi_f | \hat{o} | \phi_i \rangle_\sigma = \sum_{L_0} (ik)^{l_0 - 1} c_{L_0} \sum_{LL_i} \Gamma_{LL_0L_i} \sum_{ss_i} R_{LL_0L_iss_i\sigma} a^{f*}_{l,m+\sigma-s,s} a^{i}_{l_i,m_i+\sigma-s_i,s_i} \tag{3.23}$$

where $L = (l, m)$, o and i are the index for respectively the operator and the initial state. What is important to underline in this long and complex expression is the angular integral:

$$\Gamma_{LL_0L_i} = \int_{sphere} Y_l^{m^*}(\Omega) Y_{l_0}^{m_0}(\Omega) Y_{l_i}^{m_i}(\Omega) d\Omega \tag{3.24}$$

because it will define the absorption selection rules, fundamental to understand the XAS spectra. Indeed, the integral of eq.3.24 is $\neq 0$ only if:

- l has the same parity as $l_i + l_0$;
- $|l_i - l_0| \leq l \leq |l_i + l_0|$;
- $m = m_0 + m_i$

These conditions are satisfied if the difference between the initial and the final state is $\Delta l = \pm 1$ for E1 and $\Delta l = \pm 2$ for E2. This conclusion is crucial becauses it poses one of the basis of XAS spectroscopy: in the *dipole approximation*, the allowed transitions will be the one with $\Delta l = \pm 1$, thus for the K edge only the $s \rightarrow p$. In this way, looking at the K edge spectra of an element, the absorption intensity will reflect the p component of the final orbitals involved in the excitation. Similarly, the $L_{2,3}$ and $M_{4,5}$ edges will probe the d and f components.

3.1.1.2 Experimental description of XAS

Experimentally, the sample is irradiated with monochromatic X-Rays, whose energy is scanned in a range of few eV around the absorption edge of an element. The best X-Ray source to perform such experiments is the Synchrotron radiation, because of the wide energy tunability and the unique features of the Synchrotron sources (high brilliance, collimation, high level of polarization). As already mentioned in the previous chapter, when the beam hits the sample a core-excitation to empty virtual orbitals occurs, leaving a core-hole and creating a "particle" state. The excited state is characterized by a short lifetime, so the destiny of the core-hole is its refilling, which can happen through two different processes: the fluorescence emission (radiative process process) and the Auger electron emission (non radiative process).

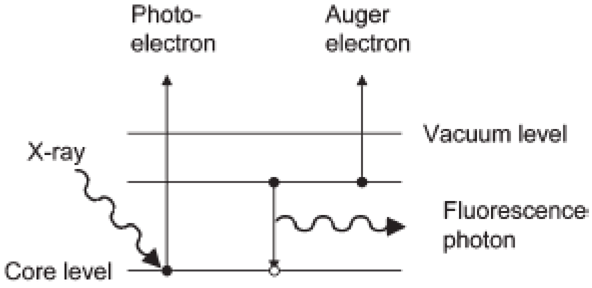

Figure 3.2: Photoabsorption process and the following core hole filling in XAS spectroscopy through radiative decay (fluorescence emission) or non radiative (Auger electron emission).

As it can be seen in Fig.3.2, the fluorescence is the process through which an electron located in an external shell fills the core-hole emitting a photon with a defined energy. The Auger effect, instead, involves two electrons: the first one decays refilling the core-hole, but its energy is transferred to another electron (the Auger electron), which is then emitted in the *continuum.* Indeed, the Auger transitions are labelled with three letters: for example, a KLL transition involves an excitation from a $1s$ electron, which is refilled by another electron located in a L shell, causing the emission of another L shell electron.

The most direct and classical way to measure XAS spectra is the *transmission* mode (Fig.3.3), where the absorption coefficient μ is measured by determining the beam intensity before and after the sample, and applying the Lambert Beer equation (3.1). The experimental detection of I and I_0 in this case is made through

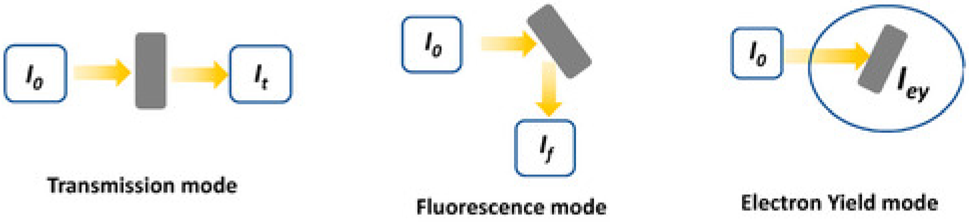

Figure 3.3: Possible measurements modes for a XAS experiment. Left: Transmission mode; center: Fluorescence Yield mode; right: Electron Yield mode.[5]

ionization chambers, positioned before and after the sample chamber. Usually, the *transmission* mode is used with hard X-Rays sources, because for the soft X-Rays the high cross-section would require very thin samples. Moreover, this technique is not surface sensitive, so it is not the most suitable for catalysis or surface physics studies[6]. The *fluorescence yield*(FY) mode consists in the detection of the emitted fluorescence photons. To a limited extent FY is proportional to the absorption cross-section (for diluted and thin samples). Experimentally, the fluorescence photons are collected by a photodiode. The third detection method is the *Electron yield* (EY), where the emitted electrons are collected. This technique is further split up in the *partial* electron yield (PEY), where the electrons are detected only in a selected energy window, and the *total* electron yield (TEY), which consists in the collection of the primary, Auger and secondary electrons (deriving from inelastic electron-electron scattering of the Auger photoelectrons). The latter can be exploited to obtain a larger signal[7]. As mentioned above, fluorescence and Auger decays are competitive processes: the latter is predominant for the core levels with binding energies below 1 keV. Moreover, considering the huge difference of the mean free paths of electrons and Soft X-Ray photons in solids, EY is much more surface sensitive than FY. The sampling depth d depends on different factors (for example the incident photon energy and the material composition) but usually it is < 7 nm for the EY mode, while it falls around 100 nm for the FY. For this reason, TEY is a effective detection mode to investigate catalytic reactions, that

occurr on the sample surface.
In the present thesis, all the NEXAFS spectra presented have been collected with TEY mode and by using a Synchrotron radiation as X-Ray source: the detailed experimental setup will be explained in detail in chapter 3.2.

3.1.1.3 NEXAFS Spectroscopy

This spectroscopic technique was developed in the 1980s, and initially was used to resolve the structure of molecules bonded to surfaces, while nowadays NEXAFS experiments are exploited to investigate the properties of a wide range of molecules and materials, ranging from solids to molecules in gas phase[8]. A NEXAFS spectrum originates from the absorption of an electro-magnetic radiation, and comprehends the energy range around an absorption edge. The intensity of the features appearing in a spectrum reflects the dependence of the photoabsorption cross-section on the photon energy, already described in detail in the previous section. The fine spectral features originate because around the ionization potential (IP), resonant transitions are superimposed on the step-like shape of the absorption edge; these transitions come from all the excitations towards the unoccupied molecular orbitals (MOs) of the investigated chemical species. According to their simmetry, the virtual MOs are labeled as π or σ orbitals. The NEXAFS region is further divided into three regions: the *pre-edge*, that falls at photon energy lower than the ionization potential (IP) of the core-electrons, the region around it(*main edge*) and the *multiple scattering region*, located above the IP, where multiple scattering phenomena dominate the signal.

To illustrate what are the most common features of a NEXAFS spectrum, a clarifying scheme is reported in Fig.3.4, where in the top panel the K edge spectrum of a diatomic molecule, such as CO, is reported.

Before the IP, at the lowest photon energies arise the transitions toward the lowest unoccupied molecular orbitals (LUMO), which in this case is a MO with

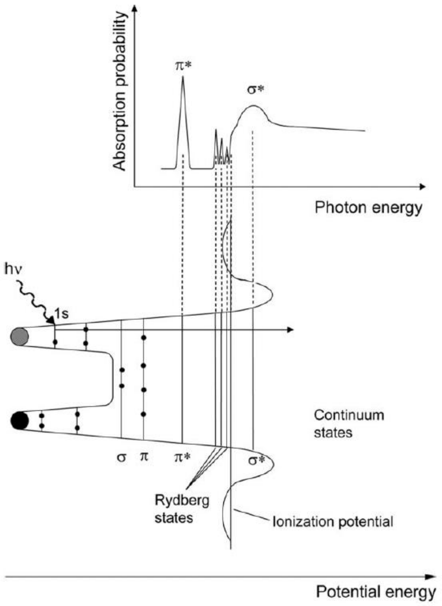

Figure 3.4: Schematic molecular potential and the corresponding K edge NEXAFS spectrum of a diatomic unsaturated molecule. At the bottom, empty and filled bound states are represented, while at the top are showed the different spectra features produced by the core electron excitation toward empty states.

π^* character. These resonances are located below the IP because of the electron-hole Coulomb interaction. These features can be observed only in presence of π orbitals, so they are intense and sharp for molecules with double and triple bonds or in aromatic systems. At higher photon energies, but below the IP, usually fall the so-called *Rydberg* resonances, which are related to toward more diffuse MOs. These resonances are often weak and sharp. In solids, they can be quenched because the relative MOs are delocalized. At higher photon energies (usually above the IP) we can find the σ^*, which are related to transitions towards MOs with a prevalent σ character. So, the energetic position of a resonance in a NEXAFS spectrum is crucial in order to understand the electronic structure of the absorbing atom. The second important feature from which we can obtain useful information is the relative intensity of the resonances, that as we already saw is determined by the dipole selection rules, allowing to understand the atomic composition of the virtual MOs. The third aspect to consider is the width of a resonance, which depends on three main factors: the resolution of the instrument, the core-hole lifetimes (which for NEXAFS is normally $\approx 10^{-15} - 10^{-16} s9$ and the vibronic effects (which often result in asymmetrical peak broadening). This explains why usually the π^* resonances are very sharp, indeed the relative lifetime is determined only by the decay of the core-hole. For transitions towards σ^* orbitals, since they are overlapped with continuum states, the decay probability of the electron to the continuum is increased. So, the more the resonances are close to the continuum the more they are broadened.

Another important feature of NEXAFS is its sensitivity to the polarization of the incident radiation; this allows to exploit NEXAFS to determine the orientation of a molecule when it is adsorbed on a surface. Indeed, the intensity of the resonances shows a significant angular dependence on σ^* and π^* orbitals of oriented molecules, i.e. *dichroism.* Assuming $\boldsymbol{E}$ as the electric field of the linearly polarized radiation, its relative orientation with respect to the adsorbed molecule causes modifications in the resonances intensities. Recalling eq.3.18 for the absorption cross-section, and applying the dipole approximation, we can rewrite it as follows:

$$\sigma_x \propto | \langle \phi_f | \boldsymbol{e} \cdot \boldsymbol{r} | \phi_i \rangle |^2 \rho_f(E), \tag{3.25}$$

where $\boldsymbol{e}$ is the unit electronic field vector, $\boldsymbol{r}$ is the dipole transition operator and $\rho_f(E)$ is the density of final states. When linearly polarized light is used, $\boldsymbol{e}$ can be removed from the matrix element. For a transition starting from a $1s$ orbital towards a directional final state $\boldsymbol{O}$, the transition intensity is defined as:

$$I \propto |\boldsymbol{e} \langle \phi_f | \boldsymbol{r} | \phi_i \rangle |^2 \rho_f(E) \propto |\boldsymbol{e} \cdot \boldsymbol{O}|^2 \propto \cos^2 \delta, \tag{3.26}$$

where δ is the angle between $\boldsymbol{E}$ and $\boldsymbol{O}$ (see Fig.3.5). Thus, the more $\boldsymbol{E}$ overlaps with $\boldsymbol{O}$, the more the resonance will be intense. Since $\boldsymbol{O}$ vectors for pure σ^* and π^* orbitals are perpendicular, according to the horizontal or vertical polarization of the incident light one can enhance the different nature of the virtual orbitals, thus understanding how the molecule is oriented on the surface.

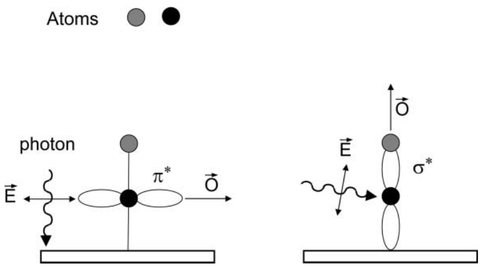

Figure 3.5: Schematic representation of the angular dependence of σ^* and π^* resonances in NEXAFS spectroscopy for an adsorbed diatomic molecule.

3.1.1.4 *Operando* NEXAFS and its applications in heterogeneous catalysis

Nowadays heterogeneous catalysis is acquiring a crucial role for the world economy and for the energy transition objectives that the European Union has set on its agenda, largely accelerated given the recent energetic crisis. One of the main aims is to develop and optimize materials able to exploit renewable sources to produce energy, or to convert waste gases coming from the combustion of fossil fuels to less harmful products (or even better to re-usable green fuels), perhaps exploiting the process to produce green energy. Moreover, more than 85% of all the fuels and chemicals are industrially produced through catalytic processes[9]. Even if catalytic reactions are so exploited in industrial processes, the understanding of the mechanisms which take to a given product selectivity and reagents conversion is still most of the time unclear. An overall comprehension of how catalytic reactions on a surface take place would lead to important steps forward for the development of more performing catalysts, with a great economic and environmental profit. Traditional characterization techniques such as microscopies, X-Ray Diffraction, Infrared, Raman, UV-Vis spectroscopies, X-Ray Photoemission Spectroscopy, can give important information about some catalysts properties, but with great limitations. Among them, the fact that usually the catalyst is measured not at its real operating conditions prevents to obtain information about the catalytic mechanism. If the design of a catalyst starts from a model systems that is initially studied in ultra high vacuum conditions, one has then to take into account three fundamental problems: the real materials (which often are very defected, and this can considerably influence the catalyst behaviour), the real pressure and the system complexity under operating conditions. Only considering these three aspects the obtained results can be exploited in order to develop large scale industrial catalysts. As an example, a comparison of a surface IR-Vis sum frequency generation study of Rh and Pt catalysts study under UHV conditions and at ambient pressure (AP) conditions revealed clearly that at ambient pressure the surface goes through reconstruction[10]. Another fundamental aspect to be taken into account is that in UHV conditions it is not possible to observe surface reaction intermediates. In other words, some crucial modifications of the sample are totally invisible. Thus, *operando* measurements are necessary to detect these transient modifications, in order to correlate them with the catalytic activity and selectivity.

The term *"operando"* has been introduced into catalysis literature in 2002[11] and refers to a measurement process that combine a simultaneous *in situ* spectroscopy and kinetic study on the same sample. Actually, *operando* studies have already been performed before 2002 (the first in 1977[12]). In this thesis, we exploited the *operando* NEXAFS spectroscopy in the soft X-Rays. As already seen in the previous chapter, NEXAFS is a powerful tool to investigate the local environment of the different chemical species in a material, highlighting that, among the various possible detection methods, the EY is the more surface sensitive. Thus, coupling NEXAFS spectroscopy in EY mode, with an experimental setup able to measure an absorption spectrum while a catalytic reaction is occurring and at ambient pressure, allows to directly observe how the interactions between the reactants and the surface are changing in time by looking at the variations of the NEXAFS spectra, and as a consequence to follow the different steps of reaction mechanism. Moreover, the implementation of an online instrument able to detect the reaction products, such as a mass spectrometer or a gas chromatograph, allows to obtain further information about the occurring catalysis, by detecting the reaction products.

The first *operando* NEXAFS setups were built to perform experiments with hard X-Rays, because of their hard penetration, even if for catalysis studies the use of the soft X-Rays is more suitable, since for example the $L_{2,3}$ edge of transition metals probe mainly the d empty orbitals, which usually are the responsible of the bonds with the reactants at the catalysts surface, and are the most sensitive to the crystal field of the metal centers in solid crystals. Moreover, also the K edges of the light Z elements (such as C, O, N, of which most of the reagents are made) fall in the soft X-Rays range. On the other hand, the design of an experimental setup where electrons have to travel through air until they are detected is difficult, given their short mean free path. Nevertheless, the first setup dedicated to the near ambient pressure Soft X-Ray NEXAFS was designed by Krop-Gericke in the late '90s[13]. A few years passed to reach the real ambient pressure NEXAFS setups, helped also by the commercial availability of very thin Si_3N_4 windows, which are able to withstand the huge differential pressure existing between the AP-NEXAFS reaction chamber and the rest of the beamline, and at the same time being transparent to the soft X-Rays. Currently, only few beamlines worldwide are equipped with an experimental setup suitable to perform measurements in the soft X-Rays[14–21]. Among these, APE-HE beamline at Elettra Synchrotron in Trieste[19] is capable of carrying out the measurements routinely with a dedicated chamber. All the *operando* NEXAFS spectra reported in this thesis work have been acquired on APE-HE beamline. The design of the reaction cell of APE-HE will be described in detail in chapter 3.2.1.3.

The most important aspects that must be considered when designing a reaction cell for *operando* NEXAFS experiments are the following:

- The pressure inside the cell must reach 1 bar in order to acquire the spectra during the catalytic reactions; the cell must simultaneously be connected to the UHV of the beamline in order to make the X-Rays radiation hit the sample (for example by using a Si_3N_4 window);
- The acquisition time of the XAS spectra must be as fast as possible, in order to detect all the variations occurring during the reaction, so a fast energy scan and acquisition mode is needed.

As an example of how *operando* XAS can be useful in order to investigate catalytic reactions, in Fig.3.6 a series of NEXAFS spectra recorded at APE-HE beamline is reported[22]. In this experiment, the authors studied the evolution of the O K edge and the Sn $M_{4,5}$ edges of a powder SnO_2 catalyst, when it is exposed to gaseous H_2 at increasing temperatures. As it can be seen from the figure, from the Sn spectra it is possible to detect the reduction of the catalysts over time (from Sn^{4+} to Sn^{2+}). At the same time, by looking at the O K edge one can observe that the typical NEXAFS peaks of gaseous water are forming, meaning that the experimental system is able to detect not only the changing of the electronic structure of Sn atoms in the catalyst surface, but also the formation of the gaseous reaction product (in this case water). Thus, through these spectra one can correlate the modifications of the active sites of the catalysts with the products formation, obtaining also information on the activation temperature of the catalysts.

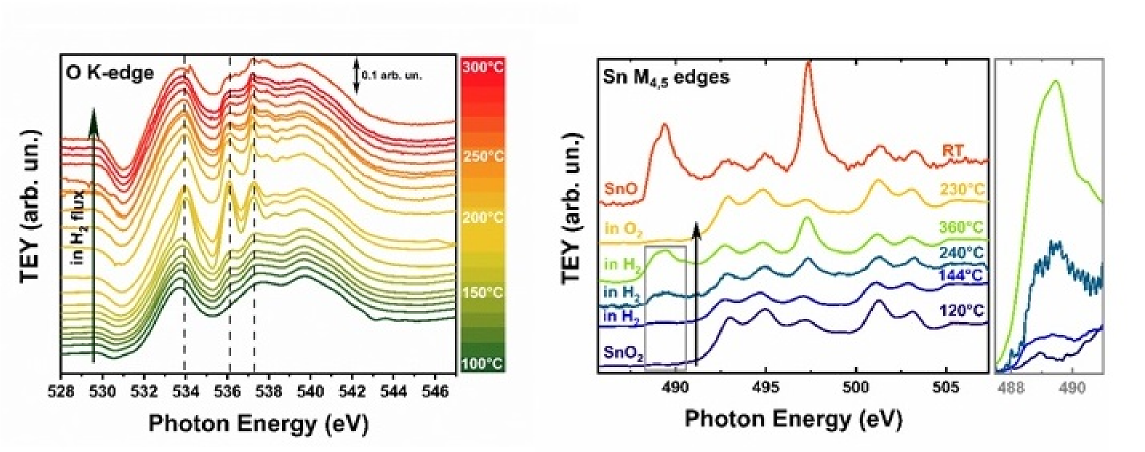

Figure 3.6: operando NEXAFS spectra collected at the APE-HE beamline. Left: Evolution of the O K edge spectra of the SnO_2 nanoparticles in flowing H_2, as a function of temperature. Right: Sn $M_{4,5}$ edges of the SnO_2 nanoparticles at different temperatures and in different conditions. The spectrum of standard SnO is shown for reference.

***In situ* vs *operando* spectroscopy** For a better understanding of this thesis work, it is important to highlight the difference between *in situ* and *operando* spectroscopies. The two terms come from the field of heterogeneous catalysis, but the precise meaning of the two concepts is still under debate. In this thesis, a spectroscopic tecnhique is defined as *in situ* when it has the aim to characterize a sample *"under reaction conditions ... or conditions relevant to reaction conditions"*[23][24]. In general, *in situ* is a term used when the conditions of pressure, atmosphere and temperature are controlled during acquisition, or the sample is not exposed to ambient conditions after specific treatments. The term *operando* was introduced more recently and describes techniques that are able to characterize a catalyst in its working conditions, correlating its structural modifications with changes in the activity/selectivity. This is done by combining the *in situ* spectroscopy with a simultaneous monitoring of how the reagents and the products are evolving, i.e. how the catalytic reaction is proceeding. Thus, an *operando* experiment is actually *in situ*, with the plus of measuring also the catalytic performance in the same experiment and with the same sample. In Fig.3.7 a schematic representation of the difference between *in-situ* and *operando* techniques is reported, for the particular case of the gas sensing[23].

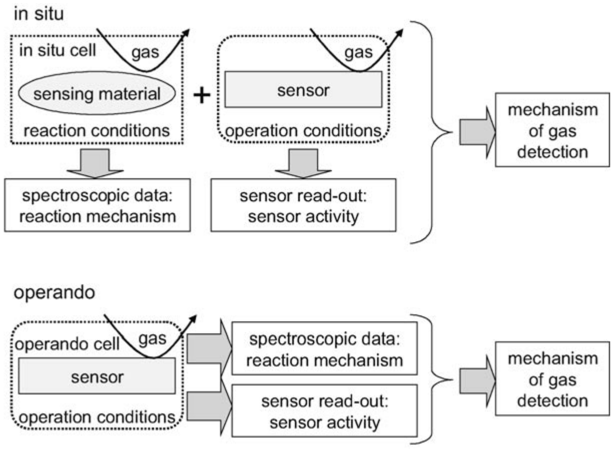

Figure 3.7: Differences between in-situ and operando methods[23].

As it can be seen in the figure, when using an *in situ* spectroscopy the activity of the material in tested separately at its real working conditions, while the spectroscopic measurement is conducted on the sample at similar reaction conditions. The combination of the two experiments can give information about the reaction mechanism. On the other hand, the *operando* measurement is done monitoring at the same time the operation of the device (through an online instrument able to detect the reaction activity) and the spectroscopic modifications occurring during its use, in the same experiment. This approach allows to directly being able to correlate the activity with the spectroscopic modifications observed.

3.1.2 X-Ray Photoemission Spectroscopy (XPS)

Since the interest in the chemical composition of surfaces has become central for materials science, there was a need of suitable characterization techniques able to provide information at the atomic layer scale. The first technique developed for the surface analysis of solids was the Auger electron spectroscopy (AES), followed by the X-Ray photoemission spectroscopy (XPS). Nowadays, AES and XPS represent the basic characterization techniques of most of the surface science studies, since as we will see later they can provide fundamental information about the elemental identification, chemical bonds, and many other surface properties. The success of XPS led to a widespread diffusion of the experimental setups dedicated to this spectroscopic technique. This thesis project involved the acquisition and analysis of photoemission spectra acquired at the APE-HE beamline, where there is the possibility to perform XPS experiments using both conventional and synchrotron based X-Rays source (the experimental setups of the beamline will be described in detail in chapter 3.2.1.2). Since this spectroscopy is now well-known, only the most important features of the technique will be reported, underlying what are the key properties which make this tool so useful for surface analysis.

XPS was developed in the middle of 1960s by Kai Seigbahn[25], who originally called the technique *ESCA* (Electron Spectroscopy for Chemical Analysis). In a typical experiment the surface of a sample is irradiated by X-Rays with defined energy, which interact with the core electrons, causing their photoemission (Fig.3.8), through the well known photoelectric effect.

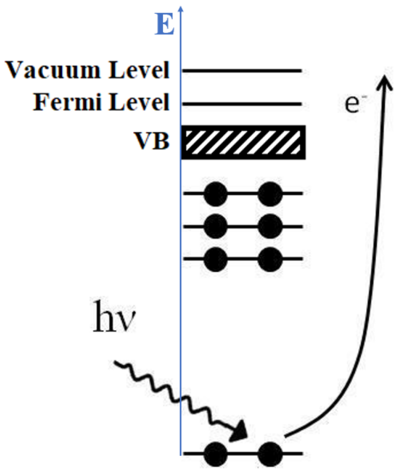

Figure 3.8: Schematic description of the *photoemission* process.

As a result, ionized states are created, and the emitted photoelectron will have a kinetic energy which can be calculated as the difference between the photon energy and the binding energy of the photoexcited core electron (i.e. the energy needed to excite the electron to the continuum), subtracting also the work function (which depend on the analyzed material). In a solid, the photoemission can be described in a simple way with the so-called *three step model* (see Fig.3.9):

1. Generation of photoelectrons and Auger electrons induced by the interaction with the X-Rays radiation;
2. These electrons move until they reach the solid surface, going through scattering processes;
3. The photoelectrons escape from surface to the vacuum.

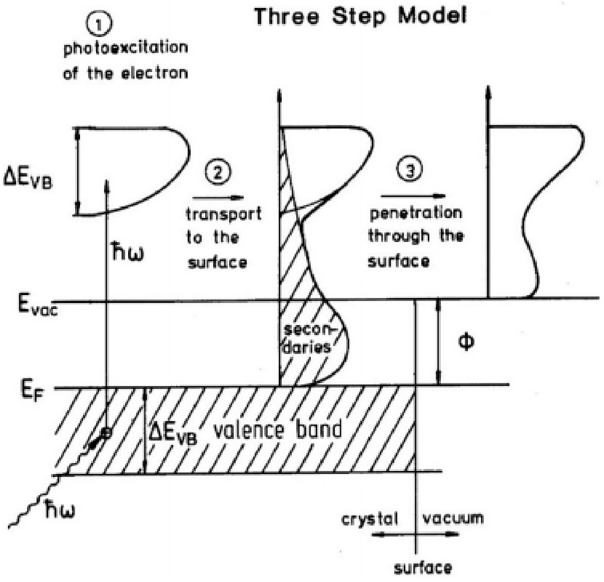

Figure 3.9: Scheme of the *three step model* for the description of the photoemission process.

For a core electron with binding energy E_b, its kinetic energy in vacuum will be defined as follows:

$$E_k = h\nu - E_b - \phi_s, \tag{3.27}$$

where $h\nu$ is the energy of the incident photons and ϕ_s is the work function of the sample. When conventional sources are used, the incident photon energy is fixed (the most used anodes are made of Al (Kα emission energy at 1486.6 eV) and Mg (1253.6 eV)), while with synchrotrons sources it is possible to choose the most suitable photon energy according to the experiment. If ϕ_A is the work function of the analyzer, the kinetic energy measured by the latter will be:

$$E_k = h\nu - E_b - \phi_s - (\phi_A - \phi_s) = h\nu - E_b - \phi_A. \tag{3.28}$$

To better visualize the process, a schematic explanation is given in Fig.3.10[26].

The relation $E_k = h\nu - E_b - \phi_A$ is the fundamental equation of XPS, because since ϕ_s is canceled in eq.3.28 and ϕ_A and $h\nu$ are known, there is a one-to-one correspondence between E_k (which is measured) and E_b. Usually, ϕ_A is around

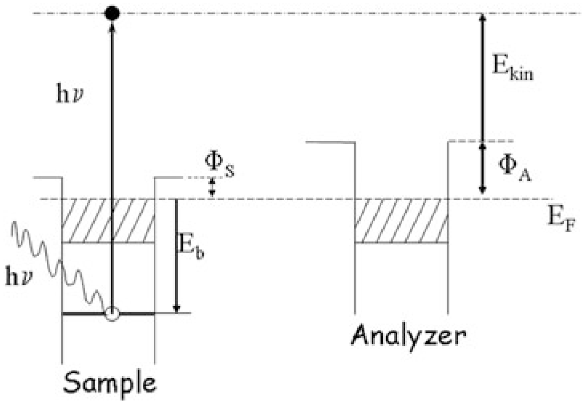

Figure 3.10: Schematic explanation of relevant energy terms in XPS of solid surfaces. The incoming photons (hν) create a core hole state and a photoelectron with binding energy E_b. The work function of the sample (ϕ_s) has to be overcome by the photoelectron, and the energy measured by the analyzer (with reference to the Fermi Energy E_F) is equal to the emitted energy diminished by the difference between the analyzer work function ϕ_A and ϕ_s[26].

4-5 eV. Eq.3.28 is valid only for conductive samples, where the Fermi energy is the same for the sample and the analyzer. For insulators or when charging effects are present, the Fermi energy is not defined and there may be energy shifts. The three step model is applicable considering the one-particle model. Actually the investigated materials are many-body systems, which are involved as a whole in the emission process. However, since the system is not too influenced by electronic correlation effects the one-particle model represents a good approximation.

The theoretical description of the photoemission spectra is based (as for XAS spectroscopy) on the *Fermi 's Golden Rule*, as a result of perturbation theory at the first order[27], where the current of emitted photoelectrons J is proportional to the transition probability from the Ground State $|\Psi_i\rangle$ to a final state $|\Psi_f\rangle = |\Psi_{\boldsymbol{k},s}\rangle$. The transition results in a photoelectron with momentum $\boldsymbol{k}$ and the remaining $(N-1)$ system:

$$J_{\boldsymbol{k}}(h\nu) = \frac{2\pi}{\hbar} \sum_{s} | \langle \Psi_{\boldsymbol{k},s} | H_{PE} | \Psi_i \rangle |^2 \delta(\epsilon_{\boldsymbol{k}} - \epsilon_s - h\nu), \tag{3.29}$$

where s comprehends the usual set of quantum numbers containing all the possible excitations to the final state. H_{PE} is the perturbation operator, having the same role of H_{int} introduced in chapter 3.1.1.1, describing the interaction between the core electrons and the electromagnetic field.

An XPS spectrum correlates the binding energies found with eq.3.28 with the relative photoelectrons counts per seconds (the intensity). Since each atom involved in the photoemission leads to a variety of possible final states, there are just as many kinetic energies where a XPS peak can be found; any different excitation has a cross-section defined by the Fermi Golden Rule (eq.3.29). Therefore, each element generates a different XPS spectrum: for example we reported the one of iron in Fig.3.11(a)^{25}.

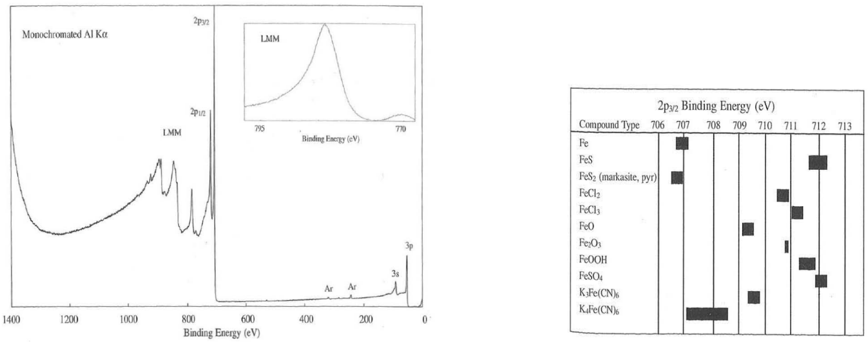

(a) (b)

Figure 3.11: a) XPS spectrum of iron, recorded by using a conventional monochromated Al source. The inset shows the LMM Auger peak of iron in the 675-800 eV range of binding energy. b) Table reporting the chemical shifts related to the different oxidation states and local chemical environment for Fe atoms.

What is the main information one can obtain from an XPS spectrum? Substantially, starting from the maximum value of the binding energy, any structure corresponds to a photoexcitation from a different initial orbital, thus it is possible to visualize from the energetical point of view how the electronic structure of the occupied states in the sample is made. For this reason XAS technique is classified as complementary to the XPS, as it probes the virtual unoccupied states of the electronic structure of a system.

Since any element has a unique set of binding energies, an XPS spectrum is element selective, and represents a fingerprint of the elements constituting the sample. As an exemplification, Fig.3.11 shows the typical XPS spectrum of metallic Fe, acquired using a monochromated Al Kα source. This type of visualization, where all the possible binding energies are probed, is called survey scan. The spectrum shows a set of different structures, related to the different orbitals in which the electronic excitation occurs and having a binding energy lower than the photon energy of the X-Ray source (in this case 1486 eV). Looking more carefully at the spectrum, one can identify the most intense structures, related to the $2p$ levels. The fact that $2p$ excitations give rise to two distinct peaks is due to the "spin-orbit coupling", i.e. an energetic splitting caused by the coupling between the electron spin and the angular momentum vector of the orbital, which can either be parallel or anti-parallel. The anti-parallel alignment results in a level with lower energy, therefore appearing at higher binding energies in the photoemission spectrum. The energetic difference between the spin orbit peaks is directly proportional to the atomic number, while their relative intensities are given by the ratio of their degeneracy $(2J + 1)$, where J is the total angular momentum quantum number. The structure shown in the inset of Fig.3.11 is referred to photoemission processes related to Auger electrons (the process is described in detail in section 3.1.1.2). Since these structures derive from Auger processes, their position in kinetic energy does not depend on the energy of the used X-Ray source.

Besides the elemental identification, XPS is very powerful in detecting any change in the bonding state of an atom, because it reflects in modifications of the spectral features: binding energy variations, peak widths and shapes, bonding satellites or valence band changes. The so-called *chemical shift* is the binding energy modification compared to the case of the pure element. Chemical shifts can originate for several reasons: the most important are the effective charge potential acting on an atom, screening effects and relaxation effects (described in detail in ref.[28–32]). These effects lead to the possibility of identifying different oxidation states of an element, which is one of the main characteristics that make this spectroscopic technique so powerful. For the case of iron, Fig.3.11(b) shows that the chemical shift between two atoms with different chemical environments can reach 5 eV. The consequence of the chemical shifts is that peaks related to specific photoemission events (for example a 2p core level excitation) can appear as a complex structure given by the convolution of more components originating from the different chemical environments of the excited atom. The relative intensities of the XPS peaks can be compared in order to obtain quantitative information about the surface composition of the analyzed material, carefully taking into account several aspects[33]:

- The different ionization cross sections, for a given atomic orbital, a given element and at a given photon energy, that can be calculated or obtained empirically; several tables and databases are available[25,34].
- The angular distribution of the photoelectrons, because they are not emitted isotropically; the cross sections dependance on the angle between the direction of the incident photons and the photoelectrons has been calculated and tabulated, even if it is valid only within the dipole approximation[34].
- The variation of the electrons mean free path according to their energy (Fig.3.12), that causes different probing depths at different electron energies. Moreover, the probing depth is proportional to $\sin\alpha$, where α is the take-off angle (i.e. the angle between the sample surface and the analyzer direction).

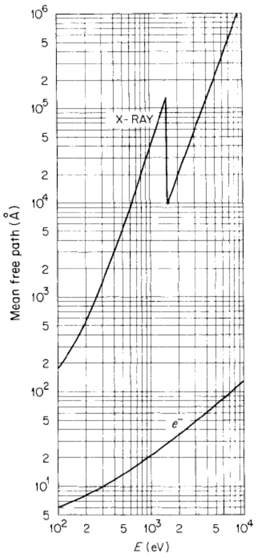

Figure 3.12: Comparison of mean free paths for electrons and X-rays in Al[33].

3.1.3 Other characterization techniques

3.1.3.1 *In Situ* Diffuse Reflectance Infrared Fourier Transform Spectroscopy (DRIFTS)

DRIFT spectroscopy is a powerful technique used to investigate the vibrational modes of the surface of powders and polymers. When used in *in situ* conditions, it can be exploited to monitor the vibrational modes of molecules interacting with the sample surface[35]. The *in situ* DRIFT spectra reported in this thesis work have been acquired at the laboratories of Catalysis for Energy and Environment of the department of Engeneering and Architecture of University of Udine. The instrument used for the measurements is a Thermo Fisher Nicolet is-50 FTIR spectrometer equipped with a specific module to perform diffuse reflectance infrared measurements. The setup consists in a complex scheme of mirrors (shown in Fig. 3.13 on the left) that allows to acquire the spectra in reflectance mode.

Moreover, a specific cell has been mounted in order to perform the *in situ* measurements (Pike™cell). The cell, shown in the right panel of Fig.3.13, is equipped with a KBr window, transparent to the IR radiation, and with inlet and outlet

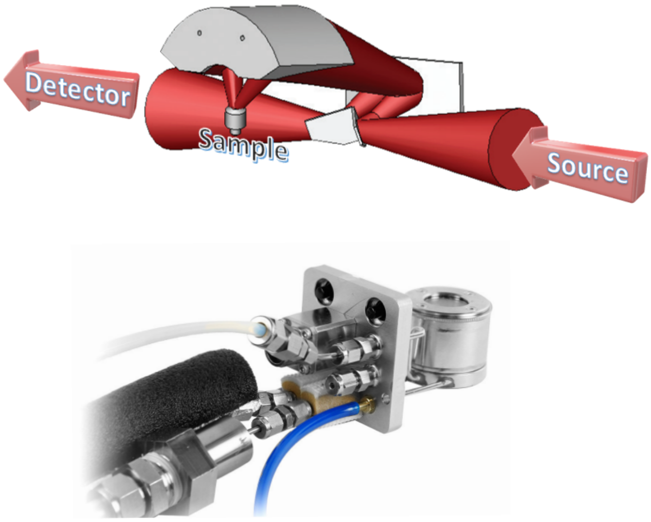

Figure 3.13: Upper panel: Optical scheme of the Diffuse IR module inserted in the spectrometer. Lower panel: Pike™cell used to perform the *in situ* experiment.

connections in order to expose the sample to different gas mixtures. Moreover, the cell can be haeated up to 500°C.

3.1.3.2 Scanning Electron Microscopy (SEM) and Energy Dispersive X-Ray Spectrscopy (EDX)

In a Scanning Electron Microscope (SEM), a focalized electron beam is scanned over the sample surface while a signal coming from secondary electrons (SE) or Back-scattered electrons (BSE) is recorded by specific electron detectors. The electron beam, which typically has an energy ranging from a few hundred eV up to 40 keV, is focused to a spot of about 0.4 nm to 5 nm in diameter.
The Scanning Electron Microscopy images have been acquired at the NFFA Trieste Laboratories of CNR-IOM (Trieste, Italy). The instrument is a ZEISS SUPRA™40 microscope equipped with three different detectors, one for the backscattered electrons and two for the secondary electrons. The first one is used to identify atoms

with different atomic number (Z) by looking at the different contrast between the particles. The secondary electrons detector is used to investigate the topography of the sample. The resolution of the instrument, with an optimal beam alignment and working distance, can reach 1.3 nm using an electron energy of 15 kV. The instrument is equipped with a EDX detector, allowing an elemental identification of the sample constituents.

3.2 Experimental Setup

3.2.1 The NFFA Trieste facility

3.2.1.1 APE beamline at Elettra Synchrotron facility

The acronym APE stands for *Advanced Photoelectric Effect*[36]. The photons coming from the section number 9 of the storage ring at Elettra Synchrotron are emitted simultaneously by two non-collinear insertion devices and then are delivered to two distinct branches, High Energy (HE) and Low Energy (LE), able to work independently. The variable polarization undulators are arranged in a zig-zag configuration such as the two beams are separated by a 2 mrad angle in the horizontal plane. The undulator related to the APE-HE branch is an APPLE-II type, made of 36 periods of 2.16 cm each. It is able to polarize the photon flux linearly (both horizontally and vertically), and circularly, by tuning the vertical gap (g) and the longitudinal phase (Z_s) betweeen the top and the bottom of the magnetic arrays. APE-LE end station is dedicated to the high resolution photoelectron spectroscopy and works at low energies (10-100 eV). APE-HE exploits photons with higher energies (140-1500 eV), and it is devoted to core-level spectroscopies, such as XAS, XPS and XMCD. All the XPS and XAS spectra discussed in this thesis have been acquired at APE-HE branch. A graphical scheme of the two end stations is depicted in Fig.3.14.

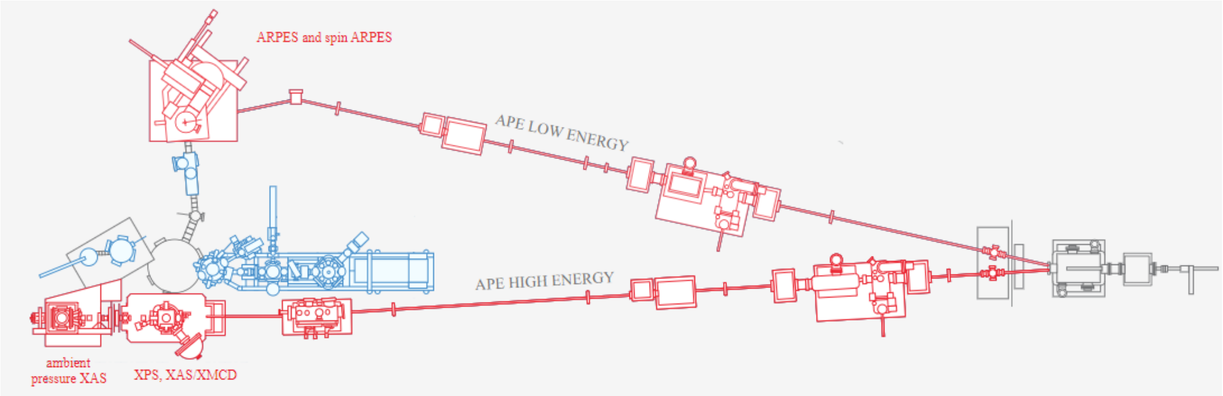

Figure 3.14: Graphical representation of HE and LE branches of APE beamline (Elettra experimental hall).

As it can be seen from Fig.3.14, the beams coming from the two undulators firstly reach a spherical mirror which deviates them in the respective HE and LE branches. The monochromators for both APE-HE and APE-LE are *Plane Grating Monochromators* (PGM) consisting in two chambers, one for gratings and one for spherical refocusing mirrors. The monochromator spherical mirror focuses the light on water cooled exit slits in the vertical plane; then the beam passes though refocusing stage before hitting the sample. In the refocus part LE branch uses a single toroidal mirror while HE has two of them, which can be moved independently in order to obtain different focusing options. At the APE-HE branch, a resolution power of $\frac{E}{\Delta E} > 8000$ at $h\nu \simeq 400eV$ and of $\frac{E}{\Delta E} > 3000$ at $h\nu > 900eV$ has been found, with a photon flux of $> 5x10^{-10}$ photons/s at best resolution in the range of $200 < h\nu < 450eV$.

3.2.1.2 Experimental setup for UHV measurements at APE-HE beamline

APE-HE end station is provided of UHV chamber, equipped with a 4 axis manipulator and an hemispherical electron energy analyzer. This chamber is used to perform NEXAFS/X-Ray Magnetic Circular Dichroism (XMCD)/XPS measurements in UHV conditions. It is built as a vibration-free sample chamber with mu-metal shielding for reducing the background H-field. The sample manipulator allows X-Y scanning on the surface with 1 μm precision and is therefore suitable to perform experiments on microstructures. It is possible to tune the sample temperature thanks to a He-flow cryostat and to a heating stage; moreover, it is possible to apply a magnetic field on the sample (up to 0.1 T) to perform XMCD measurements, and an electric field up to 500 V between contacted surfaces and substrate. For the NEXAFS and XMCD masuremenrs, The total electron yield (TEY) detection is achieved by measuring the drain current with a high sensitivity electrometer through shielded connections, or with an in vacuum electron multiplier. The total fluorescent yield (TFY) detection is achieved by an in-vacuum photodiode. The monochromator can be moved to performs photon energies scans (for NEXAFS and MXCD measurements). The movement can be done in two different modes, namely step-mode (the monochromator is moved at defined steps, and the spectrum is acquired at any step) or fast scan mode (the monochromator is moved continuously, allowing a faster spectra acquisition). Two independent electrical connections on the measuring position of the sample allow applying electric bias during or in-between the measurement. The possibility of combining electric and magnetic fields allows studying the chemical and magnetic behaviour of multiferroic materials and heterostructures.

For XPS measurements, a Scienta Omicron R3000 electron analyzer is mounted on the UHV chamber. The sample is usually measured in normal emission configuration, but the manipulator can be rotated in order to perform XPS measurements at different emission angles. The detector is made of a 2D delay line with a spatial resolution of 30 x 30 µm. The energy resolution that can be achieved using a pass energy of 50 eV is 50 meV.

3.2.1.3 Reaction cell for *Operando* NEXAFS at APE-HE beamline

The first prototype of the cell was developed in 2018, within the PRIN (*Progetti Di Rilevante Interesse Nazionale*) project MOSCATo[19]. It was designed to be inserted in the UHV end station of APE-HE beamline. The prototype was able to perform *operando* NEXAFS experiments, but it showed important limitations for the achievement of the real operating conditions of the catalysts inside the cell reactor. Since then, substantial modifications have been made, taking to a huge improvement of the instrument, which now is able to operate efficiently to perform experiments of great interest for the community working in the field of heterogeneous catalysis. A new dedicated chamber for the *operando* ambient pressure NEXAFS experiments has been built in 2021, shown in the right panel of Fig.3.15. The left panel of the figure shows the actual reaction cell.

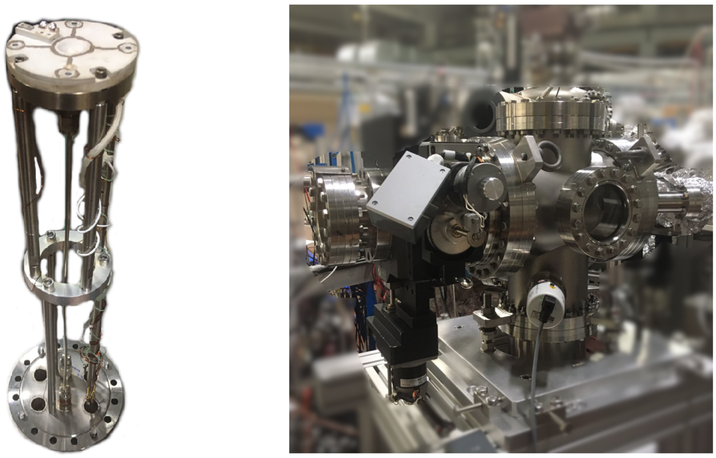

Figure 3.15: Left: reaction cell designed at the APE-HE beamline. Right: Picture of the new dedicated chamber for the *operando* ambient pressure NEXAFS experiments, on the APE-HE beamline.

The cell is introduced coaxially with the X-Ray beam and it can be moved in the xy plane perpendicular to it in order to center the sample (with a vectorial precision of $5\mu m$). The beam spot size can be mantained to less than $100\mu m$ of diameter, thanks to a double slit system placed at the beginning of the end station. Before the chamber there are two UHV valves devoted to separate the vacuum of the experimental chamber from the UHV of the beamline. The one closer to the experimental chamber is a gate valve used to preserve the UHV of the beamline while the chamber is vented; the one closer to the X-Ray source instead contains an X-Ray window, made of an array of 4x4 Si_3N_4 membranes (1mm x 1mm size, 50 nm thick), inserted in a supporting frame (10x10 mm size, 200 μm thick). The Si_3N_4 membranes are used because of their good soft X-Rays transmission[19] and to separate the vacuum between the experimental chamber ($\simeq 1x10^{-5}$ mbar) and the UHV of the beamline. The main disadvantage of these membranes is that by using them the K absorption edge of nitrogen can not be acquired, being covered by the Si_3N_4 window absorption. This problem can be solved by substituting the Si_3N_4 membranes array with SiC ones, which also have a good soft X-Rays transmission. Thus, closing the first valve allows to vent the chamber during the insertion of the reaction cell, while during the measurement it remains open and second one is closed. This configuration allows a fast replacing of the samples in the reaction cell; moreover, the Si_3N_4 window containing valve acts also as a "safety" valve in the case of any leak in the reaction cell, protecting the UHV of the beamline. In Fig.3.16 is depicted the new design of the top part of the reaction cell, which is the most important because it contains the reactor itself.

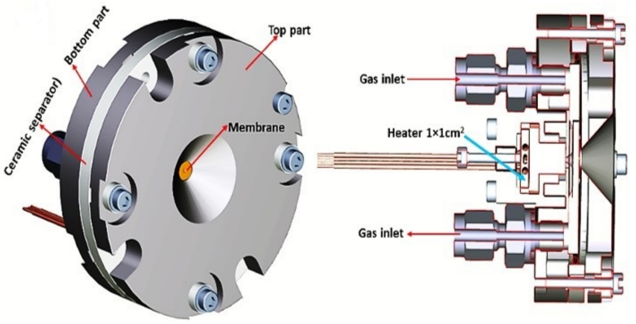

Figure 3.16: 3D model of the reaction cell. (left) front view, (Right) Vertical section.

The right panel shows the vertical section of the main body of the cell: the bottom part, made in Titanium, contains the sample holder and it is connected to the gas inlet and outlet conducts. The top part of the cell (visible in the left panel of Fig.3.16) is made of SHAPAL™, a chemically inert ceramic material, excellent electric insulator and compatible with UHV conditions. In the center of the top SHAPAL case, a Si_3N_4 membrane (500 μm x 500 μm size and 100 nm thickness supported by a frame of 10x10 mm size and 200 μm thickness) is glued with a silver conductive paste, which ensured the electrical conduction and a fast removal when the membranes are replaced. Concerning the Si_3N_4 membrane, the X-Ray transmission ranges between 40% to 80% in the soft X-Rays. Moreover, its resistance to 1 bar of differential pressure has been verified under under beam exposure and for several measuring cycles. With the above described configuration, a small volume is created between the top and the bottom part (of about 500 µm), which will be the proper reactor for the catalytic reactions, staying at ambient pressure (1 bar). Indeed, the reactant gases enter through the gas inlet and after reacting with the sample the products exit through the other gas conduct. In the meantime, the X-Ray beam passes through the Si_3N_4 membrane and the gas layer and hits the sample surface, which absorbs the radiation subsequently emitting photoelectrons. Fig.3.17 allows to visualize better the electrical scheme of the reaction cell.

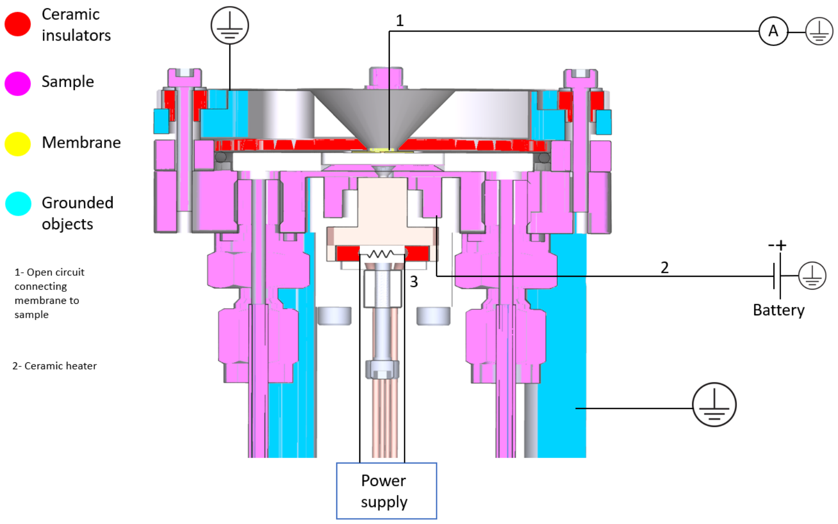

Figure 3.17: Scheme of the electrical circuits of the reaction cell.

The absorption intensity is measured by acquiring the TEY signal through two electrical contacts, represented by paths 1 and 2 in the scheme of Fig.3.17. The first one is connected to the Si_3N_4 membrane, while the second one is placed on the sample, allowing to apply a voltage bias between the sample and the membrane.

The two electrical contacts allow to polarize the sample negatively in order to accelerate the emitted electrons. The incoming of the X-Rays, and the consequent absorption processes occurring on the sample, give rise to a current of the order of pA going from the sample to the membrane; the membrane drain current is measured by a Keithley 6514 picoammeter[37]. When measuring the drain current, one has to take into account that, being in a reactor at 1 bar of pressure, there are also other sources of electrons. As depicted in Fig.3.18, firstly electrons are emitted when the beam hits the Si_3N_4 membrane, both when it passes through the vacuum/membrane and membrane/reactor interfaces. These photoelectrons can collide with the gas molecules present in the cell and also with the sample surface. Thus, the effective measured drain current can be evaluated as:

$$I_{DRAINSample} = I_{TEY,Sample} - I_{TEY,membrane} - I_{electronfromgas} + I_{ionsfromgas}, \quad (3.30)$$

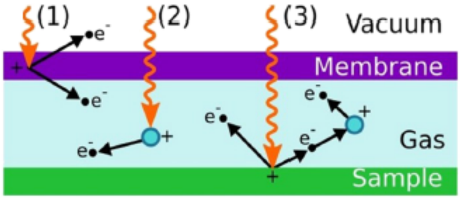

Figure 3.18: Scheme of all the secondary processes originated by the X-Ray beam interacting with the membrane (1), the gas (2), and the sample (3).

that is the sum of the TEY current from the sample ($I_{TEY,Sample}$) and of the various interference phenomena that we just mentioned. Since the absorption edges of the elements present in the membrane and in the gas in principle do not interfere with the edges of the chemical species of the sample and have constant cross sections, they should not modify the measured NEXAFS spectra and thus can be considered as constant in eq.3.30. Another phenomenon occurring during the absorption process is the avalanche of low energy electrons created by the collision of the photoemitted electrons with the reactant gases. This effect depends on the ionization energy of the gases, the gas pressure, and on the energy of the photoemitted electrons[38]. All this above-mentioned secondary effects contribute to possible high background levels in the NEXAFS spectra, with non-linear shapes, which can lead to difficulties in the data analysis. To this aim, in the context of the PRIN project a dedicated data analysis software called THORONDOR has been developed[39]. This software allows a quick treatment and analysis for the soft X-Rays NEXAFS data. The last problem that can arise from the TEY mode configuration of the reaction cell is related to the interference of the photoelectron current coming from fluorescence processes occurring at the membrane or at the gas molecules, but we verified that these contributions at the soft X-Rays energies can be neglected[19].

The temperature of the sample can be increased from room temperature up to 400°C, thanks to a flat ceramic heater placed just below the sample. The heater is 3mm thick and 8x8 mm large, with a maximum power of 150 W and it is electrically insulated from the main body of the cell (circuit 3 in Fig.3.17). The temperature is read by a K-type thermocouple in contact with the sample holder. Despite the electrical insulation, the heater sometimes can disturb the TEY signal when the drain current is measured by the Keithley attached to the sample: for this reason the signal is acquired from the electrical contact placed on the membrane.

Concerning the gas circuit (see Fig.3.19 in which is depicted the gas line configuration), there are three gas branches, each one equipped with a flow meter that serves to regulate different gas flows (two of them are general MF1, the third is suitable also for corrosive gases). After the flow meters the gases are mixed together to converge into a single conduit inside the cell.

One of these branches is used for the carrier gas flow (usually an inert gas with an high ionization potential, such as He), while the other two can be connected to small 1L bottles of the reactant gases[40]. Once they have entered the cell, the

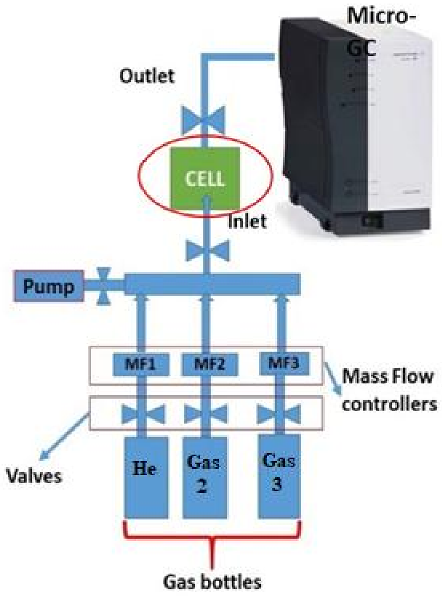

Figure 3.19: Scheme of the gas circuit at the APE-HE beamline for the *operando* NEXAFS measurements.

gases reach the reactor containing the sample. There, the catalytic reaction takes place and the gaseous products flow through an outlet gas line, which is directly connected to a micro gas cromatograph (Micro GC 490 Agilent). In this way, the outlet gases (and so the products of a possible catalytic reaction) are detected. The Micro-GC is equipped with two chromatographic column, one Molecular Sieve (used to detect light molecules such as H_2 and He), and one Volamine™(exploited to detect carbonaceous products such as methane, methanol or formaldheide). Each chromatographic column is equipped with a Thermal Conductivity Detector (TCD). The exhaust coming from the micro-GC is connected to the gas recuperation unit of Elettra experimental hall. The gas circuit is also connected to a membrane pump, for two main purposes: to measure XAS spectra in moderate vacuum conditions ($\simeq 1x10^{-3}$) and to purge the gas line when the experiment is finished. Finally, a liquid nitrogen trap has been mounted to the gas path line, allowing to remove water contaminations from reactant gases.

As already mentioned before, at the APE-HE beamline it is possible to use two different energy scan modes in order to acquire the NEXAFS spectra (both in UHV and *operando* conditions). The first one is the "step mode": the monochromator is moved with discrete steps, and at each of them the TEY intensity is acquired, repeating this operation for all the energy range to scan. This mode requires several minutes to acquire a good spectrum, and in order to follow the kinetics of a reaction it is too slow, thus for the *operando* XAS measurements the use of the "fast scan" mode is preferred. This acquisition mode consists of a continuous recording, reducing the acquisition time of more than one order of magnitude. The monochromator position is read by an optical encoder whose signal is synchronized with the measured one of the Keithley 6514 picoammeter.

Lastly, in order to be able to align the different absorption spectra that are acquired over time and can undergo rigid shifts in energy due to small drifts of the synchrotron photons energy, recently we coated a slit plate with a powder containing a mix of oxides. The plate is positioned in the X-Ray tube before the reaction cell, so as to be hit by the beam. The slit is connected to another picoammeter in order to collect at the same time a reference spectrum of the element of interest with the NEXAFS spectrum of the sample. In Fig.3.20 the available absorption edges references are reported.

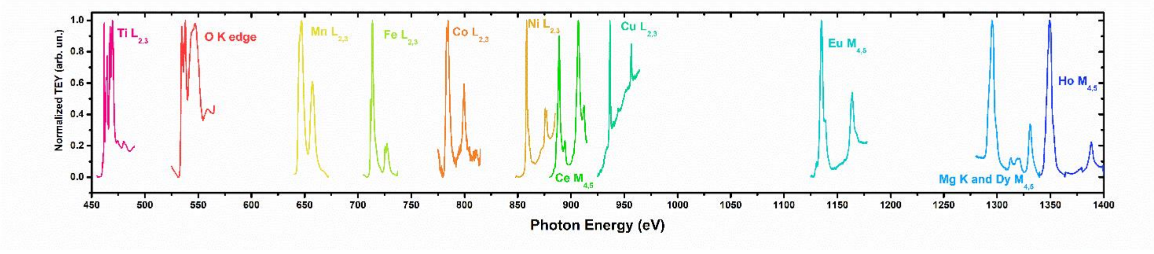

Figure 3.20: Absorption K, $L_{2,3}$ and $M_{4,5}$ edges spectra of the reference metal powders located on the slit in the X-ray tube of APE-HE end station.

3.3 Bibliography

[1] Frank De Groot. Core level spectroscopy of solids. crc press, boca raton. 01 2008.

[2] Yves Joly and Stéphane Grenier. *Theory of X-Ray Absorption Near Edge Structure*, chapter 4, pages 73–97. John Wiley & Sons, Ltd, 2016.

[3] Amphol Wongjamras, Alfred Schlachter, and Wayne Stolte. Progress of Soft-X-Ray Absorption Endstation for environmental samples. *Energy Procedia*, 9:56–62, 12 2011.

[4] R. Jenkins, R. Manne, R. Robin, and C. Senemaud. IUPAC—nomenclature system for X-Ray Spectroscopy. *X-Ray Spectrometry*, 20(3):149–155, 1991.

[5] Lei Jin and Ali Seifitokaldani. In Situ Spectroscopic Methods for Electrocatalytic CO_2 Reduction. *Catalysts*, 10(5), 2020.

[6] Stefano Turchini, Renaud Delaunay, Pierre Lagarde, Jan Vogel, and Maurizio Sacchi. Soft X-Ray Absorption spectroscopy in transmission mode: Ce $M_{4,5}$ edges. *Journal of Electron Spectroscopy and Related Phenomena*, 71(1):31 – 37, 1995.

[7] A. Ruosi, C. Raisch, A. Verna, R. Werner, B. A. Davidson, J. Fujii, R. Kleiner, and D. Koelle. Electron sampling depth and saturation effects in perovskite films investigated by Soft X-Ray Absorption Spectroscopy. *Phys. Rev. B*, 90(12):125120–, sep 2014.

[8] J. Stöhr. *NEXAFS spectroscopy.* Springer-Verlag, 1992.

[9] Yulong Zhang, Donglong Fu, Xingyan Xu, Yiyi Sheng, Jing Xu, and Yi fan Han. Application of operando spectroscopy on catalytic reactions. *Current Opinion in Chemical Engineering*, 12:1 – 7, 2016. Nanotechnology / Separation Engineering.

[10] Gabor A. Somorjai and Günther Rupprechter. Molecular Studies of Catalytic Reactions on Crystal Surfaces at High Pressures and High Temperatures by Infrared-Visible Sum Frequency Generation (SFG) Surface Vibrational Spectroscopy. *The Journal of Physical Chemistry B*, 103(10):1623–1638, 1999.

[11] Miguel A. Bañares. Operando methodology: combination of in situ spectroscopy and simultaneous activity measurements under catalytic reaction conditions. *Catalysis Today*, 100(1):71 – 77, 2005. 100th Anniversary Issue.

[12] Tadashi Okawa, Takaharu Onishi, and Kenzi Tamaru. Infrared and Kinetic Study of Ammonia Decomposition on Supported Iron Catalysts: Infrared Observation of Molecularly Adsorbed N_2 in Ammonia Decomposition. *Zeitschrift für Physikalische Chemie*, 107(2):239 – 243, 1977.

[13] A Knop-Gericke, M Hävecker, Th Neisius, and Th Schedel-Niedrig. New experimental technique: X-ray absorption spectroscopy detector for in situ studies in the soft X-ray range (250 eV $\leq$ hv $\leq$ 1000 eV) under reaction conditions. *Nuclear Instruments and Methods in Physics Research Section A: Accelerators, Spectrometers, Detectors and Associated Equipment*, 406(2):311 – 322, 1998.

[14] P. T. Kristiansen, T. C. R. Rocha, A. Knop-Gericke, J. H. Guo, and L. C. Duda. Reaction cell for in situ Soft X-Ray Absorption Spectroscopy and resonant inelastic X-Ray scattering measurements of heterogeneous catalysis up to 1 atm and ° C. *Review of Scientific Instruments*, 84(11):113107, 2013.

[15] Yusuke Tamenori. Electron yield Soft X-Ray Photoabsorption Spectroscopy under normal ambient-pressure conditions. *Journal of Synchrotron Radiation*, 20(3):419–425, May 2013.

[16] J. Forsberg, L.-C. Duda, A. Olsson, T. Schmitt, J. Andersson, J. Nordgren, J. Hedberg, C. Leygraf, T. Aastrup, D. Wallinder, and J.-H. Guo. System for

in situ studies of atmospheric corrosion of metal films using Soft X-Ray Spectroscopy and quartz crystal microbalance. *Review of Scientific Instruments*, 78(8):083110, 2007.

[17] Carlos Escudero, Peng Jiang, Elzbieta Pach, Ferenc Borondics, Mark W. West, Anders Tuxen, Mahati Chintapalli, Sophie Carenco, Jinghua Guo, and Miquel Salmeron. A reaction cell with sample laser heating for *in situ* Soft X-Ray Absorption Spectroscopy studies under environmental conditions. *Journal of Synchrotron Radiation*, 20(3):504–508, May 2013.

[18] J. J. Velasco-Velez, C. H. Wu, B. Y. Wang, Y. Sun, Y. Zhang, J.-H. Guo, and M. Salmeron. Polarized X-ray Absorption Spectroscopy Observation of Electronic and Structural Changes of Chemical Vapor Deposition Graphene in Contact with Water. *The Journal of Physical Chemistry C*, 118(44):25456–25459, 2014.

[19] C. Castán-Guerrero, D. Krizmancic, V. Bonanni, R. Edla, A. Deluisa, F. Salvador, G. Rossi, G. Panaccione, and P. Torelli. A reaction cell for ambient pressure Soft X-Ray absorption spectroscopy. *Review of Scientific Instruments*, 89(5):054101, 2018.

[20] David C. Grinter, Federica Venturini, Pilar Ferrer, Matthijs A. van Spronsen, Rosa Arrigo, Wilson Quevedo Garzon, Kanak Roy, Alexander I. Large, Santosh Kumar, and Georg Held. The Versatile Soft X-Ray (VerSoX) Beamline at Diamond Light Source. *Synchrotron Radiation News*, 35(3):39–47, 2022.

[21] Yi-Sheng Liu, Sohee Jeong, James L. White, Xuefei Feng, Eun SeonCho, Vitalie Stavila, Mark D. Allendorf, Jeffrey J. Urban, and Jinghua Guo. In-Situ/Operando X-ray Characterization of Metal Hydrides. *ChemPhysChem*, 20(10):1261–1271, 2019.

[22] Luca Braglia, Martina Fracchia, Paolo Ghigna, Alessandro Minguzzi, Daniela Meroni, Raju Edla, Matthias Vandichel, Elisabet Ahlberg, Giuseppina Cer-

rato, and Piero Torelli. Understanding Solid–Gas Reaction Mechanisms by Operando Soft X-Ray Absorption Spectroscopy at Ambient Pressure. *The Journal of Physical Chemistry C*, 124(26):14202–14212, 2020. PMID: 33815647.

[23] Alexander Gurlo and Ralf Riedel. In Situ and Operando Spectroscopy for Assessing Mechanisms of Gas Sensing. *Angewandte Chemie International Edition*, 46(21):3826–3848, 2007.

[24] Michael Hunger. In situ NMR spectroscopy in heterogeneous catalysis. *Catalysis today*, 97(1):3–12, 2004.

[25] J.F. Moulder and J. Chastain. *Handbook of X-ray Photoelectron Spectroscopy: A Reference Book of Standard Spectra for Identification and Interpretation of XPS Data*. Physical Electronics Division, Perkin-Elmer Corporation, 1992.

[26] Siegfried Hofmann. *Auger- and X-Ray Photoelectron Spectroscopy in Materials Science*, volume 49. 01 2013.

[27] Stefan Hüfner. *Very High Resolution Photoelectron Spectroscopy*, volume 715. 01 2007.

[28] S. Hüfner. *Unfilled inner shells: Transition metals and compounds*, volume 27, page 173. 1979.

[29] Stefan Hüfner. *Photoelectron spectroscopy: principles and applications; 3rd ed.* Advanced Texts in Physics. Springer, Berlin, 2003.

[30] Kai Siegbahn, Carl Nordling, and Anders Fahlman. ESCA, atomic, molecular and solid state structure studied by means of electron spectroscopy. Technical report, Almqvist and Wiksell, Uppsala, 1967.

[31] U Gelius. Binding energies and chemical shifts in ESCA. *Physica Scripta*, 9(3):133–147, mar 1974.

[32] MP Seah, D Briggs, and JT Grant. Quantification in AES and XPS in surface analysis by Auger and X-ray photoelectron spectroscopy. *Surface science spectra. IM, Chichester*, 345, 2003.

[33] T. A. Carlson. Basic assumptions and recent developments in quantitative XPS. *Surface and Interface Analysis*, 4(4):125–134, 1982.

[34] `https://vuo.elettra.eu/services/elements/WebElements.html`.

[35] Mark B. Mitchell. *Fundamentals and Applications of Diffuse Reflectance Infrared Fourier Transform (DRIFT) Spectroscopy*, chapter 13, pages 351–375.

[36] G Panaccione, I Vobornik, J Fujii, D Krizmancic, E Annese, L Giovanelli, F Maccherozzi, F Salvador, A De Luisa, D Benedetti, et al. Advanced photoelectric effect experiment beamline at Elettra: A surface science laboratory coupled with Synchrotron Radiation. *Review of Scientific Instruments*, 80(4):043105, 2009.

[37] `www.tek.com/keithley`.

[38] John Townsend. *The theory of ionization of gases by collision.* Constable, Limited, 1910.

[39] David Horst Simonne, Andrea Martini, Matteo Signorile, Alessandro Piovano, Luca Braglia, Piero Torelli, Elisa Borfecchia, and Gabriele Ricchiardi. *THORONDOR*: a software for fast treatment and analysis of low-energy XAS data. *Journal of Synchrotron Radiation*, 27(6):1741–1752, Nov 2020.

[40] `https://www.siad.com/`.

Chapter 4

Inverse ball milled $CeO_2 - CuO$ catalyst for partial oxidation of methane: a combined ***in situ*** DRIFT/***operando*** NEXAFS investigation

4.1 Introduction

The direct catalytic partial oxidation of methane to methanol, discussed in detail in section 2.3.1.1, is considered nowadays as a "dream reaction". Indeed, currently no scalable catalyst is able to efficiently promote the reaction at low temperatures, because of the high energy required to activate CH_4 and of the difficulty to obtain selectively the production of methanol avoiding the over oxidation of CH_4 to CO_2 and H_2O. The possibility to produce methanol from CH_4 through a direct route, without going through the production of syngas, would be extremely convenient from an energetic point of view, simultaneously contributing to eliminate a greenhouse gas. Even if at the state-of-the-art no efficient scalable catalyst has yet been discovered, in literature there are some promising studies on model systems; in particular, one of these works has been chosen as a starting point for the present study, a recent article by Zuo et al.[1], already described in detail in section 2.3.1.1. In the study, a CeO_2 film deposited on a Cu(111) substrate was grown through Pulsed Laser Deposition; as a consequence, a reactive Cu_2O monolayer formed at the interface between CeO_2 the Cu substrate. The resulting model system is called "Inverse" catalyst, because the oxide active phase is supported by a metal substrate, while the standard catalysts are usually designed at the opposite (oxide-supported metal nanoparticles). The material shown outstanding catalytic properties, being able to activate CH_4 at 170°C and in presence of an oxidizing agent obtaining high selectivity for the production of CH_3OH. The choice of using CeO_2 and Cu was made for specific reasons, elucidated hereafter. Cerium oxide (CeO_2) is a widely exploited material, due to its abundance in nature and to its outstanding oxygen storage capacity (OSC). The latter is caused by the easy tuning of the equilibrium of eq.4.1:

$$CeO_2 \rightleftharpoons CeO_{2-x} + 1/2O_2, \tag{4.1}$$

by modifying the external partial pressure of oxygen. The crystallographic structure of CeO_2 is crucial in defining its ionic mobility. Its unit cell is of the fluorite type, i.e. face-centered (fcc), with Ce cations bonded to eight nearest equivalent oxygen atoms, while O anions are tetrahedrally bonded to four Ce nearest neighbors (Fig.4.1 a)). This crystal structure can be seen also as a primitive cubic array of oxygen ions with alternated Ce cations in the centre, with an octahedral coordination (see Fig.4.1 b)). The empty octahedral sites are one of the main causes of the high mobility of oxygen ions through the defect structure[2].

In CeO_2, Ce cations possess a $+4$ oxidation state. The reduction from CeO_2 (Ce^{4+}) to Ce_2O_3 (Ce^{3+}), induced by the progressive shift to the right side of the equilibrium of eq.4.1, is accompanied by the formation of oxygen vacancies, pre-

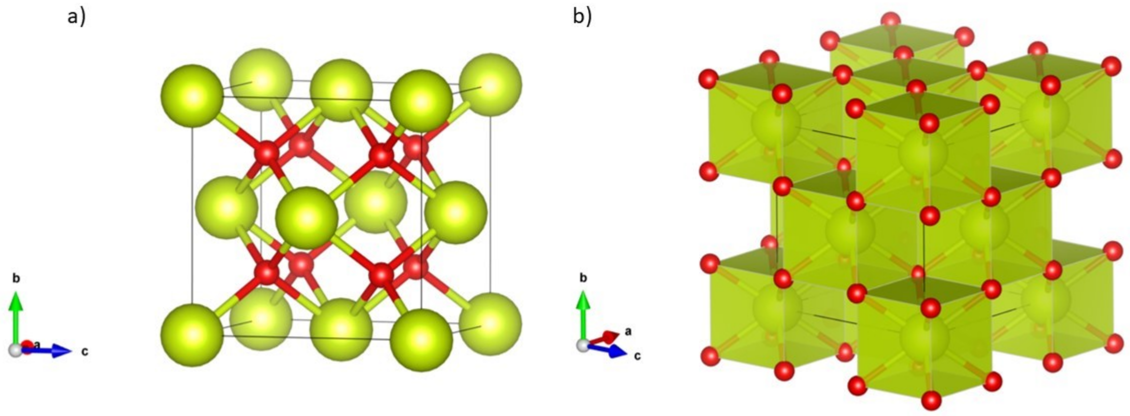

Figure 4.1: a) CeO_2 crystallographic unit cell; b) Same structure redrawn as a primitive cubic array of oxygen atoms.

serving the fluorite-type crystal structure[3]. A commonly used strategy to obtain a high number of oxygen vacancies and therefore of Ce^{3+} defective sites is to maximize the surface area, reducing the size of the crystallites[4–6]. The large diffusion capacity and the ability to supply oxygen atoms has made CeO_2 a material widely used as a support for metal particles[2,7,8], enhancing the so called Strong Metal-Support Interactions (SMSI). Indeed, It is well established that the SMSI at the interface between metal particles supported on oxides can improve the catalytic performance of a system[9], making metal supported oxides widely investigated materials in heterogeneous catalysis[10–13]. In order to further enhance the interfacial interactions between metal and oxides phases, efficient inverse catalysts can be synthesized[14,15].

Cu incorporation in CeO_2, and more in general the synergy between Cu and Ce atoms, has received considerable attention in catalysis[16], for a wide range of reactions, such as preferential CO oxidation (CO-PROX)[17–21], water-gas shift reaction[22–24], CO_2 hydrogenation to methanol[25,26], NO_x reduction[27,28]. The efficient catalytic performances of $CuO_x - CeO_2$ based catalysts are thought to be due to the synergistic effect linked to strong Copper–Ceria interactions. At the interface between CuO_x and CeO_2 surfaces, several phenomena can occur, with the consequence of modifying the overall catalytic activity. In detail, the binding interactions between Cu and Ce nanoparticles can result in surface chemistry modifications and/or perturbations of the electronic structure in proximity of the interface between the two oxides. For example, the increased charge mobility consequent to the interfacing of the two surfaces can induce the formation of $Ce^{3+} - Ce^{4+}$ / $Cu^{2+} - Cu^{+}$ redox couples. These electronic structure modifications can result in a facilitated formation of defects such as oxygen vacancies, and therefore a facilitated reducibility. Moreover, the charge transfer phenomena consequent to the interfacing can take to the formation of reactive sites resulting in enhanced catalytic activity. Depending on the systems, all these effects can cohexist. In the case of the model system synthetized by Zuo et al.[1], the deposition of CeO_2 islands on a $Cu(111)$ surface results in the formation of a monolayer of Cu_2O, where the interfacial Cu^{+} sites possess an enhanced reactivity towards the methane.

Having made these premises, it is therefore fundamental in order to be able to understand the catalyst surface behaviour from the reaction mechanism point of view, the use of *operando* spectroscopies coupled with classical characterization techniques, in order to investigate the structural/chemical/electronic modifications occurring at the real working conditions of the catalyst. The tuning of the morphological characteristic of the two oxides can significantly modify the kind of metal-support interactions: in this direction the employment of new synthetic routes could trigger unique opportunities towards the development of specific architecture catalysts possessing the desired properties. In this work, we tried to reproduce a CeO_2/CuO inverse catalyst with the characteristics of the model system synthetized by Zuo et al.[1], exploiting a ball milling process. The process is potentially scalable at the industrial level, moreover it is solvent free and thus it is in agreement with the principles of the green chemistry. The mechanochemical approach is extensively used to synthesize mixed oxides and alloys[29–32] and it already revealed to be successful for the synthesis of heterogeneous catalysts with improved catalytic efficiency with respect to the conventionally prepared metarials[33–36]. In this case, the idea behind the synthetic approach is to promote a $Cu^{2+} \rightarrow Cu^{+}/Ce^{3+} \rightarrow Ce^{4+}$ redox reaction induced during the milling process by the mechanochemical energy. In this way, we tried to reproduce the active interfacial Cu^{+} sites formed of the model system synthetized by Zuo et al.[1]. In order to achieve this goal, a commercial high surface area CeO_2 powder has been employed as a precursor, because of its increased Ce^{3+} surface sites content. In order to monitor the electronic structure modifications and the Cu-Ce synergistic effects occurred during the synthesis, Soft X-Ray NEXAFS spectroscopy has been exploited. Moreover, the catalyst morphology and structure have been characterized with X-Ray Diffraction (XRD) and Scanning Electron Microscopy (SEM). The combined spectroscopic investigation was performed in order to investigate at the same time:

- The electronic structure modifications of the catalyst surface during the reaction, by means of *operando* NEXAFS spectroscopy. The micro-GC directly connected to the *operando* NEXAFS reaction cell allowed to identify the different reaction products.
- The presence of adsorbates and their evolution in time when the catalyst is exposed to methane and oxygen, by means of *in situ* DRIFT spectroscopy;

In this way, we were able to directly observe the mechanism of methane activation and conversion to methanol on the surface of the ball milled CeO_2/CuO inverse catalyst. In order to be able to correlate the spectroscopic modifications and the catalytic behaviour to the specific mechanochemical process, we also tested a similar CeO_2/CuO catalyst synthesized with a conventional impregnation method. The spectroscopic results shown that the ball milled CeO_2/CuO, through the formation of peculiar active sites subsequent to the interfacing of HSA CeO_2 and CuO, is able to activate CH_4 and to promote its partial oxidation to methanol, detected by the online micro-GC. On the opposite, the impregnated CeO_2/CuO catalyst resulted to be totally inert to CH_4. These findings would not have been possible without the use of *operando/in situ* techniques, because all the catalyst modifications occurring during the reaction are completely reversible, and after every catalytic cycle the initial configuration of the material surface is restored. This last property is fundamental for an optimal functioning of an heterogeneous catalyst. Our results, supported by DFT calculations, allowed us to propose a mechanism model for the catalytic reaction and to lay the foundations for a design improvement of these promising catalysts.

4.2 Experimental

4.2.1 Catalysts synthesis

The synthesis of the inverse CeO_2/CuO catalysts studied in this thesis have been performed at the laboratories of Catalysis for Energy and Environment of the department of Engineering and Architecture of University of Udine.

4.2.1.1 Ball Milled CeO_2/CuO catalyst

The two precursors used for the ball milling synthesis are commercial CuO and CeO_2 powders, with a w/w ratio of 80:20 respectively. In particular, the CeO_2 employed is provided by Umicore® and has a surface area of 120 m^2/g. The CuO and CeO_2 precursors were pre-calcined at 600°C and 500°C respectively. Then the powders were homogenized and trasferred in a 15 mL jar containing one zirconia ball with a weight of 10 g and a diameter of 15 mm. The powders were milled for 10 minutes and with a shaking frequency of 15 Hz. The use of one single zirconia ball and a different shaking movement during the milling process differentiates this synthesis from the more common High Energy Ball Milling technique: Fig.4.2 graphically illustrates the main differences between the two techniques.

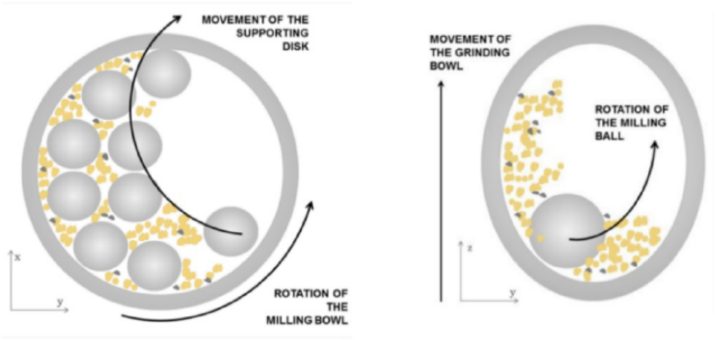

Figure 4.2: Left: graphic representation of the High Energy Ball Milling process; Right: graphic representation of the Mild Energy Ball milling process.

The soft shear-like stress generated by exploiting the mild energy ball milling process give rise to specific morphological features of the resulting composite material[37]; they will be deeply analyzed in the next sections for the CeO_2/CuO catalyst, which from now on in the text will be labeled as $MCeO_2/CuO$.

4.2.1.2 Impregnated CeO_2/CuO catalyst

A reference impregnated catalysts (labeled as $ICeO_2/CuO$) with the same weight percentages of the $MCeO_2/CuO$ was synthesized via impregnation technique. A proper amount of Cerium nitrate ($Ce(NO_3)_3 \cdot 6H_2O$) was dissolved in 45 mL of ethanol, in a 50 mL Becher. 750 mg of CuO where dispersed in the solution. Then, the solvent was evaporated by heating the resulting sospension at 60°C. The resulting black powder was dried at 100°C for 12 hours and then calcined at 400°C for 1 hour.

4.2.2 Experimental procedure for the *in situ/operando* characterization

The experimental procedure followed for the *in situ* DRIFT and *operando* NEXAFS characterization is schematically reported in Fig.4.3.

In detail, the experimental steps have been the following:

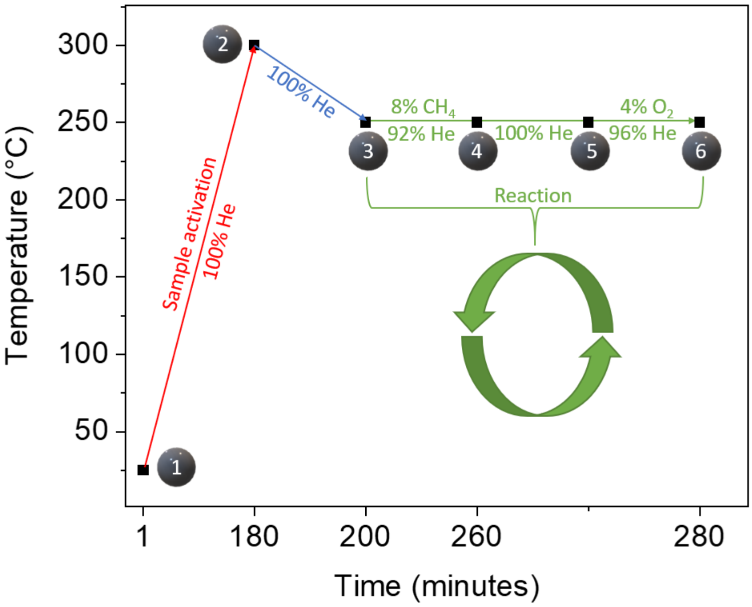

Figure 4.3: Experimental procedure scheme.

1. The catalyst was heated from room temperature to 300 °C in an inert atmosphere (100% of Helium);
2. After reaching 300°C, the sample was cooled down to 250°C, temperature to which it was maintained during all the successive steps;
3. The catalyst was exposed to a mixture of CH_4 (8%) and He (92%) for one hour;
4. CH_4 was removed, keeping only the He flux for 10 minutes;
5. The catalyst was exposed to a mixture of O_2 (4%) and He (96%) for 10 minutes.

After step 5, the process was restarted from step 3 to 6, repeating this cycle several times, in order to evaluate the reversibility of the observed spectral modifications, and thus the regeneration capacity of the catalyst surface. This procedure has been followed for the impregnated $ICeO_2/CuO$ and the ball milled $MCeO_2/CuO$ catalysts. During the entire experiment, the DRIFT and NEXAFS spectra have been acquired continuously. In detail, we acquired the $CuL_{2,3}$ and $CeM_{4,5}$ edges NEXAFS spectra, while detecting the reaction products with the online micro-GC (the experimental setup is described in detail in section 3.2.1.3), For the *In situ* DRIFT, the range of probed wave numbers was set from 500 to 4000 cm^{-1}.

Concerning the sample mounting, for both the *operando* NEXAFS and *in situ* DRIFT experiments, few milligrams of the CeO_2/CuO powders were manually pressed into a round sized sample holder, creating a pellet-like sample. The sample area exposed to the gas reactants were 11.94 mm^2 and 17.34 mm^2 for NEXAFS and DRIFT respectively.

4.3 Results and discussion

4.3.1 Morphological and structural characterization of CeO_2/CuO systems

4.3.1.1 X-Ray Diffraction (XRD) and Brunauer–Emmett–Teller (BET) analysis

An XRD analysis was performed for the $ICeO_2/CuO$ and $MCeO_2/CuO$ catalysts, together with the starting precursors used for the ball milled composite, i.e. the HSA CeO_2 and the CuO powders. Moreover, a Brunauer–Emmett–Teller (BET) analysis has been performed. This preliminary characterization allowed to obtain information about the bulk crystallographic structure of the catalysts, the crystallites dimensions, the pore sizes and surface areas. All the analysis reported in this subsection has been conducted at University of Udine.

The obtained XRD patterns are reported in Fig.4.4. Their analysis enabled us to attribute to both catalysts the fluorite structure of CeO_2 and of the monoclinic crystallographic unit cell of CuO, without impurities. The absence of shifts in the diffraction peaks of the two composites indicates that solid solutions are not formed during the synthesis. Another noteworthy observation regards the peaks width: the CuO related ones are sharp, while broader structures are detected for the CeO_2 related peaks in both catalysts. This result indicates an high crystallinity of the CuO particles, while for CeO_2 the peaks broadening is symptomatic of very small crystallites. The width difference between the two composites is determined by the different calcination temperature to which they were subjected during the synthesis (400°C and 500°C for $MCeO_2/CuO$ and $ICeO_2/CuO$ respectively).

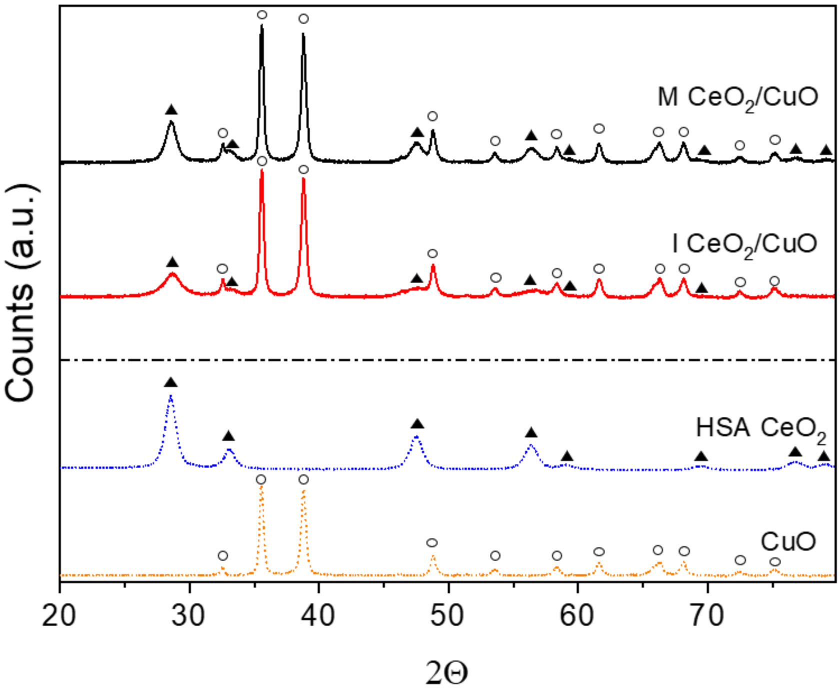

Figure 4.4: XRD pattern of $MCeO_2/CuO$ (black line) and $ICeO_2/CuO$ (red line) catalysts. In the lower part of the figure, the XRD pattern of the starting precursors for the ball milled CeO_2/CuO synthesis have been reported, i.e. CuO (orange dotted line) and HSA CeO_2 (blue dotted line).

Exploiting the Paul-Scherrer equation, the mean crystallites size for the two composites have been calculated. The results are reported in Tab.4.1, which summarizes all the morphological and structural properties found for the two catalysts. Looking at the table, we were able to confirm that the CuO crystallites are larger

Table 4.1: Summary of the morphological and textural properties of $MCeO_2/CuO$ and $ICeO_2/CuO$ catalysts, together with the CeO_2 and CuO precursors.

	$\mathbf{MCeO_2/CuO}$		$\mathbf{ICeO_2/CuO}$		$\mathbf{CeO_2}$	**CuO**
	CeO_2	CuO	CeO_2	CuO		
Crystallites size (XRD) (nm)	8.6	19.9	6.1	19.5	8.7	19.5
Particle size (SEM) (nm)	3000	58.49	2000	56.16	-	-
BET surface area ($\mathbf{m^2/g}$)	30.0*		20.0		120	10.0
Average pore diameter (nm)	180.0		26.6		72	35.1
Mean pore volume ($\mathbf{cm^3/g}$)	0.18		0.15		0.30	0.09

[*] The BET Surface Area, the Average Pore Diameter and the Mean Pore Volume resulted in only one value for $MCeO_2/CuO$ and $ICeO_2/CuO$, because these measurements are performed on the overall composite, without distinguishing the two oxides.

than the CeO_2 ones in the starting materials. The crystallites dimensions are mostly conserved after both the synthetic procedures, indicating that they did not affect the primary structure of the oxides. Concerning the BET surface area, the $MCeO_2/CuO$ catalyst shows values that reflect a weighted average between the two precursors areas. A clear difference between the two catalysts is observed when looking at the size of the pores: the $MCeO_2/CuO$ shows a macroporosity (180 nm of pore diameter), while the $ICeO_2/CuO$ is mesoporous (26.6 nm).

4.3.1.2 SEM analysis

Scanning Electron Microscopy (SEM) images have been acquired for the $MCeO_2/CuO$ and $ICeO_2/CuO$ composites. Panel a) and b) of Fig.4.5 show low magnified ($\sim 10kX$) images of $MCeO_2/CuO$ and $ICeO_2/CuO$ respectively, showing in both cases an inhomogeneous morphology. Nevertheless, for the ball milled catalyst we detect the presence of two types of particles with different morphological features.

In detail, nanoparticles with a mean size of 58.5 nm and bigger agglomerates of $\sim$ 3 μm. For the $ICeO_2/CuO$ catalyst we detect the same type of particles, albeit a lower density of the agglomerates, which are slightly smaller ($\sim$ 2μm). The mean size of the smaller nanoparticles in this case is 56.6 nm, very similar to the ones of the ball milled catalyst.

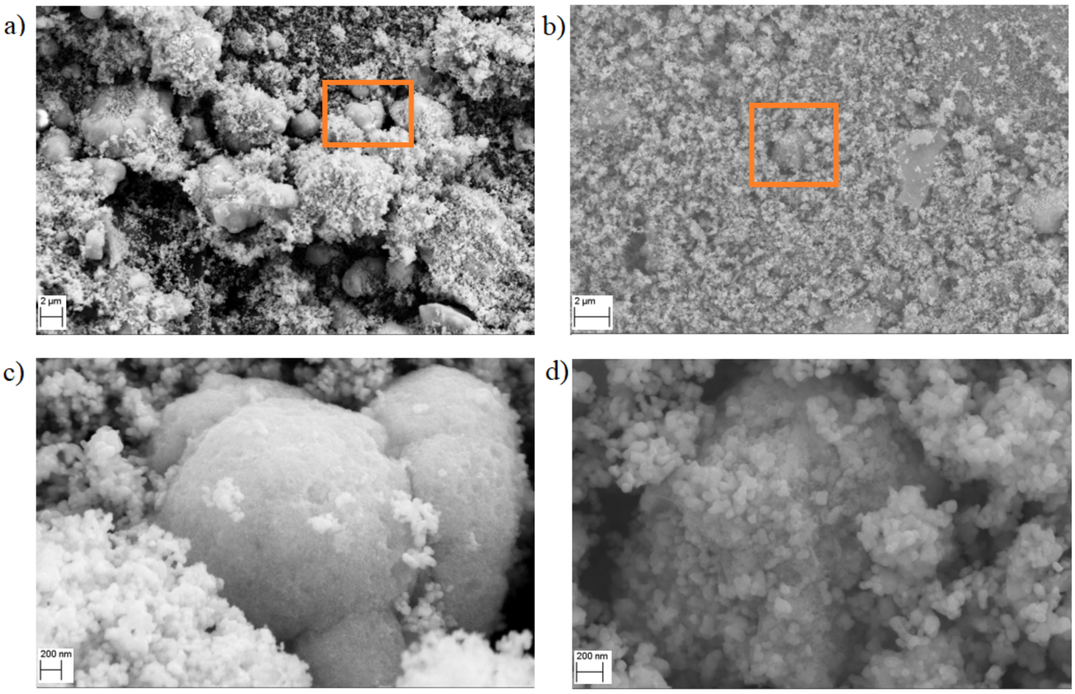

Figure 4.5: SEM images acquired for a) $MCeO_2/CuO$ and b) $ICeO_2/CuO$ catalysts. The orange boxes indicate the regions where the magnificated images have been acquired for c) $MCeO_2/CuO$ and d) $ICeO_2/CuO$.

The use of a backscattered electrons detector to acquire the SEM images allowed us to observe an evident contrast difference between the two kind of particles (see Fig.4.6), indicating different chemical composition (the clearer the image, the higher is the atomic number Z). This made us hypothesize that the smaller objects could be CuO nanoparticles, while the bigger ones could be agglomerates of CeO_2.

To confirm this hypothesis, an EDX analysis on three different regions of the $MCeO_2/CuO$ catalyst has been performed, shown in Fig.4.7. The first EDX

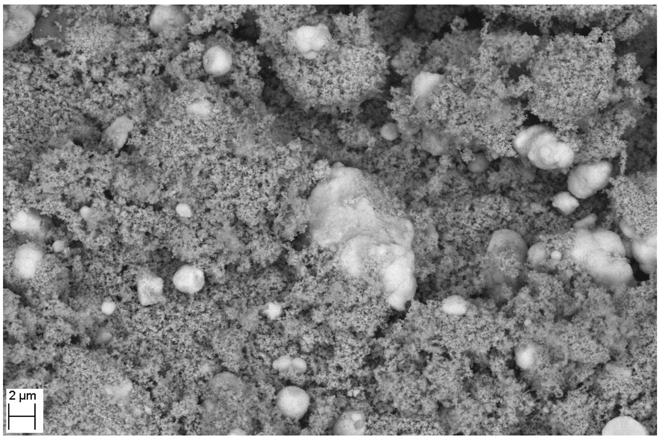

Figure 4.6: SEM image acquired for $MCeO_2/CuO$ using a backscattered electrons detector.

spectrum has been acquired on the clean surface of one of the brighter and bigger agglomerate, showing the presence of cerium and oxygen, with negligible Cu quantity, confirming that the bigger agglomerates are made up of CeO_2 crystallites. On the contrary, spectra 2 and 3, acquired on regions totally covered by the smaller and darker nanoparticles, confirmed their CuO nature (only Cu and O signals have been detected).

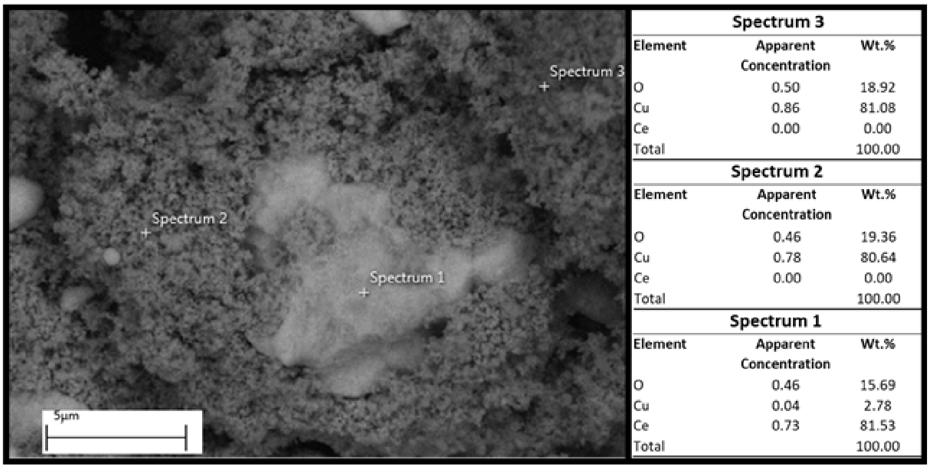

Spectrum 3

Element	Apparent Concentration	Wt.%
O	0.50	18.92
Cu	0.86	81.08
Ce	0.00	0.00
Total		100.00

Spectrum 2

Element	Apparent Concentration	Wt.%
O	0.46	19.36
Cu	0.78	80.64
Ce	0.00	0.00
Total		100.00

Spectrum 1

Element	Apparent Concentration	Wt.%
O	0.46	15.69
Cu	0.04	2.78
Ce	0.73	81.53
Total		100.00

Figure 4.7: Left: sample region employed to perform the EDX analysis, over three different points of the $MCeO_2/CuO$ catalyst, marked by a cross in the figure. Right: Table indicating the EDX results.

If one acquires magnified SEM images on the CeO_2 agglomerates for both catalysts (panels c) and d) of Fig. 4.5 and a) and b) in fig. 4.8) it can be observed that in both cases CuO nanoparticles are deposited on the CeO_2 agglomerates, with the difference that in the impregnated catalyst the NPs cover the entire CeO_2 surface (Fig.4.8 panel b)), while for the ball milled one it is possible to observe CuO-free areas on the cerium oxide (Fig.4.8 panel a)). Focusing on the latter, a porous CeO_2 surface is detected. This is in agreement with the BET results shown in Tab.4.1 and discussed above, where a macroporosity was found for the $MCeO_2/CuO$ catalyst.

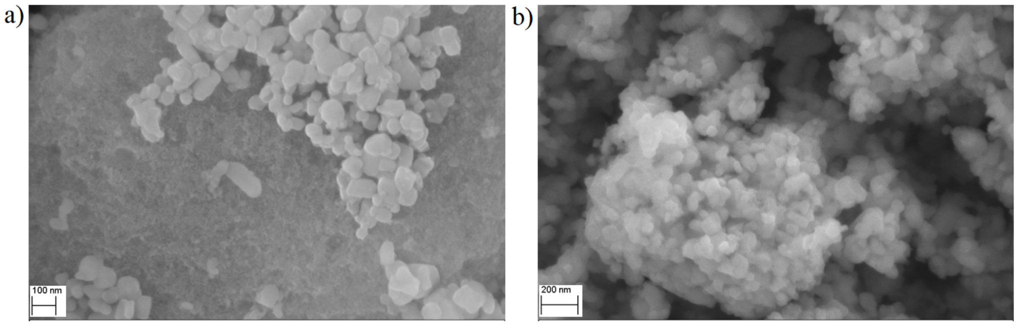

Figure 4.8: SEM images showing the deposition of the CuO nanoparticles on the CeO_2 agglomerates for a) $MCeO_2/CuO$ and b) $ICeO_2/CuO$ composites.

Summarizing, by combining the information obtained by SEM, XRD and BET analysis, we understood that the morphological properties of the two composites are very similar. In both cases, CeO_2 nanosized crystallites aggregates forming micrometric porous particles, with larger pores in the case of the ball milled catalyst. Also the CuO crystallites aggregates forming smaller nanoparticles which deposit on the porous CeO_2 agglomerates. These results show that the use of the mild energy ball milling technique resulted in a catalyst with similar morphology and structure with respect to the more conventional impregnated one.

4.3.2 Combined *in-situ* DRIFT / *operando* NEXAFS investigation

The electronic structure modifications occurring on the surface of the $MCeO_2/CuO$ and $ICeO_2/CuO$ catalysts during the experimental steps reported in Fig.4.3 have been monitored by means of *operando* Soft X-Rays NEXAFS spectroscopy at ambient pressure. The investigated absorption edges are the Cu $L_{2,3}$ and the Ce $M_{4,5}$. The online micro gas chromatograms allowed to detect the reaction products, making possible the identification of different methane oxidation paths. At the same experimental conditions, *in situ* DRIFT spectra have been acquired in order to investigate the evolution of the adsorbed species on the catalysts surface during the reaction. The combination of the two techniques allowed to directly observe the catalytic methane activation and the subsequent oxidation on the catalyst surface; with the help of DFT calculations, a tentative reaction mechanism model has been proposed.

4.3.2.1 Catalyst thermal activation

Fig.4.9 shows the Cu $L_{2,3}$ and the Ce $M_{4,5}$ X-Ray absorption edges acquired for the $ICeO_2/CuO$ and the $MCeO_2/CuO$, together with the spectra of the ball milled catalyst precursors (i.e. HSA CeO_2 and the CuO). The spectra have been acquired at room temperature, at ambient pressure (1 bar), in an inert atmosphere of Helium (step 1 of the experimental procedure described in section 4.2.2) .

The Cu $L_{2,3}$ edges spectra of the three samples show the same features and are almost superimposable. They consist of two intense peaks located at 931.05 eV and 951.68 eV, characteristic of the $2p_{3/2} \rightarrow 3d$ and $2p_{1/2} \rightarrow 3d$ electronic core excitation of copper atoms with a $+2$ oxidation state[38–40]. The intensity of these structures is related to different phenomena, of which the more relevant is the dipole selection rule (described in section 3.1.1.1): Cu^{2+} electronic structure ($[Ar]3d^9 4s^0$) shows an empty $3d$ orbital, and therefore a certain $2p \rightarrow 3d$ transition

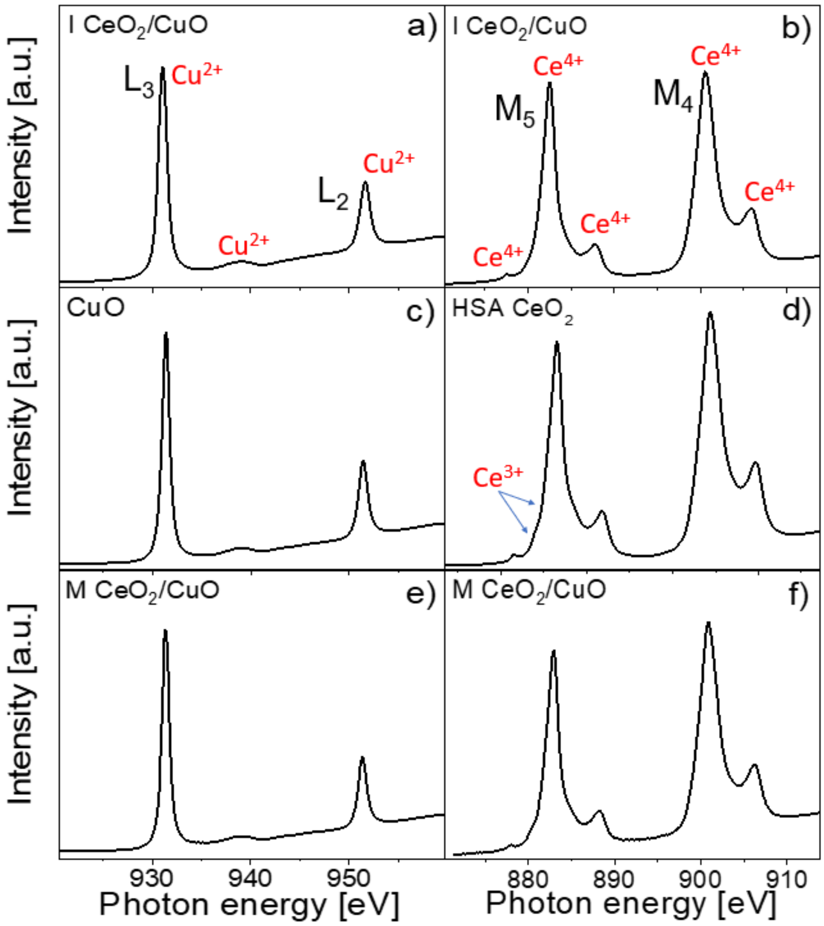

Figure 4.9: Left panels: Cu $L_{2,3}$ edges NEXAFS spectra of a) $ICeO_2/CuO$, c) CuO nanoparticles used as precursors and e) $MCeO_2/CuO$. Right panels: Ce $M_{4,5}$ edges NEXAFS spectra of b) $ICeO_2/CuO$, d) HSA CeO_2 used as precursor and f) $MCeO_2/CuO$. In red, the characteristic features of Cu^{2+}, Ce^{4+} and Ce^{3+} are indicated.

probability. The position of the intense white-line of Cu^{2+} is located at consistently lower photon energies with respect to the XPS treshold, indicating strong core-hole effects due to the Coulomb interaction between the strongly localized 2p hole and the rather small Cu 3d orbital[38]. Another broad structure typical of Cu^{2+} compounds is detected at 939.0 eV, assigned to $2p \rightarrow 4s$ electronic transitions[41]. The overall analysis of the peaks position and shape allow to assign the Cu^{2+} cations of the spectra of Fig.4.9 to the chemical environment and local geometry of CuO[38], in agreement with the fact that CuO nanoparticles have been used to synthetize both the $ICeO_2/CuO$ and the $MCeO_2/CuO$ composites.

For what concerns the $CeM_{4,5}$ edges spectra (right panels of Fig.4.9), some differences have been detected between the three samples. The $ICeO_2/CuO$ material shows the characteristic spectroscopic features of CeO_2, with Ce atoms having a $+4$ oxidation state. In detail, M_5 absorption edge gives rise to one main feature located at 882.47 eV, while for the M_4 an intense structures is located at 900.53 eV; they are related to $3d^{10}_{5/2}4f^0 \rightarrow 3d^9_{5/2}4f^1$ and $3d^{10}_{3/2}4f^0 \rightarrow 3d^9_{3/2}4f^1$ transitions respectively; the energy difference between them is 18.04 eV, slightly higher with respect to values reported in literature[42,43]. Both edges show a structure at higher photon energies ($+5.34$ eV for M_5 and $+5.29$ eV for M_4), attributed to transitions to 4f states in the conduction band[42]. Moreover, for the M_5 edge another weak structure located at 877.4 eV is detected, according to literature related to Ce^{4+}, but with an uncertain attribution[42,43]. Looking at the spectrum of the HSA CeO_2 (Fig.4.9 panel d)), in addition to the Ce^{4+} peaks, two shoulders appear at lower photon energies with respect to the main Ce^{4+} structure, at 880.4 eV and 881.5 eV, attributable to Ce^{3+} features[44]. The corresponding structures on the M_4 edge are not visible because of their weak intensity compared to the nearly superimposed Ce^{4+} features. The same shoulders have been detected for the $MCeO_2/CuO$, indicating the presence of a small percentage of Ce^{3+} sites also in the composite. We tried to quantify the Ce^{3+} content in the HSA CeO_2 and in the $MCeO_2/CuO$, performing a linear combination fit on the CeM_5 edge, using reference spectra of CeO_2 and Ce_2O_3 measured on APE-HE beamline as independent variables in the fitting function (eq.4.2):

$$LC = C1 \cdot a + C2 \cdot b, \tag{4.2}$$

where a and b are the reference spectra of CeO_2 and Ce_2O_3, while $C1$ and $C2$ are multiplicative constants of a and b, whose values define the percentage of the two species in the fitted spectrum (LC). Two constraints have been defined for $C1$ and $C2$, i.e. i) $C1 + C2 = 1$ and ii) $0 \leq C1 \leq 1$ and $0 \leq C2 \leq 1$. The result obtained for the HSA CeO_2 (Fig.4.9 panel d)) is graphically shown in Fig.4.10, where an amount of 6% of Ce^{3+} sites have been found.

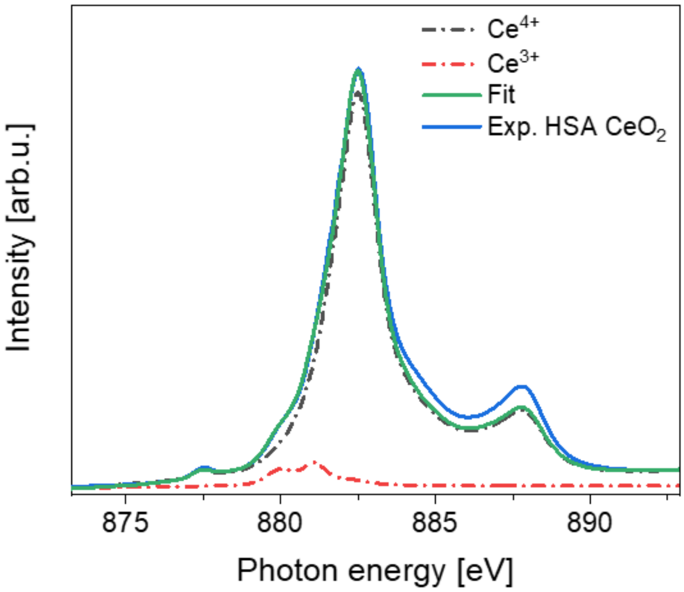

Figure 4.10: Solid blue line: CeM_5 edge NEXAFS spectrum acquired at room temperature for the HSA CeO_2. Solid green line: linear combination fit, using CeO_2 (black dotted) and Ce_2O_3 (red dotted) reference spectra acquired on APE-HE beamline.

As it can be observed in the figure, the linear combination fit has a very good agreement with the experimental spectrum, especially in the range between 875 eV and 885 eV, where the main features of Ce^{3+} are located. Using the same equation

(4.2), the calculated amount of Ce^{3+} sites in the $MCeO_2/CuO$ composite is 2.5%.

Summarizing the results found looking at the spectra of Fig.4.9, the following statements can be done:

- In the two composites, Cu atoms maintain the oxidation state and the same coordination environment of the CuO nanoparticles used as precursors for both synthetic methods, confirming the XRD results;
- We verified that the $Ce(NO_3)_3 \cdot 6H_2O$ used as precursor for the synthesis of the $ICeO_2/CuO$ catalyst, that is a compound where Ce has nominally a $+3$ oxidation number, was totally decomposed to pure CeO_2 during the calcination step, since no Ce^{3+} features have been detected. This is in agreement with the XRD findings, confirming that also the surface of the catalyst is clean from $Ce(NO_3)_3 \cdot 6H_2O$ impurities;
- The HSA CeO_2 used for the synthesis of the $MCeO_2/CuO$, as expected, shows a small amount of Ce^{3+} sites on its surface (6%), being a defect-rich material; after the ball milling synthesis, only 2.5 % of the Ce^{3+} sites are still present. This result indicate a partial Ce oxidation occurred during the ball milling synthesis; nevertheless, at this stage we do not detect a redox reaction between Ce and Cu, since Cu^+ sites formation is not detected.

The next step of the experiment (step 2 of Fig.4.2.2) was the thermal activation of the catalysts, that were heated from room temperature to 300 °C, with a consequent cooling to 250 °C, temperature at which the methane oxidation reaction was performed.

Fig.4.11 reports a comparison between the NEXAFS spectra acquired at room temperature and at 250 °C, after the thermal activation at 300°C. In the figure, we focused our attention on the Cu L_3 and the Ce M_5 absorption edges. Starting from the $ICeO_2/CuO$ composite (panels a) and b)), we did not detect any spectral

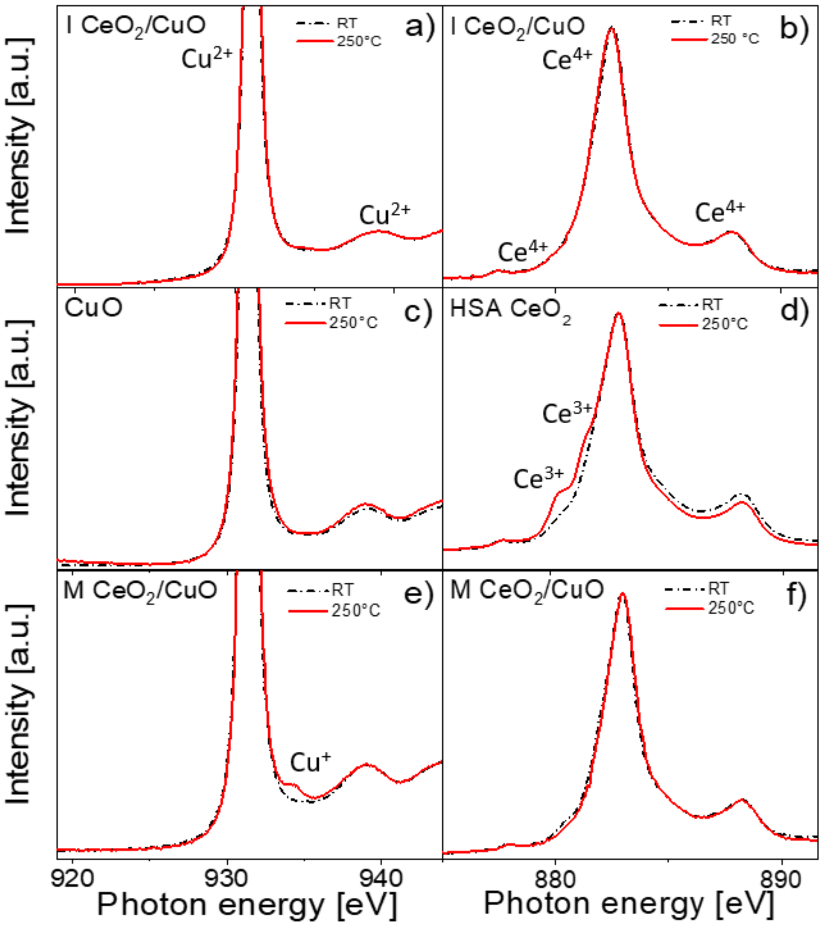

Figure 4.11: Left panels: Cu L_3 edge NEXAFS spectra of a) $ICeO_2/CuO$, c) CuO nanoparticles used as precursors and e) $MCeO_2/CuO$. Right panels: Ce M_5 edge NEXAFS spectra of b) $ICeO_2/CuO$, d) HSA CeO_2 used as precursor and f) $MCeO_2/CuO$. Dotted black lines: spectra acquired at room temperature; red lines: spectra acquired at 250°C after the thermal activation to 300°C.

modification for both Cu and Ce edges after the thermal treatment, i.e. only spectral features related to Cu^{2+} and Ce^{4+} are present. If we look at the spectra of the ball milled catalyst precursors (panels c) and d)), no modifications upon heating are visible for the CuO nanoparticles, while a $Ce^{4+} \rightarrow Ce^{3+}$ reduction is observed for the HSA CeO_2. It is probable that the thermal treatment to 300°C can induce the desorption of surface adsorbed hydroxyles in the form of water, forming oxygen vacancies and as a consequence Ce^{3+} sites. This behaviour has already been observed precedently in other CeO_2 based systems[45]. Exploiting the linear combination fit of eq.4.10, we calculated a Ce^{3+} amount of 11% after the thermal treatment. Surprisingly, an opposite behaviour was detected for the Ce sites of the $MCeO_2/CuO$: the initial 2.5% of Ce^{3+} sites are oxidized to Ce^{4+} during the thermal treatment. At the same time a new feature appears at 934.2 eV, ascribable to Cu^{+}[40,41] (panel e) of Fig. 4.11), whose calculated amount is 3%, similar to the one of the initial Ce^{3+} sites. Nevertheless, in the case of Cu a quantitative determination of different oxidation states based on the NEXAFS white lines intensity is very delicate. This is due to the electronic configuration of copper: since the NEXAFS L edges probe mainly the $2p \rightarrow 3d$ transitions and Cu^{+} has nominally no empty $3d$ orbitals, its L edge transitions should be quenched. An exhaustive explanation of the white line intensity of Cu_2O has not yet been given: theoretical studies[4039] show that probably the strong hybridization between the O $2p$ and the Cu $3d$ orbitals in Cu_2O result in partially empty $3d$ states in the conduction band, in this way increasing the the XAS $2p \rightarrow 3d$ transition probability. It is therefore very difficult to determine a cross section value for Cu_2O L edges. For this reason, the values obtained through the linear fit process, reported in Tab.4.2 and in the next section, can only be interpreted qualitatively to compare different stages of Cu reduction. In the case of Ce M edges, the cross sections of Ce^{4+} and Ce^{3+} are more similar due to their electronic configuration, since the $4f$ orbitals are almost completely empty for both ions. For this reason, the quantitative results obtained from Ce M edges spectra can be considered as a more precise measure.

Table 4.2: Summary of the Ce $M_{4,5}$ and Cu $L_{2,3}$ edges quantitative analysis during the thermal activation process.

	CuO		**HSACeO$_2$**		**MCeO$_2$/CuO**		**ICeO$_2$/CuO**	
%	RT	250 °C	RT	250 °C	RT	250 °C	RT	250 °C
Ce^{3+}	-	-	$6 \pm 1 \cdot 10^{-4}$	10.9 ± 0.4	2.5 ± 0.2	0	0	0
Ce^{4+}	-	-	$94 \pm 1 \cdot 10^{-4}$	89.1 ± 0.4	97.5 ± 0.2	100	100	100
Cu^{2+}	100	100	-	-	100	97.0 ± 0.27	100	100
Cu^{+}	0	0	-	-	0	3.0 ± 0.27	0	0

Looking at the results of Fig.4.11 and Tab.4.2, the ball milling process resulted in a rearrangement of the charge distribution in the formed composite. In detail we observe that the amount of initial Ce^{3+} sites is converted to Cu^{+} sites consequently to a redox reaction occurring during the thermal activation. In HSA CeO_2, when oxygen vacancies are formed consequently to the heating process, the two electrons coming from the release of the oxygen atom are able to reduce two Ce^{4+} neighbouring atoms to Ce^{3+}, in agreement with literature[2,46]. In the ball milled CeO_2/CuO composite, the different observed behaviour made us hypothesize that the strong $Ce - Cu$ interactions formed during the milling process give rise to a new charge transfer channel in the direction of copper atoms, that are reduced to Cu^{+}. These $Cu - Ce$ interactions are specific of the synthetic method used, since the $ICeO_2/CuO$ does not behave in the same way.

4.3.2.2 Methane activation

After the thermal activation, the interaction between the composites and methane has been followed by *operando* NEXAFS and *in situ* DRIFT spectroscopies. The catalysts were exposed to a CH_4 (8%)/He (92%) mixture for 60 minutes (step 3 of the experimental procedure represented in Fig.4.2.2).

Operando NEXAFS Fig.4.12 shows the Cu L_3 edge NEXAFS spectral evolution (looking from the bottom to the top of the figure) of the two composites during the exposure to the He/CH_4 mixture at 250 °C.

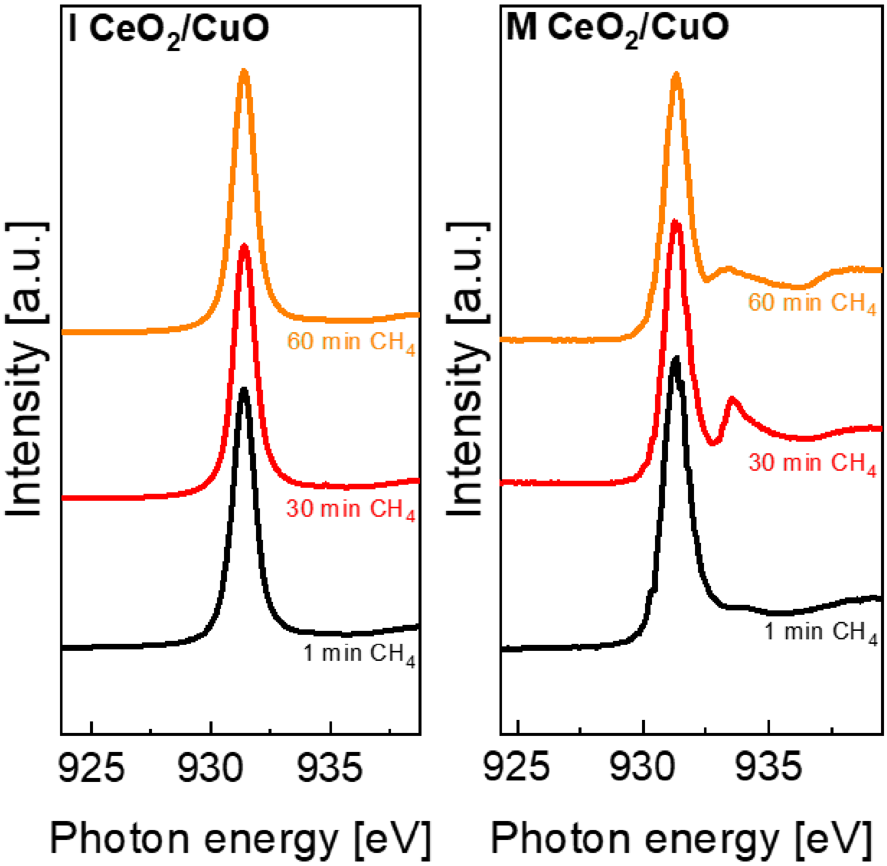

Figure 4.12: Cu L_3 edge NEXAFS spectra evolution (from the bottom to the top) of $ICeO_2/CuO$ (left) and $MCeO_2/CuO$ (right) composites during their exposure to a $He(92\%)/CH_4(8\%)$ mixture for 60 minutes, at 250 °C.

The spectra of the $ICeO_2/CuO$ do not change during the exposure to methane, meaning that Cu^{2+} atoms local chemical environment is preserved. On the opposite, important spectral modifications are detected in the $MCeO_2/CuO$ composite: the Cu^{+} related structure grows, reaching a maximum of intensity after 30 minutes of methane exposure, then it becomes broader and decreases its intensity reaching a stationary shape after 60 minutes. These results clearly indicate that CH_4 perturbs the chemical environment of Cu atoms only in the $MCeO_2/CuO$ catalyst, resulting in the reduction of a consistent amount of sites. The quantification of formed Cu^+ atoms through linear combination fitting indicates that the 18% of the total Cu^{2+} sites are reduced to Cu^+ after 30 minutes (red spectrum of Fig.4.12). The position of the Cu^+ peak is slightly shifted to lower photon energy with respect to Cu_2O white line, indicating that the reduced Cu atoms formed due to methane activation on the catalyst surface have a different chemical environment with respect to the standard Cu_2O. Moreover, modifications in the peak intensity and broadening over time indicates that the local chemical environment of the active Cu atoms evolves, until a definitive adsorption configuration of methane is reached (after 60 minutes). The reduced Cu calculated percentage at this stage (orange spectrum of Fig.4.12) reaches the 30%. As already discussed in the previous sections, these numbers can be interpreted only qualitatively, indicating that during the CH_4 exposure the quantity of reduced Cu sites increases over time.

Ce $M_{4,5}$ edges spectra do not change upon CH_4 exposure in both catalysts (Fig.4.13), maintaining the characteristic features of CeO_2.

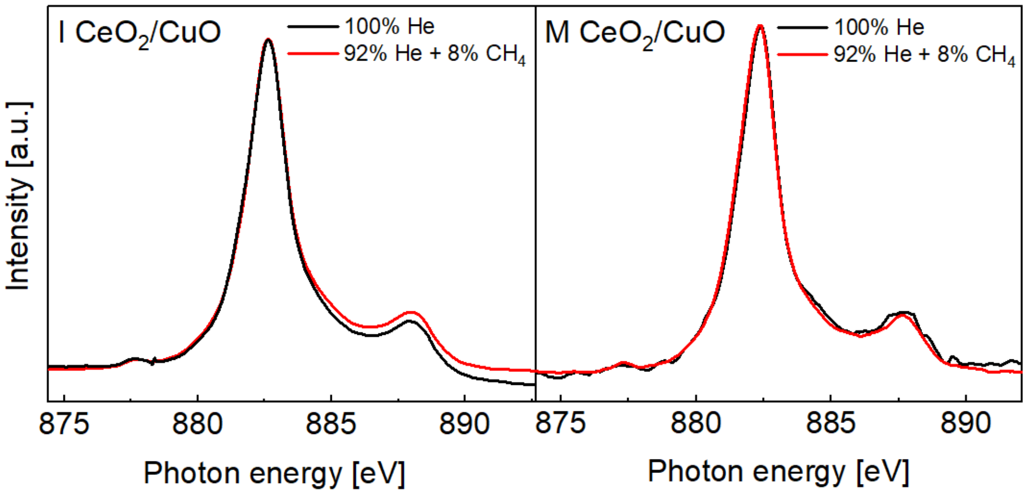

Figure 4.13: Ce M_5 edge NEXAFS spectra of $ICeO_2/CuO$ (left) and $MCeO_2/CuO$ (right) composites during their exposure to a $He(92\%)/CH_4(8\%)$ mixture for 60 minutes, at 250 °C. Black lines: spectra acquired in pure He(100%); red lines: spectra acquired in $He(92\%)/CH_4(8\%)$ mixture.

The NEXAFS results of Fig.4.12 and 4.13 show unequivocally that $ICeO_2/CuO$ electronic structure is unchanged upon exposure to methane, while for $MCeO_2/CuO$ catalyst the electronic structure is perturbed by an increased electron density in proximity of Cu atoms, causing a Cu reduction.

In situ DRIFT To further elucidate how methane activates on the $MCeO_2/CuO$ catalyst surface, DRIFT spectra have been acquired at the same experimental conditions of Fig.4.12 spectra, i.e. exposing the sample to a $He(92\%)/CH_4(8\%)$ mixture for 60 minutes. The results are shown in the top panel of Fig.4.14. The same experiment has been repeated for the $ICeO_2/CuO$ composite and for the two $MCeO_2/CuO$ precursors (bottom panel of Fig.4.14).

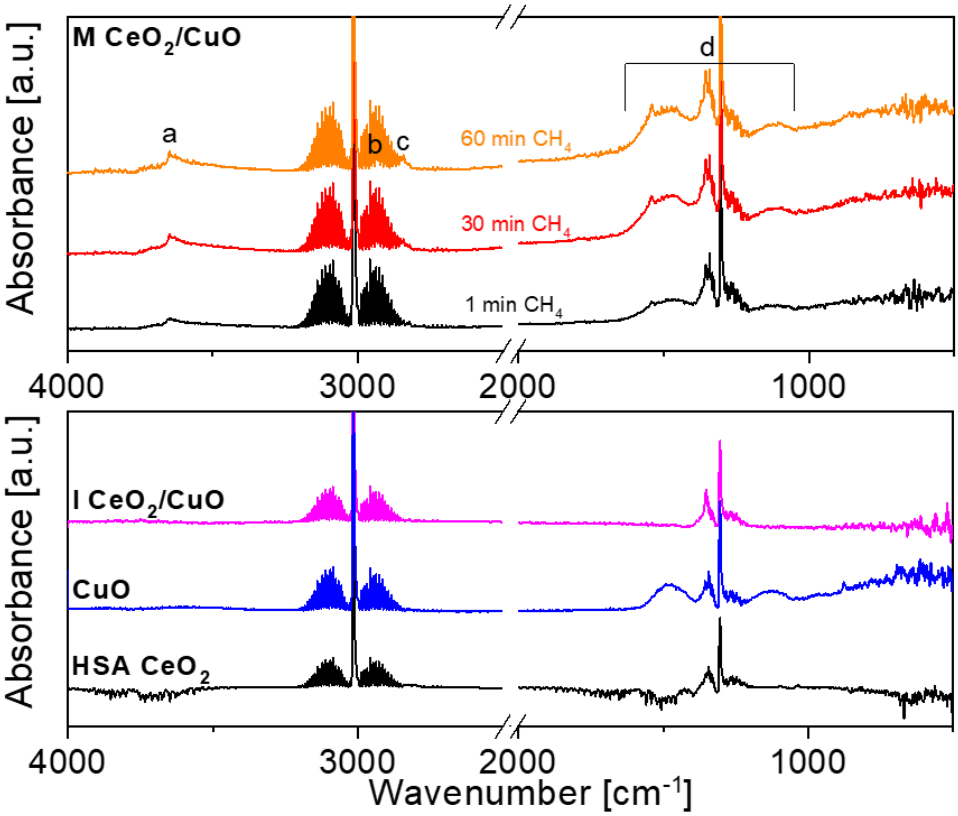

Figure 4.14: DRIFT spectra of $MCeO_2/CuO$ (top) and $ICeO_2/CuO$, HSA CeO_2 and CuO (bottom) during their exposure to a $He(92\%)/CH_4(8\%)$ mixture for 60 minutes, at 250 °C. The spectra of the bottom panel have been acquired after 60 minutes of CH_4 exposure.

Table 4.3: Assignments of vibrational modes visible in the DRIFT spectra of Fig. 4.14 according to literature[47–53].

Peak	Adsorbed species	Wavenumber (cm^{-1})	Vibrational mode
a	Hydroxy (-OH)	3650	Stretching O-H
b	Formate (-OOCH)	2931	Stretching C-H
c	Methoxy (-OCH$_3$)	2842	Stretching C-H
d	Formate (-OOCH)	1541	Stretching C-O
	Methoxy (-OCH$_3$)	1371	Bending C-H
	Methoxy (-OCH$_3$)	1355	Bending C-H
	Hydrogen Carbonate (HCO$_3^-$)	1308	Bending C-H

The spectra were collected by subtracting the background signal at the temperature of 250°C under pure He. All the spectra of Fig.4.14 present a complex structure centered at $\simeq 3000cm^{-1}$, that is the characteristic vibrational structure of gas phase CH_4[54]. Focusing on the $MCeO_2/CuO$ spectra, we observe the growing of different structures during the exposure to CH_4, labeled with $a-d$ letters in the figure. Looking at the peaks assignments of Tab.4.3, we observe that upon CH_4 exposure oxygenated adsorbates (formates, methoxy ad hydrogen carbonates) are formed on the catalyst surface, implying that CH_4 is activated on oxygen atoms of the composite. Moreover, literature data confirms that the observed vibrational modes are specific of a CeO_2 substrate[47–53]. All the detected adsorbates come from a partial CH_4 deprotonation, and could be possible intermediates of partial methane oxidation products; in particular, the methoxy moiety is a methanol intermediate. The observation of peak **a** growth (referred to the O-H stretching of hydroxyles) indicates that CH_4 is deprotonated by other oxygen atoms. The peak position (3650 cm^{-1}) is slightly shifted to higher wavenumbers with respect to the one reported in literature for CeO_2 substrates[48]; the shift indicates that the

O atoms responsible of CH_4 deprotonation have a chemical environment partially different to the one of pure CeO_2.

The results described above made us hypothesize that CH_4 molecules are activated by oxygen atoms that are peculiar of the $MCeO_2/CuO$ composite. This hypothesis is supported by the DRIFT spectra reported in the bottom panel of Fig.4.14: indeed, hydroxy and methoxy species are not formed upon CH_4 exposure for HSA CeO_2, CuO and $ICeO_2/CuO$. Only carbonates species are detected (peak at 1308 cm^{-1}). The structural position of the active O atoms able to deprotonate the CH_4 is difficult to assign, but combining the information obtained by NEXAFS and DRIFT spectra we can conclude that:

- The consequence of the CH_4 adsorption is the reduction of part of the Cu^{2+} sites;
- The deprotonated CH_4 is adsorbed on CeO_2, but it does not affect its electronic structure;
- The reactive O atoms able to activate methane are located close to the CeO_2 surface, but they are not stardand CeO_2 oxygens.

These results made us hypotesize that the reactive O atoms could be located in proximity of specific Cu-Ce interfaces formed during the ball milling process. The formation of -OH species, observed in DRIFT spectra, is likely to take place at the interface between CeO_2 and CuO, and can be than responsible of the Cu reduction in NEXAFS spectra of Fig.4.12. It is important to underline that the reactive $Ce-Cu$ interfaces are synthesis-specific, because detected only in the ball milled sample, probably formed due to the mechanochemical energy given to the composite during the milling process.

4.3.2.3 Methane oxidation

As indicated in steps 4 and 5 of the schematic experimental procedure of Fig. 4.2.2, after 60 minutes methane is removed keeping the samples under a pure Helium flow; then, the materials were exposed to a $He(96\%)/O_2(4\%)$ mixture for 10 minutes, in order to oxidize the adsorbed methane.

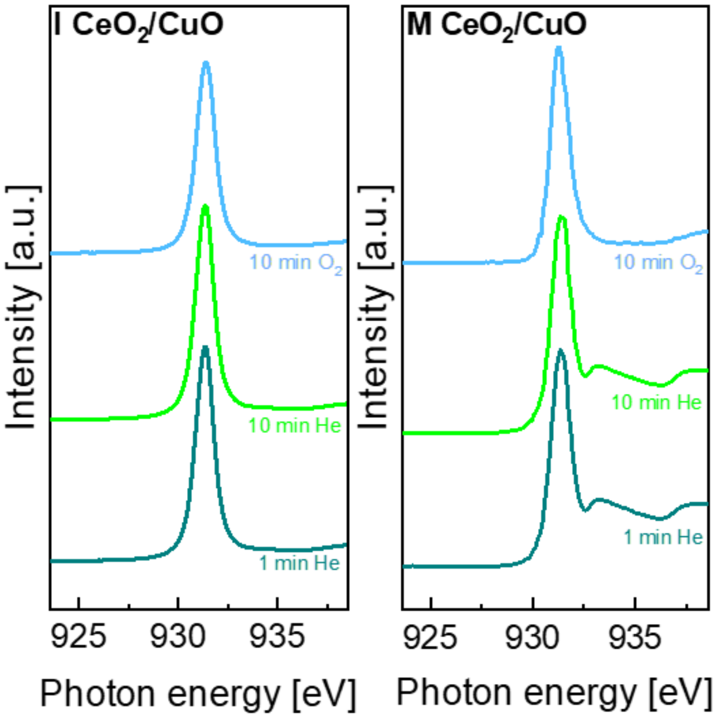

Figure 4.15: Cu L_3 edge NEXAFS spectra evolution (from the bottom to the top) of $ICeO_2/CuO$ (left) and $MCeO_2/CuO$ (right) composites during their exposure to He(100%) after being exposed to a $He(92\%)/CH_4(8\%)$ mixture for 60 minutes (green spectra) and consequently to a $He(96\%)/O_2(4\%)$ mixture for 10 minutes (blue spectra), at 250 °C.

***Operando* NEXAFS** Fig.4.15 shows the Cu L_3 edge spectra acquired during the above mentioned experimental steps. After removing CH_4 from the reaction mixture we observe that the structure related to reduced Cu sites, located at $\simeq$ 933 eV, is still present in the NEXAFS spectra of the $MCeO_2/CuO$ composite, maintaining a stationary shape and intensity. This means that the activated CH_4

is adsorbed on the catalyst surface, taking to an irreversible perturbation of the local chemical environment of part of Cu surface sites. When the $He(96\%)/O_2(4\%)$ mixture is introduced in the reaction cell, after 10 minutes the structure is totally disappeared, meaning that the reduced Cu sites are re-oxidized to the initial Cu^{2+} electronic configuration. This behaviour suggests that the oxidizing agent (O_2) is able to promote the desorption of the activated CH_4, restoring the initial electronic configuration of the catalyst surface. Ce M_5 edge spectrum does not change upon oxidation, as shown in Fig.4.16, meaning that Ce sites maintain a $+4$ oxidation state during all the reaction steps. Concerning the $ICeO_2/CuO$ composite, no spectral modifications at the Cu L_3 edge are detected (left panel of Fig.4.15), confirming the total absence of surface chemical reactivity and once again the outstanding synthetic-specific reactivity found for the $MCeO_2/CuO$ material.

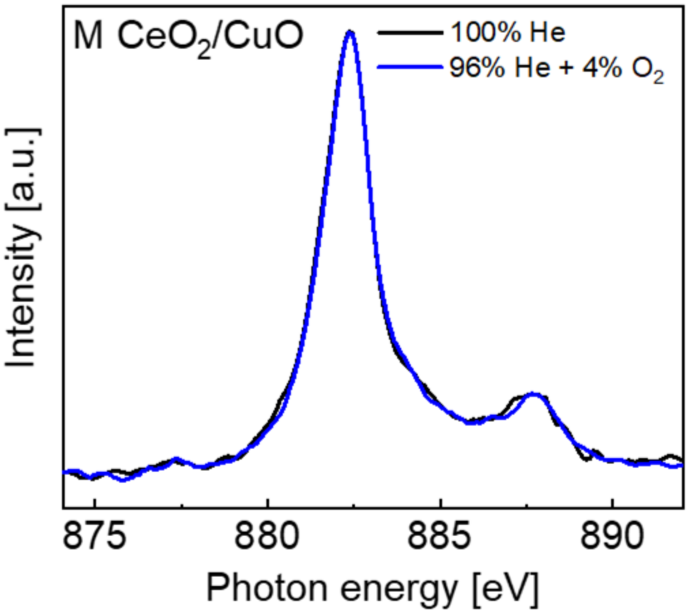

Figure 4.16: Ce M_5 edge NEXAFS spectra (from the bottom to the top) of $MCeO_2/CuO$ composite during its exposure to He(100%) after being exposed to a $He(92\%)/CH_4(8\%)$ mixture for 60 minutes (black spectrum) and consequently to a $He(96\%)/O_2(4\%)$ mixture for 10 minutes (blue spectrum), at 250 °C.

***In situ* DRIFT** The behaviour of the DRIFT spectra of the $MCeO_2/CuO$ during steps 4 and 5 of the experiment (Fig.4.17) is closely relatable to the one we observed in the NEXAFS spectra of Fig.4.15. After CH_4 is removed from the reaction mixture keeping a He(100%) flow (green spectra of Fig.4.17), we observe that the structures related to hydroxy, methoxy and formates species (peaks a,b,c and d) are still present in the spectra with the same intensity reached after 60 minutes of CH_4 exposure. Once again, this result confirms that methane is still activated and adsorbed on the catalyst surface. An interesting observation can be done looking at the peak located at 1308 cm^{-1}, assigned to hydrogen carbonates; in fact, its intensity consistently decreases after CH_4 is removed from the reaction mixture (and continues to decrease after 10 minutes of 100% He exposure), indicating that most of the carbonates are loosely bound to the catalyst surface and are desorbed much more easily than the other species. When the $He(96\%)/O_2(4\%)$ mixture is introduced in the reaction cell, all the DRIFT peaks related to adsorbed species disappear already after 10 minutes, confirming that the activated CH_4 is desorbed, promoted by oxygen atoms, restoring a clean catalyst surface.

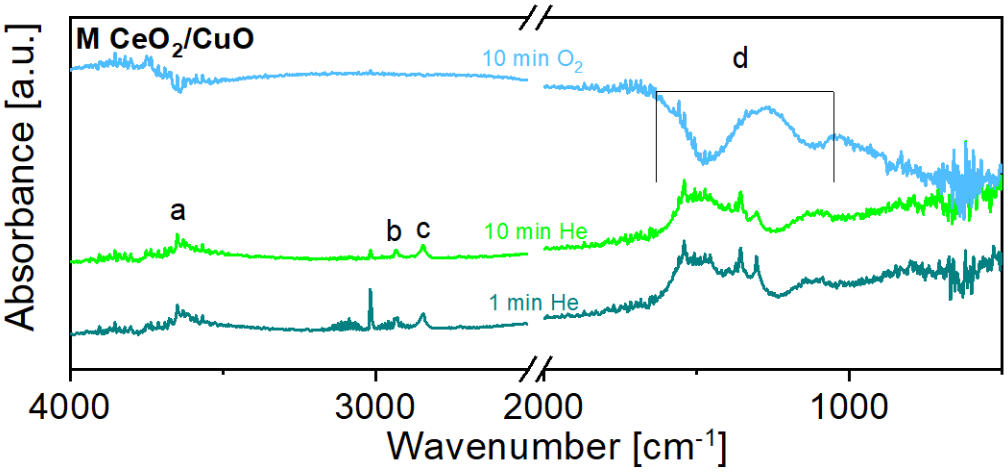

Figure 4.17: DRIFT spectra of $MCeO_2/CuO$ during its exposure to He(100%) after being exposed to a $He(92\%)/CH_4(8\%)$ mixture for 60 minutes (green spectra) and consequently to a $He(96\%)/O_2(4\%)$ mixture for 10 minutes (blue spectrum), at 250 °C.

4.3.2.4 Micro-GC results

The analysis of the micro chromatograms acquired during the *operando* NEXAFS experiment while the $MCeO_2/CuO$ catalyst was exposed to $He(92\%)/CH_4(8\%)$ and $He(96\%)/O_2(4\%)$ mixtures allowed us to detect the reaction products formed during the methane catalytic oxidation.

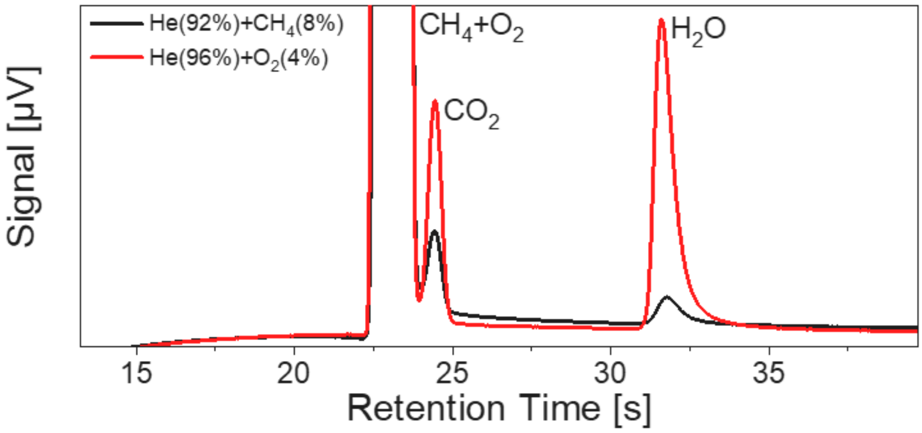

Figure 4.18: Micro gas chromatograms acquired during the $MCeO_2/CuO$ catalyst exposure to $He(92\%)/CH_4(8\%)$ (black line) and $He(96\%)/O_2(4\%)$ (red line) gas mixtures, at 250 °C.

Fig.4.18 shows the main signals detected for a retention time range between 15 and 50 seconds. Besides the signals of CH_4 and O_2 reactants that overlap at $\simeq$ 24 s, we observe a certain amount of CO_2 ($\simeq$ 25 s) and H_2O ($\simeq$ 32 s) already when the catalyst is exposed to CH_4; the two signals increase consistently when the reaction mixture is switched to an oxidizing atmosphere. The presence of CO_2 and H_2O in $He(92\%)/CH_4(8\%)$ environment confirms that hydrogen carbonate species (HCO_3^-), weakly adsorbed on the catalyst surface, are desorbed in the form of carbon dioxide and water; more in general, the source of H_2O come from the hydroxyles formed as a consequence of CH_4 deprotonation. When oxygen is introduced in the reaction cell, the content of produced CO_2 is more than doubled, while H_2O signal is ten times more intense. In this case, carbon dioxide and water production indicate that the total oxidation of methane is occurring (eq.4.3):

$$CH_4 + 2O_2 \rightarrow CO_2 + 2H_2O \tag{4.3}$$

Another source of water can also come from the partial oxidation of methane to formaldehyde (eq.4.4):

$$CH_4 + O_2 \rightarrow CH_2O + H_2O \tag{4.4}$$

In fact, if we zoom on the 20-50 s range of the chromatograms, we detect the presence of formaldehyde at 28.7 s. Moreover, at 41 s another peak is present when oxygen is introduced in the reaction cell, that corresponds to methanol. This means that also a direct partial oxidation of methane to methanol occurred (eq.4.5):

$$CH_4 + 1/2O_2 \rightarrow CH_3OH \tag{4.5}$$

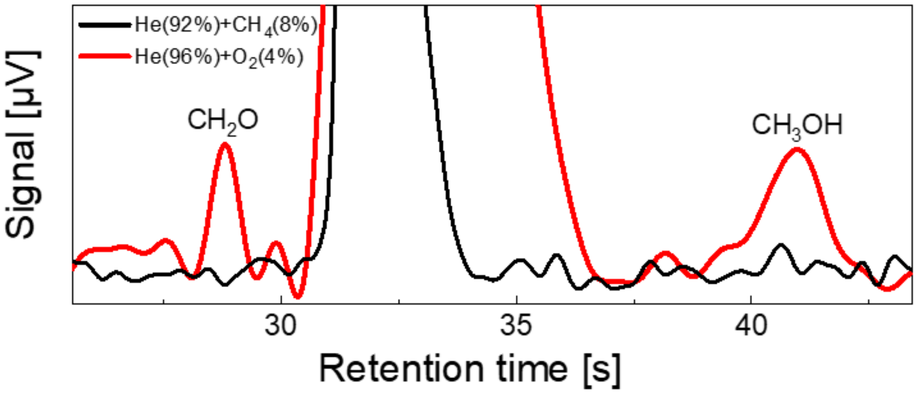

Figure 4.19: Zoom on the methanol and formaldheide region (20-50 s) of the micro gas chromatograms of Fig.4.18.

The micro-GC results have been used qualitatively to address the different reaction paths occurring during the reaction, understanding that methane undergoes in parallel to total and partial oxidation. This means that the selectivity of the $MCeO_2/CuO$ catalyst is not optimized, even if the detection of the methanol signal is an important result. We were not able to extrapolate quantitative values from the micro gas chromatograms shown in Fig.4.18 and 4.19 for two main reasons: *i)* the micro-GC has not been calibrated with standard gas mixtures prior to the experiment, thus we are not able to correlate a peak area with a defined quantity of produced gas; *ii)* the experimental setup used for the *operando* NEXAFS experiment is not the most suitable for products quantification, because the gas mixtures flow tangentially to the sample (detailed information is given in the subsection 3.2.1.3), therefore only the surface of the catalyst and not its entire volume is exploited during the catalytic reaction.

4.3.3 DFT calculations

This section briefly describes part of the results obtained by the DFT simulations performed in collaboration with the group of Dr. Stefano Fabris. The complete discussion of the results will be reported in the PhD thesis of the person in charge of the calculations. They are focused on the modeling of stable CeO_2/CuO interfaces that could be formed as a result of the ball milling process, responsible of the methane activation and oxidation. This first step of calculations has been done using Artemis software[55]. Then, energies of vacancy formation have been calculated using QUANTUM ESPRESSO code[56], comparing the values obtained for the $MCeO_2/CuO$ interfaces with the starting precursors, i.e. HSA CeO_2 and CuO. Moreover, charge transfers phenomena upon merging of CeO_2 and CuO surfaces have been investigated. In this way, we were able to validate the experimental observations made with NEXAFS, in which we observe a charge transfer from Ce to Cu atoms consequently to the milling process in the $MCeO_2/CuO$ catalyst.

Based on the formation energies, the two most stable CeO_2/CuO interfaces have been chosen, graphically represented in Fig.4.20.

They were obtained merging CeO_2 (110) + CuO (110) and CeO_2 (111) + CuO (-111) surfaces respectively. Moreover, for each interface two kind of CeO_2 have

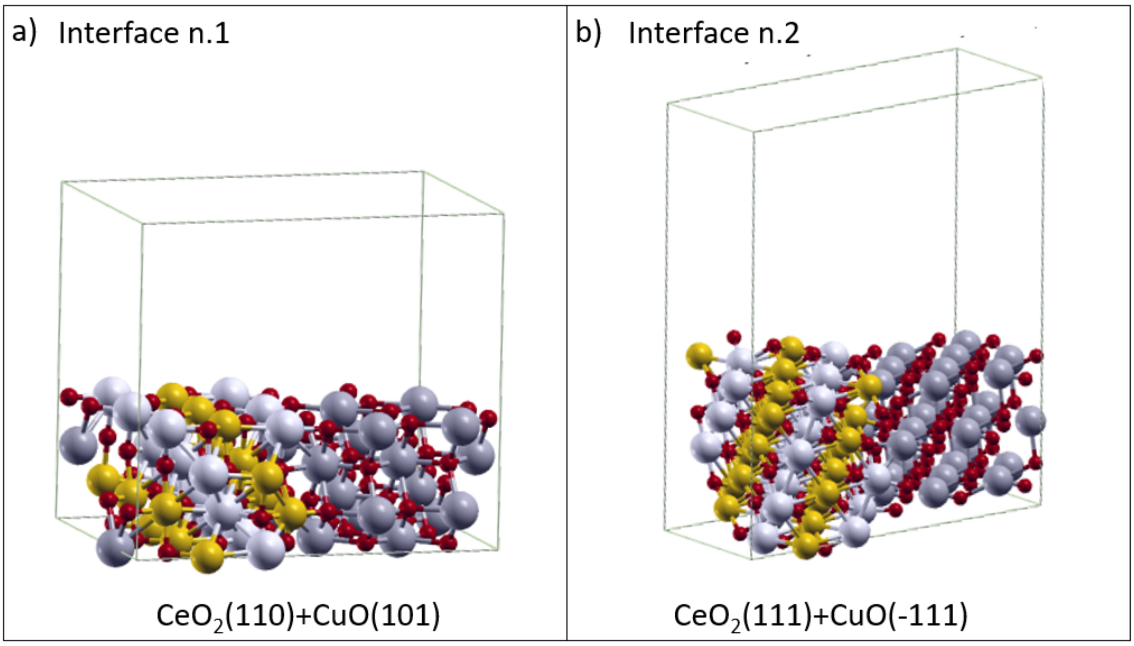

Figure 4.20: Graphic representation of the two interfaces chosen to perform the DFT calculations.

been considered: the stoichiometric one (CeO_2^s), where all the oxygen vacancies are occupied by atoms, and a defective one (CeO_2^v), where oxygen vacancies are present on the surface. This differentiation was done in order to simulate the different synthetic method employed, i.e. the impregnation (CeO_2^s) and the ball milling (CeO_2^v, since an high surface area cerium oxide has been employed). Fig. 4.21 shows the calculated charge transfer occurred during the formation of the composites, i.e. after the merging of the two oxides.

In the figure, x axis represents the charge variation while y axis is the distance from the interface (that is located at 8 Å). At z $\leq$ 8 there is the CeO_2, at z $\geq$ 8 the CuO. In panel a), stoichiometric CeO_2 has been employed, while in panel b) the defective one. In both cases, the merging of the two surfaces causes a charge transfer from CeO_2 to CuO, that is much more pronounced when defective CeO_2^v is employed, especially in proximity of the interface. This result confirmed what we observed in the NEXAFS spectra, where in the ball milled sample the amount of Ce^{+3} sites after the synthesis is halved with respect to the pure HSA CeO_2.

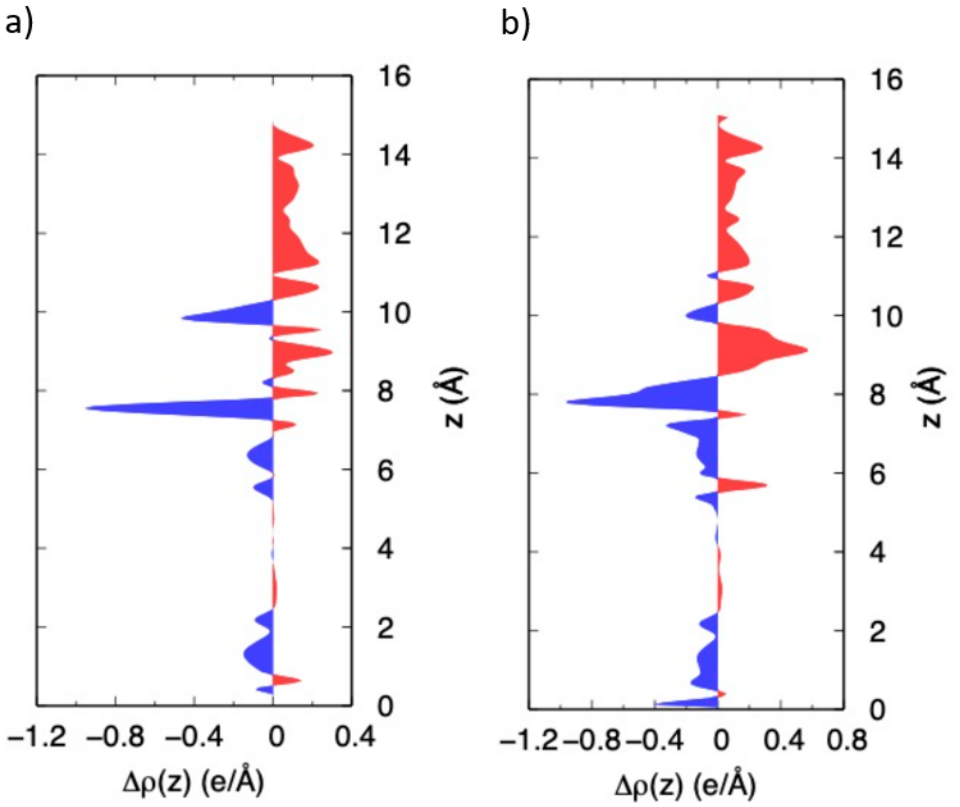

Figure 4.21: Graphic representation of the charge transfer occurred consequently to the merging of a) Stoichiometric CeO_2 (111) and CuO (-111) surfaces; b) Surface defective CeO_2 and stoichiometric CuO (-111) surfaces.

Table 4.4: Calculated energies for vacancy formation of the two interfaces of Fig.4.20 compared with pure CeO_2 and CuO surfaces

Interface n.1		**Interface n.2**	
System	$E_{vac}(eV)$	System	$E_{vac}(eV)$
CeO_2 (110)	+1.27	CeO_2 (111)	+1.84
CuO(101)	+1.69	CuO (-111)	+1.45
-	-	CuO (111)	+1.60
CeO_2/CuO, CeO_2 side	+1.47	CeO_2/CuO, CeO_2 side	+1.49
CeO_2/CuO, interface	+0.52	CeO_2/CuO, interface	+1.50
CeO_2/CuO, CuO side	+1.06	CeO_2/CuO, CuO side	-0.34

Moreover, the calculated energies of vacancy formation of Tab.4.4 once again confirmed the experimental NEXAFS observations: in fact, after the two oxides are merged, vacancies are formed more easily, indicating a different reactivity of the atoms in the composite with respect to the single oxide precursors, especially under reducing conditions. In detail, for interface n.1 the vacancy formation at the interface is more than twice lower than on the surfaces of the single oxides. In the case of interface n.2, we observe that the energy formation of O vacancies on the CeO_2/CuO interface is comparable with the ones of the single oxides, while the value is even negative on the CuO side close to the CeO_2/CuO interface. This results confirms that the reactive sites responsible of the methane activation on the composite surface are located in proximity of the CeO_2/CuO interface.

4.3.4 Proposed reaction mechanism model

A summary of the spectroscopic information obtained with the combined *operando* NEXAFS/*In situ* DRIFT experiment are shown in Fig.4.22.

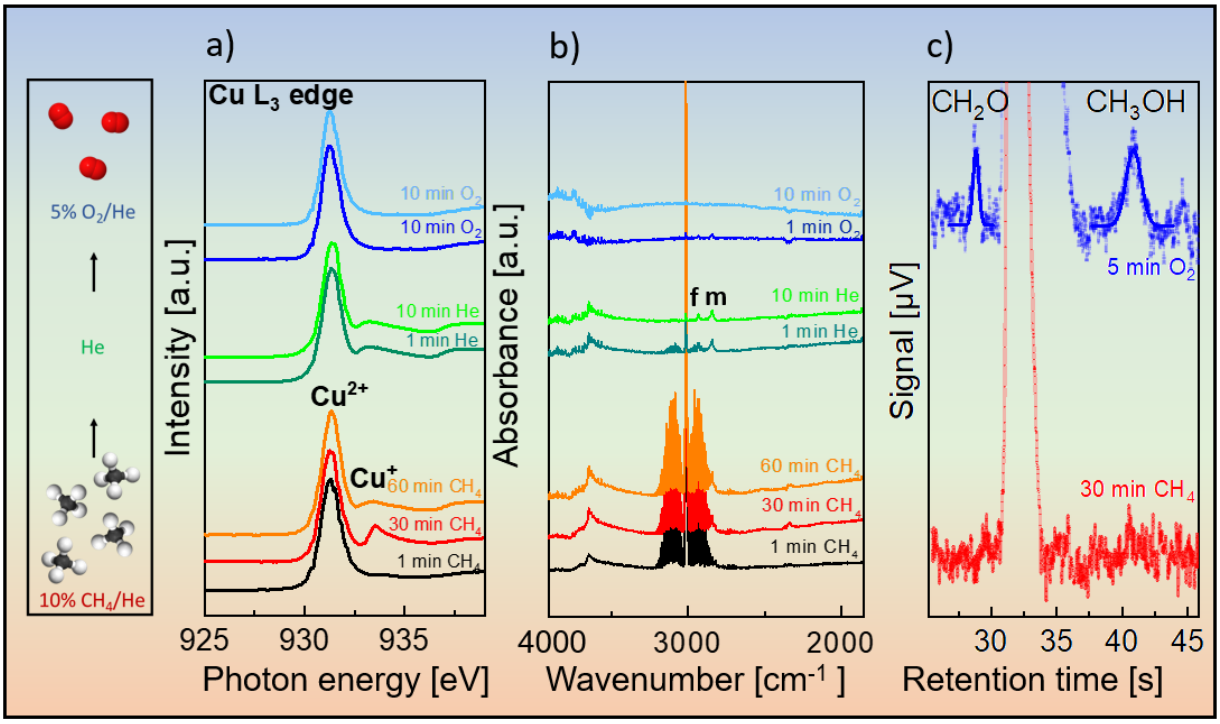

Figure 4.22: Summary of the combined *operando* NEXAFS/*In situ* DRIFT results. a) Cu $L_{2,3}$ NEXAFS, b) DRIFT, c) Micro-GC spectra evolution during the different reaction steps. Black and red-based lines: spectra acquired exposing the $MCeO_2/CuO$ catalyst to the $He(92\%)/CH_4(8\%)$ reaction mixture; green-based lines: spectra acquired exposing the catalyst to the $He(100\%)$ reaction mixture; Blue-based lines: spectra acquired exposing the catalyst to the $He(96\%)/O_2(4\%)$ reaction mixture. On the left, a graphical representation of the reaction steps, from the bottom to the top, is reported.

Looking at the figure, the main results can be summarized as follows:

- When CH_4 is added to the reaction mixture, it is activated on the catalyst surface. Experimentally, NEXAFS spectra show that part of Cu^{2+} sites are reduced to Cu^+; simultaneously, DRIFT spectra evidenced the formation of formates and methoxy species (structures labeled with f and m in the figure), together with surface hydroxyles (at 3650 cm^{-1}). We know from literature data that the position of the DRIFT peaks can be associated with a CeO_2 substrate, while the position of the hydroxyles is slightly shifted (of $\simeq -10cm^{-1}$).

- When CH_4 is removed from the reaction mixture, keeping a 100% Helium flow, Cu^+ sites, methoxy and formates related structures are still present in the spectra; this observation allowed to verify the direct correlation between Cu reduction and adsorbates formation.
- The introduction of O_2 in the reaction mixture takes to a $Cu^+ \rightarrow Cu^{2+}$ oxidation and a simultaneous disappearing of the methoxy, formates and hydroxyles DRIFT peaks. At the same time, CO_2, H_2O, CH_2O and CH_3OH are detected by the Micro-GC.
- The surface of the catalyst is totally restored after the introduction of O_2, and the catalytic cycle can be repeated more times without deactivating/poisoning the material surface.

The summarized results allowed us to predict an hypotetical mechanism model for the catalytic partial oxidation of methane to methanol (that can be extended also to the other detected reaction products), schematized in Fig.4.23. The first step of the mechanism shows the starting catalyst surface, where a peculiar CeO_2/CuO interface is formed upon the milling process. In proximity of the interface, on the CuO side, an high charge concentration is present coming from the CeO_2 side, as demonstrated through NEXAFS spectroscopy and validated by DFT calculations. In that region, reactive oxygen atoms are able to deprotonate a CH_4 molecule (step 2), forming a hydroxyle (detected by DRIFT and NEXAFS); the remaining methyl is adsorbed on an oxygen atom of the CeO_2 side forming a methoxy species, as observed in the DRIFT spectra. These species are strongly chemisorbed on the catalyst surface. The subsequent introduction of O_2 in the reaction mixture promotes the desorption of a CH_3OH (formed by the $-OH$ and the $-CH_3$ adsorbed species), leaving a vacancy that is refilled by an oxygen atom (steps 3 and 4).

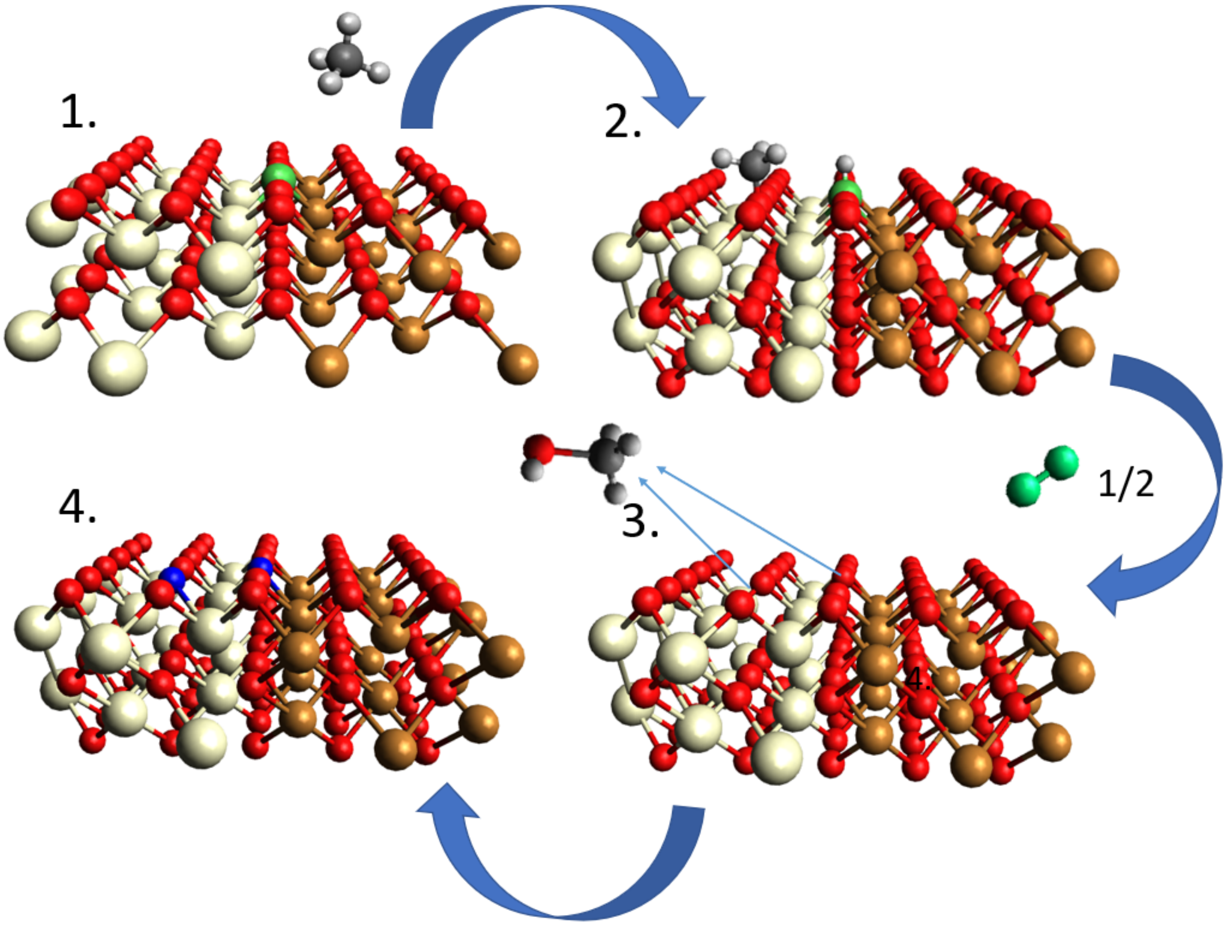

Figure 4.23: Scheme of the hypothesized reaction mechanism. Red balls: O; Light yellow balls: Ce; brown balls: Cu; dark grey balls: Carbon; white balls: Hydrogen; Green balls: reactive O; Blue Balls: O atoms refilling the vacancies formed during the methanol desorption. Note: the figures are not real models as the ones of Fig.4.20, but qualitative representations.

The reactions steps can be summarized as follows (the catalyst surfaces have been labelled with an *):

1. $CeO_2*/CuO*+CH_4$

2. $CeO_2*CH_3/CuO*H$

3. $CeO_2 * /CuO * V_O + CH_3OH(product) + 1/2O_2(reactant)$
4. $CeO_2 * /CuO*$

We observed also the production of CH_2O, CO_2 and H_2O with the micro-GC. Their production follows the same path of Fig.4.22, with the difference that CH_4 is deprotonated twice in the case of formaldehyde, and therefore also a molecule of water is desorbed, according to the following mechanism:

1. $CeO_2 * /CuO * +CH_4$
2. $CeO_2 * CH_2/CuO * H_2$
3. $CeO_2 * V_O/CuO * V_O + CH_2O(product) + H_2O(product) + O_2(reactant)$
4. $CeO_2 * /CuO*$ (O_2 refills the created vacancies)

In the case of CO_2, the CH_4 is deprotonated three times:

1. $CeO_2 * /CuO * +CH_4$
2. $CeO_2 * C/CuO * H_4$
3. $CeO_2 * V_O/CuO * 2V_O + CO_2(product) + 2H_2O(product) + 2O_2(reactant)$
4. $CeO_2 * /CuO*$ (3 of the 4 oxygen atoms introduced refill the created vacancies, while the fourth contributes to CO_2 production)

All the reported mechanisms are balanced according to the stoichiometric ratios of eq.4.3, 4.4 and 4.5.

4.3.5 Conclusions and perspectives

This study investigated the promising catalytic properties of a CeO_2/CuO composite synthetized exploiting a green and scalable ball milling process. As a comparison, we investigated a similar CeO_2/CuO composite synthesized with a conventional impregnation method. The standard *ex situ* characterization techniques employed to investigate the morphological and textural properties of catalysts (XRD, BET and SEM) were not sufficient to highlight noteworthy differences between the two composites, but helped to identify similar morphological and structural properties. The combined *operando* NEXAFS and *in situ* DRIFT investigation, on the opposite, revealed a drastically different catalytic behaviour for the two composites at real operating conditions. The impregnated catalyst does not interact with methane, and as a consequence it is not able to catalyze its partial oxidation. On the other hand, the ball milled composite is able to activate methane at low temperatures (250 °C). The cause of this outstanding behaviour was elucidated by NEXAFS spectrocopy, whose spectra evidenced a charge transfer occurring from Ce to Cu atoms upon the ball milling process, during which the mechanochemical energy provided to the system is able to create specific reactive interfaces on the final composite that are absent in the conventional impregnated catalyst. Fundamental for the synthetic approach was the use of an High Surface Area CeO_2 as a precursor: rich of surface oxygen vacancies, it is able to enhance the Ce → Cu charge transfer, as demonstrated also by DFT calculations. The *In situ* DRIFT investigation shown that methane is adsorbed on the catalyst surface on oxygen atoms, in the form of methane oxidation intermediates (mainly methoxy and formates). When the catalyst is exposed to an oxidizing agent, all the adsorbates are desorbed in the form of CO_2, H_2O, CH_2O and CH_3OH, detected by the micro-GC directly connected to the *operando* NEXAFS reaction cell. The product desorption promoted by O_2 restores the initial electronic configuration of the catalyst surface, therefore making it possible to perform more catalytic cycles without deactivating the catalyst. For this reason, it is important to underline the fundamental role of the *operando*/*in situ* techniques, without which all the observed catalyst modifications would not have been detected. The deep spectroscopic investigation at real catalytic conditions allowed to hypotize a mechanism model for the reaction, which involves reactive oxygen atoms close to the CeO_2/CuO interface, able to deprotonate the CH_4 that is consequently adsorbed on the CeO_2 side of the composite. The oxidizing agent (O_2) acts as a promoter for the products desorption, refilling the created oxygen vacancies and therefore restoring the initial catalyst surface. Due to the outstanding catalytic properties and the facile and green synthetic method, the ball milled CeO_2/CuO catalyst revealed to be a promising candidate to be exploited at the industrial level; nevertheless, the selectivity to methanol should be improved. Considered the fundamental information obtained in this study, we were able to put the basis for the future catalyst optimization, which reside in three main potential improvements:

- Increase the surface area of the starting CeO_2 precursor, in order to increase the number of initial Ce^{3+} surface sites;
- Tune the ratio between CeO_2 and CuO content in the final composite; this work reported the results obtained with a weighted CeO_2/CuO ratio of 20%/80%, but it can be changed in order to increase the number of active sites;
- Change the reaction conditions based on the proposed reaction mechanism, for example introducing H_2O which could act as a promoter shifting the reaction equilibrium towards the production of methanol.

4.4 Bibliography

[1] Zhijun Zuo, Pedro J. Ramírez, Sanjaya D. Senanayake, Ping Liu, and José A. Rodriguez. Low-temperature conversion of methane to methanol on CeO_x/Cu_2O catalysts: Water controlled activation of the C–H bond. *Journal of the American Chemical Society*, 138(42):13810–13813, 2016.

[2] Alessandro Trovarelli. *Catalysis by ceria and related materials*, volume 2. World Scientific, 2002.

[3] Ping Li, Xiaoyin Chen, Yongdan Li, and Johannes W Schwank. A review on oxygen storage capacity of CeO_2-based materials: Influence factors, measurement techniques, and applications in reactions related to catalytic automotive emissions control. *Catalysis Today*, 327:90–115, 2019.

[4] N Laosiripojana and S Assabumrungrat. Catalytic dry reforming of methane over high surface area ceria. *Applied Catalysis B: Environmental*, 60(1-2):107–116, 2005.

[5] Francesca Giordano, Alessandro Trovarelli, Carla de Leitenburg, and Massimiliano Giona. A model for the temperature-programmed reduction of low and high surface area ceria. *Journal of catalysis*, 193(2):273–282, 2000.

[6] Daniela Terribile, Alessandro Trovarelli, Carla de Leitenburg, Giuliano Dolcetti, and Jordi Llorca. Unusual oxygen storage/redox behavior of high-surface-area ceria prepared by a surfactant-assisted route. *Chemistry of materials*, 9(12):2676–2678, 1997.

[7] Matteo Cargnello, Vicky VT Doan-Nguyen, Thomas R Gordon, Rosa E Diaz, Eric A Stach, Raymond J Gorte, Paolo Fornasiero, and Christopher B Murray. Control of metal nanocrystal size reveals metal-support interface role for ceria catalysts. *Science*, 341(6147):771–773, 2013.

[8] Carl Walkey, Soumen Das, Sudipta Seal, Joseph Erlichman, Karin Heckman, Lina Ghibelli, Enrico Traversa, James F McGinnis, and William T Self. Catalytic properties and biomedical applications of cerium oxide nanoparticles. *Environmental Science: Nano*, 2(1):33–53, 2015.

[9] Zhouxin Luo, Guoqiang Zhao, Hongge Pan, and Wenping Sun. Strong Metal-Support Interaction in Heterogeneous Catalysts. *Advanced Energy Materials*, 12(37):2201395, 2022.

[10] SJ Tauster, SC Fung, RTK Baker, and JA Horsley. Strong interactions in supported-metal catalysts. *Science*, 211(4487):1121–1125, 1981.

[11] Lichen Liu and Avelino Corma. Identification of the active sites in supported subnanometric metal catalysts. *Nature Catalysis*, 4(6):453–456, 2021.

[12] Francesco Pinna. Supported metal catalysts preparation. *Catalysis Today*, 41(1-3):129–137, 1998.

[13] Jingyue Liu. Advanced electron microscopy of metal-support interactions in supported metal catalysts. *ChemCatChem*, 3(6):934–948, 2011.

[14] Jing Zhang and J Will Medlin. Catalyst design using an inverse strategy: From mechanistic studies on inverted model catalysts to applications of oxide-coated metal nanoparticles. *Surface Science Reports*, 73(4):117–152, 2018.

[15] Anna Ostroverkh, Viktor Johanek, Peter Kus, Romana Sediva, and Vladimír Matolín. Efficient ceria-platinum inverse catalyst for partial oxidation of methanol. *Langmuir*, 32(25):6297–6309, 2016.

[16] Michalis Konsolakis. The role of Copper–Ceria interactions in catalysis science: Recent theoretical and experimental advances. *Applied Catalysis B: Environmental*, 198:49–66, 2016.

[17] D. Gamarra, G. Munuera, A. B. Hungría, M. Fernández-García, J. C. Conesa, P. A. Midgley, X. Q. Wang, J. C. Hanson, J. A. Rodríguez, and A. Martínez-Arias. StructureActivity Relationship in Nanostructured CopperCeria-Based Preferential CO Oxidation Catalysts. *The Journal of Physical Chemistry C*, 111(29):11026–11038, 2007.

[18] Shu Hua Wang, Li Xu, Pan Shen, Chao Chen, and Ning Zhang. New approach to synthesis of CuO/CeO_2 catalysts for preferential CO oxidation. *Applied Mechanics and Materials*, 472:666 – 670, 2014. Cited by: 4.

[19] Daniel Gamarra, Carolina Belver, Marcos Fernández-García, and Arturo Martínez-Arias. Selective CO oxidation in excess H_2 over copper-ceria catalysts: Identification of active entities/species. *Journal of the American Chemical Society*, 129(40):12064 – 12065, 2007. Cited by: 287.

[20] Wei-Wei Wang, Pei-Pei Du, Shi-Hui Zou, Huan-Yu He, Rui-Xing Wang, Zhao Jin, Shuo Shi, Yu-Ying Huang, Rui Si, Qi-Sheng Song, Chun-Jiang Jia, and Chun-Hua Yan. Highly Dispersed Copper Oxide Clusters as Active Species in Copper-Ceria Catalyst for Preferential Oxidation of Carbon Monoxide. *ACS Catalysis*, 5(4):2088–2099, 2015.

[21] A Hornés, AB Hungría, P Bera, A López Cámara, M Fernández-García, A Martínez-Arias, L Barrio, M Estrella, G Zhou, JJ Fonseca, et al. Inverse CeO_2/CuO catalyst as an alternative to classical direct configurations for preferential oxidation of CO in Hydrogen-rich stream. *Journal of the American Chemical Society*, 132(1):34–35, 2010.

[22] Kumudu Mudiyanselage, Sanjaya D Senanayake, Leticia Feria, Shankhamala Kundu, Ashleigh E Baber, Jesús Graciani, Alba B Vidal, Stefano Agnoli, Jaime Evans, Rui Chang, et al. Importance of the metal-oxide interface in catalysis: In situ studies of the water-gas shift reaction by ambient-pressure X-

Ray Photoelectron Spectroscopy. *Angewandte Chemie International Edition*, 52(19):5101–5105, 2013.

[23] José A Rodriguez, Jesús Graciani, Jaime Evans, Joon B Park, Fan Yang, Dario Stacchiola, Sanjaya D Senanayake, Shuguo Ma, Manuel Pérez, Ping Liu, et al. Water-Gas Shift Reaction on a Highly Active Inverse CeO_x/Cu (111) Catalyst: Unique Role of Ceria Nanoparticles. *Angewandte chemie international edition*, 48(43):8047–8050, 2009.

[24] SY Yao, WQ Xu, AC Johnston-Peck, FZ Zhao, ZY Liu, S Luo, SD Senanayake, A Martínez-Arias, WJ Liu, and JA Rodriguez. Morphological effects of the nanostructured ceria support on the activity and stability of CuO/CeO_2 catalysts for the water-gas shift reaction. *Physical Chemistry Chemical Physics*, 16(32):17183–17195, 2014.

[25] José A Rodriguez, Ping Liu, Dario J Stacchiola, Sanjaya D Senanayake, Michael G White, and Jingguang G Chen. Hydrogenation of CO_2 to methanol: importance of metal-oxide and metal-carbide interfaces in the activation of CO_2. *Acs Catalysis*, 5(11):6696–6706, 2015.

[26] Wen-Jie Shen, Yuichi Ichihashi, and Yasuyuki Matsumura. Low temperature methanol synthesis from carbon monoxide and hydrogen over ceria supported copper catalyst. *Applied Catalysis A: General*, 282(1-2):221–226, 2005.

[27] Shanlong Li, Nengli Wang, Yonghai Yue, Guangsheng Wang, Zhao Zu, and Yu Zhang. Copper doped ceria porous nanostructures towards a highly efficient bifunctional catalyst for carbon monoxide and nitric oxide elimination. *Chemical science*, 6(4):2495–2500, 2015.

[28] Andrzej Adamski, Wojciech Zając, Filip Zasada, and Zbigniew Sojka. Copper ionic pairs as possible active sites in N_2O decomposition on CuO_x/CeO_2 catalysts. *Catalysis Today*, 191(1):129–133, 2012.

[29] Alessandro Trovarelli, Francesca Zamar, Jordi Llorca, Carla De Leitenburg, Giuliano Dolcetti, and Janos T Kiss. Nanophase fluorite-structured $CeO_2 - ZrO_2$ Catalysts prepared by high-energy mechanical milling. *Journal of Catalysis*, 169(2):490–502, 1997.

[30] TP Yadav, NK Mukhopadhyay, RS Tiwari, and ON Srivastava. Studies on the formation and stability of nano-crystalline $Al_{50}Cu_{28}Fe_{22}$ alloy synthesized through high-energy ball milling. *Materials Science and Engineering: A*, 393(1-2):366–373, 2005.

[31] Erika Furlani, Eleonora Aneggi, Carla de Leitenburg, and Stefano Maschio. High energy ball milling of titania and titania-ceria powder mixtures. *Powder technology*, 254:591–596, 2014.

[32] Vladimir Šepelák, Andre Düvel, Martin Wilkening, Klaus-Dieter Becker, and Paul Heitjans. Mechanochemical reactions and syntheses of oxides. *Chemical Society Reviews*, 42(18):7507–7520, 2013.

[33] Friederike C Jentoft, Helmut Schmelz, and Helmut Knözinger. Preparation of selective catalytic reduction catalysts via milling and thermal spreading. *Applied Catalysis A: General*, 161(1-2):167–182, 1997.

[34] Dong Wook Kwon, Kwang Hee Park, and Sung Chang Hong. The influence on SCR activity of the atomic structure of V_2O_5/TiO_2 catalysts prepared by a mechanochemical method. *Applied Catalysis A: General*, 451:227–235, 2013.

[35] Lu-Cun Wang, Yong-Mei Liu, Miao Chen, Yong Cao, He-Yong He, Gui-Sheng Wu, Wei-Lin Dai, and Kang-Nian Fan. Production of hydrogen by steam reforming of methanol over Cu/ZnO catalysts prepared via a practical soft reactive grinding route based on dry oxalate-precursor synthesis. *Journal of Catalysis*, 246(1):193–204, 2007.

[36] L Guczi, L Takács, G Stefler, Zs Koppány, and L Borko. $Re-Co/Al_2O_3$ bimetallic catalysts prepared by mechanical treatment: CO hydrogenation and CH_4 conversion. *Catalysis today*, 77(3):237–243, 2002.

[37] Maila Danielis, Sara Colussi, Carla de Leitenburg, Lluís Soler, Jordi Llorca, and Alessandro Trovarelli. The effect of milling parameters on the mechanochemical synthesis of $Pd-CeO_2$ methane oxidation catalysts. *Catalysis Science & Technology*, 9(16):4232–4238, 2019.

[38] M. Grioni, J. B. Goedkoop, R. Schoorl, F. M. F. de Groot, J. C. Fuggle, F. Schäfers, E. E. Koch, G. Rossi, J.-M. Esteva, and R. C. Karnatak. Studies of copper valence states with Cu L_3 X-Ray-Absorption Spectroscopy. *Phys. Rev. B*, 39:1541–1545, Jan 1989.

[39] Francesco Tavani, Martina Fracchia, Alessandro Tofoni, Luca Braglia, Andrea Jouve, Sara Morandi, Maela Manzoli, Piero Torelli, Paolo Ghigna, and Paola D'Angelo. Structural and mechanistic insights into low-temperature CO oxidation over a prototypical high entropy oxide by Cu L-edge operando soft X-ray absorption spectroscopy. *Physical Chemistry Chemical Physics*, 23(46):26575–26584, 2021.

[40] M Grioni, JF Van Acker, MT Czyžyk, and JC Fuggle. Unoccupied electronic structure and core-hole effects in the X-Ray-Absorption spectra of Cu_2O. *Physical Review B*, 45(7):3309, 1992.

[41] Luca Braglia, Francesco Tavani, Silvia Mauri, Raju Edla, Damjan Krizmancic, Alessandro Tofoni, Valentina Colombo, Paola D'Angelo, and Piero Torelli. Catching the Reversible Formation and Reactivity of Surface Defective Sites in Metal–Organic Frameworks: An Operando Ambient Pressure-NEXAFS Investigation. *The Journal of Physical Chemistry Letters*, 12(37):9182–9187, 2021.

[42] L.A.J. Garvie and P.R. Buseck. Determination of Ce^{4+}/Ce^{3+} in electron-beam-damaged CeO_2 by electron energy-loss spectroscopy. *Journal of Physics and Chemistry of Solids*, 60(12):1943–1947, 1999.

[43] R. C. Karnatak, J. M. Esteva, H. Dexpert, M. Gasgnier, P. E. Caro, and L. Albert. X-ray absorption studies of $\mathrm{CeO_2}$, $\mathrm{PrO_2}$, and $\mathrm{TbO_2}$. I. Manifestation of localized and extended f states in the 3d absorption spectra. *Phys. Rev. B*, 36:1745–1749, Jul 1987.

[44] B. T. Thole, G. van der Laan, J. C. Fuggle, G. A. Sawatzky, R. C. Karnatak, and J.-M. Esteva. 3d X-Ray-Absorption lines and the $3d^94f^{n+1}$ multiplets of the lanthanides. *Phys. Rev. B*, 32:5107–5118, Oct 1985.

[45] M Barreau, D Chen, J Zhang, V Papaefthimiou, C Petit, D Salusso, E Borfecchia, S Turczyniak-Surdacka, K Sobczak, S Mauri, et al. Synthesis of Ni-doped ceria nanoparticles and their unusual surface reduction in hydrogen. *Materials Today Chemistry*, 26:101011, 2022.

[46] Zongxian Yang, Gaixia Luo, Zhansheng Lu, and Kersti Hermansson. Oxygen vacancy formation energy in Pd-doped ceria: A DFT+U study. *The Journal of Chemical Physics*, 127(7):074704, 2007.

[47] Magdalena Chrzan, Damian Chlebda, Przemysław Jodłowski, E Salomon, Andrzej Kołodziej, Anna Gancarczyk, Maciej Sitarz, and J Łojewska. Towards methane combustion mechanism on metal oxides supported catalysts: ceria supported palladium catalysts. *Topics in Catalysis*, 62(1):403–412, 2019.

[48] Can Li, Kazunari Domen, Ken-ichi Maruya, and Takaharu Onishi. Spectroscopic identification of adsorbed species derived from adsorption and decomposition of formic acid, methanol, and formaldehyde on cerium oxide. *Journal of Catalysis*, 125(2):445–455, 1990.

[49] Pablo German Lustemberg, Marta Verónica Bosco, A Bonivardi, Heriberto Fabio Busnengo, and MV Ganduglia-Pirovano. Insights into the nature of formate species in the decomposition and reaction of methanol over cerium oxide surfaces: a combined infrared spectroscopy and density functional theory study. *The Journal of Physical Chemistry C*, 119(37):21452–21464, 2015.

[50] Can Li, Yoshihisa Sakata, Toru Arai, Kazunari Domen, Ken-ichi Maruya, and Takaharu Onishi. Adsorption of carbon monoxide and carbon dioxide on cerium oxide studied by Fourier-transform infrared spectroscopy. Part 2 - Formation of formate species on partially reduced CeO_2 at room temperature. *Journal of the Chemical Society, Faraday Transactions 1: Physical Chemistry in Condensed Phases*, 85(6):1451–1461, 1989.

[51] Kohei Yoshikawa, Hiroki Sato, Masato Kaneeda, and Junko Nomura Kondo. Synthesis and analysis of CO_2 adsorbents based on cerium oxide. *Journal of CO2 Utilization*, 8:34–38, 2014.

[52] Claude Binet, Marco Daturi, and Jean-Claude Lavalley. IR study of polycrystalline ceria properties in oxidised and reduced states. *Catalysis Today*, 50(2):207–225, 1999.

[53] Ahmed Badri, Claude Binet, and Jean-Claude Lavalley. An FTIR study of surface ceria hydroxy groups during a redox process with H_2. *Journal of the Chemical Society, Faraday Transactions*, 92(23):4669–4673, 1996.

[54] AJ Knoll, S Zhang, M Lai, P Luan, and GS Oehrlein. Infrared studies of gas phase and surface processes of the enhancement of catalytic methane decomposition by low temperature plasma. *Journal of Physics D: Applied Physics*, 52(22):225201, 2019.

[55] Ned Thaddeus Taylor, Francis Huw Davies, Isiah Edward Mikel Rudkin, Conor Jason Price, Tsz Hin Chan, and Steven Paul Hepplestone. ARTEMIS:

Ab initio restructuring tool enabling the modelling of interface structures. *Computer Physics Communications*, 257:107515, 2020.

[56] Paolo Giannozzi, Stefano Baroni, Nicola Bonini, Matteo Calandra, Roberto Car, Carlo Cavazzoni, Davide Ceresoli, Guido L Chiarotti, Matteo Cococcioni, Ismaila Dabo, et al. QUANTUM ESPRESSO: a modular and open-source software project for quantum simulations of materials. *Journal of physics: Condensed matter*, 21(39):395502, 2009.

Chapter 5

Hydrogen Production Mechanism in Low-Temperature Methanol Decomposition Catalyzed by Ni_3Sn_4 Intermetallic Compound: A Combined Operando and Density Functional Theory Investigation

The data presented in this chapter have been the object of a publication in Journal of Physical Chemistry Letters.

Partially reprinted with permission from https://doi.org/10.1021/acs.jpclett.2c03471.

5.1 Introduction

Intermetallic compounds (IMCs)[1–8], already introduced in Chapter 2, are solid materials having the unique characteristic to possess ordered crystal structures which differ from the ones of the constituting elements. This results in peculiar electronic structures, making IMCs different from the substitutional alloys, in which all atoms occupy randomly the crystal structure sites of one of the constituting elements. As an example, Fig.5.1 reports the density of states of a metal (Pd), a substitutional alloy (AgPd) and an intermetallic compound (GaPd): it is evident that, while the density of states of AgPd is similar to the one of the metal with a difference in the filling degree, for GaPd the electronic structure is extremely modified.

The consequence of the consistently different electronic structure result in different chemical and catalytic properties, making intermetallic catalysts promising materials, whose potentialities have still to be deeply elucidated. Compared to substitutional alloys, IMCs possess three main advantages[1]:

- Peculiar electronic and crystal structures, resulting in different catalytic properties;
- Improved stability, which prevents segregation phenomena or decomposition in reactive atmospheres;
- The constituting transition metals have a wide range of chemical potential, which can be used to adjust the catalyst redox properties according to the different catalytic reaction to be performed.

As extensively discussed in Chapter 2, the possibility to deeply investigate the above mentioned advantages was not trivial until the advent of the *operando* techniques, able to monitor the structural, geometric and electronic modifications occurring at the catalyst operating conditions. The engineering of intermetallic

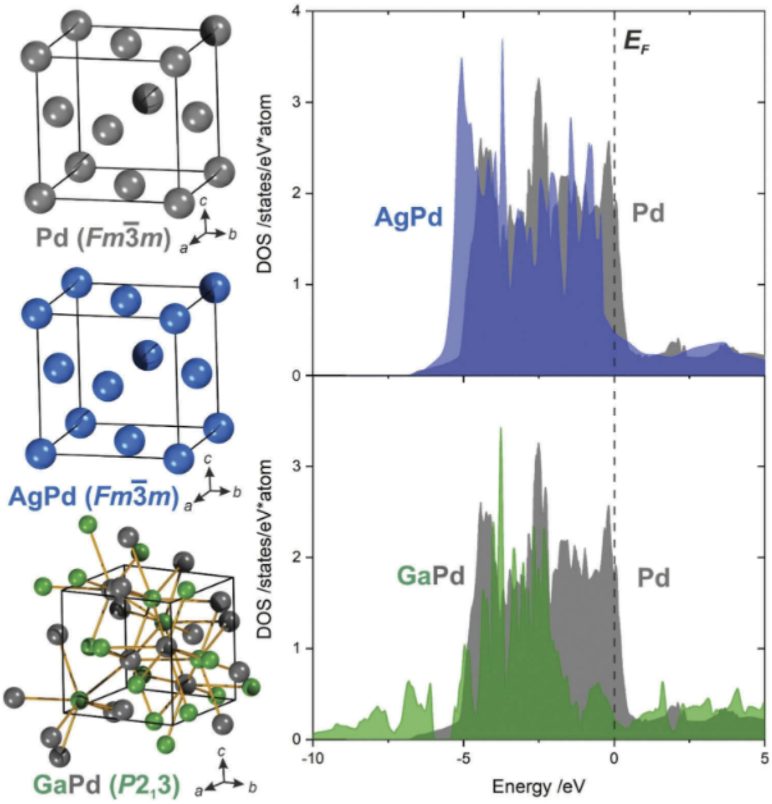

Figure 5.1: Crystal structures (left) and respective electronic structure (right) of metallic Pd, AgPd substitutional alloy and GaPd intermetallic compound[9,10].

catalysts, depending on the use that the final material must have, and which property you want to exploit in catalytic conditions, can be done starting from three different designs, graphically shown in Fig.5.2.

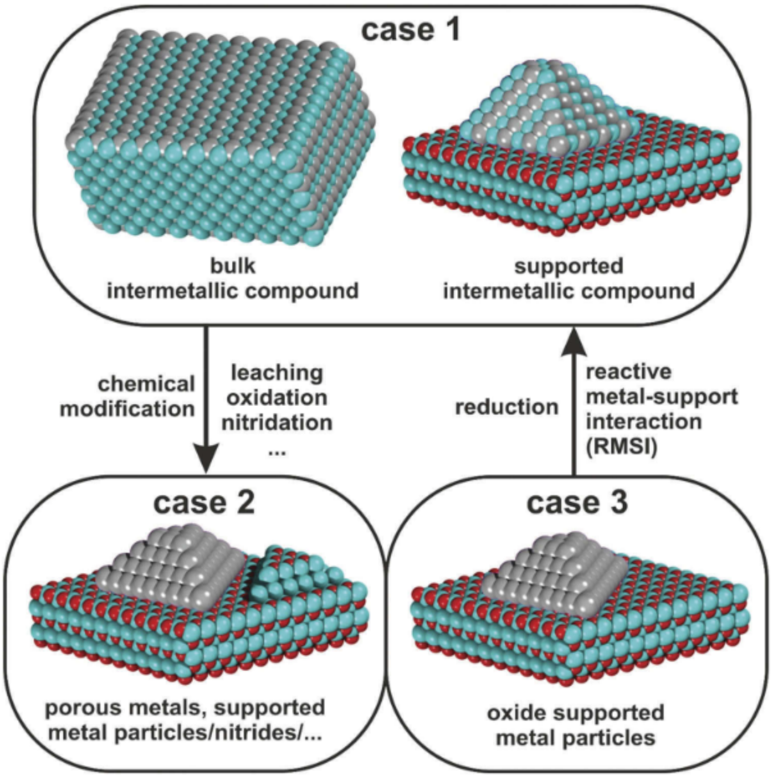

Figure 5.2: Graphic representation of three different way to disegn an intermetallic catalyst. This image has been directly taken from the review of Professor Armbrüster[9].

In case 1, the IMC can be exploited as a bulk compound (image on the left) or as supported particles (image on the right). In the latter case, other variables can further contribute to tune the catalytic properties of the final material, for example the support-metal interactions or properties derived from the material nano-sizing, such as reactive under coordinated surface sites, or different absorption properties. In the second case of Fig.5.2, IMCs can be used as precursors and decomposed to the active species by (partial) oxidation or leaching[11]. In the third case, under specific conditions supported metal particles can evolve, through reactive metal-support diffusion, to intermetallic particles[12]. In this work, we decided to investigate the electronic structure modifications under catalytic conditions for intermetallic Ni-Sn taken as bulk compounds, as in the left panel of the first case of Fig.5.2. In this way, we could address and investigate the catalytic activity intrinsic of the compound, without adding other variables coming from the support. Nevertheless, we found through *operando* investigations that specific catalyst pretreatments deeply affect the surface electronic structure of the material, therefore modifying also their catalytic activity.

As already introduced in section 2.3.2.1, the main advantage of using Ni as a catalyst is the low cost and natural abundance compared to the expensive noble metals. On the other hand, Ni catalysts have the main disadvantages of fast deactivation[13–17] and not optimized product selectivity, that can be tuned by synthesizing Ni alloys or supported Ni particles[18–22]. Intermetallic catalysts based on Ni and Sn have been investigated in heterogeneous catalysis during the last years mainly for hydrogenation and steam reforming reactions[23–28]. Only few studies regarding Ni-Sn intermetallic compounds for syngas production from catalytic direct methanol decomposition are reported in literature[9,29,30]. All the cited studies show that Sn incorporation can improve the catalyst selectivity to hydrogen, suppressing the secondary undesired products (all the details regarding the catalytic reaction are provided in section 2.3.2). Nevertheless, at our knowledge no study focuses on the mechanism through which Sn incorporation manages to direct the catalysis reaction towards a specific product through *operando* investigations. Moreover, the reported studies investigate the catalytic performances at temperatures > 300°C.

In this study, we investigated the methanol decomposition mechanism of Ni-Sn IMCs at temperatures between 250 and 300 °C. Such a hitherto unexplored temperature range, while extremely advantageous for industrial methanol decomposition implementation, would also enable the recovery of waste heat in methanol-fueled vehicles. In this work, we unveiled the physicochemical mechanism ruling low-temperature methanol decomposition by combining *operando* ambient pressure NEXAFS with synchrotron-based *in situ* X-ray photoemission spectroscopy (XPS), complemented by density functional theory (DFT) calculations. Evidently, the use of *operando* and *in situ* spectroscopic techniques using synchrotron radiation is particularly appropriate to monitor the status of the catalyst surface during the reaction[31,32] while standard XPS investigations[9,29,30] can only probe the irreversible surface modifications after the catalytic reaction, thus inevitably losing information on the various reaction steps. This analysis allowed to show that the surface oxide skin (with the thickness of 1.5 nm) imaged by high-resolution transmission electron microscopy (HR-TEM) emerging from the natural interaction of the catalyst surface with the ambient atmosphere plays a pivotal role in the catalytic mechanism. We also established that different amounts of Sn in the alloy strongly influence methanol decomposition selectivity, and we find that, for Ni_3Sn_4, the H_2/CO_2 ratio is increased, compared to Ni_3Sn_2. The role of surface oxide phases was also demonstrated through the analysis of pretreatment procedures of the $Ni-Sn$ catalysts. Spectroscopic results were correlated with a semiquantitative analysis of the gas products, detected through online micro gas chromatography.

5.2 Results and Discussion

5.2.1 Surface reactivity of Ni_3Sn_4

5.2.1.1 Theoretical modeling of Ni_xSn_y surface reactivity

The atomic structure and energetics of various configurations of Ni_xSn_y surfaces and chemical reactivity of these substrates were studied by DFT, using QUANTUM ESPRESSO code[33] (version 6.0) and the GGA PBE approximation[34] with van der Waals (vdW) corrections[35]. To unveil the key features of the surface chemical reactivity of Ni - Sn alloys, we modeled the physisorption of molecular oxygen, water, carbon monoxide, and methanol in gaseous phases on the most stable Ni_3Sn_4 and Ni_3Sn_2 surfaces, whose models are shown in panels a-c) of Fig.5.3.

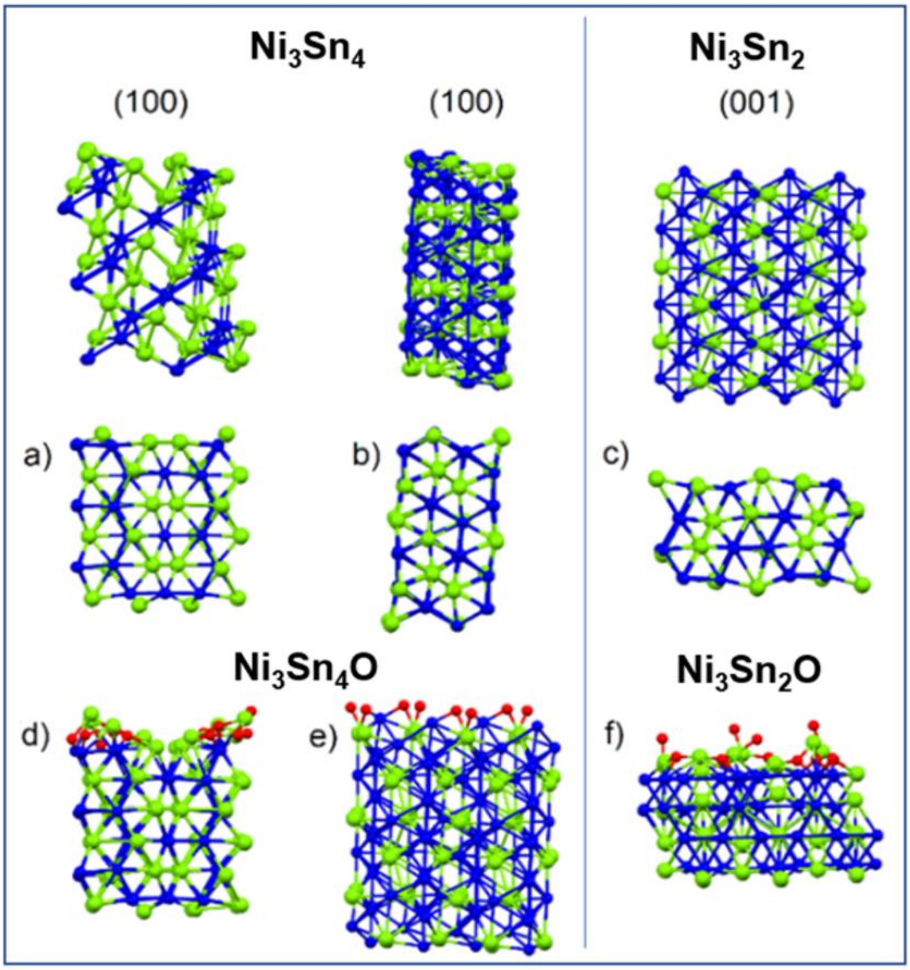

Figure 5.3: (a-c) top and side views of optimized atomic structures corresponding with reduced and side views (d-f) of oxidized (100) surface of Ni_3Sn_4, (100) and (001) surfaces of Ni_3Sn_2. Green, blue, and red balls denote Sn, Ni, and O, respectively.

The calculations reported in Tab.5.1 demonstrate the stable adsorption of all considered species with the magnitude of the differential Gibbs free energies larger than 20 kJ/mol for all of the investigated Ni_xSn_y compounds.

Successively, we modeled the decomposition of physisorbed molecular water, oxygen, and methanol. The decomposition of molecular oxygen and methanol is

Table 5.1: Calculated Differential Enthalpies (ΔH) of Physisorption and Decomposition, and Differential Gibbs Free Energy (ΔG) of Physisorption of Considered Compounds from Gaseous Phases on Various Reduced and Oxidized Surfaces of Ni_xSn_y Compounds.

Substrate	**Surface**	**Adsorbant**	$\mathbf{\Delta H_{ads}}$**(kJ/mol)**	$\mathbf{\Delta G}$	$\mathbf{\Delta H_{dec}}$**(kJ/mol)**
$\mathbf{Ni_3Sn_4}$	(100)	CO	-65.53	-46.18	-
		H_2O	-74.78	-43.48	+18.59
		O_2	-138.40	-126.91	-96.70 (-542.17)*
		CH_3OH	-104.48	-66.88	-156.50
$\mathbf{Ni_3Sn_2}$	(100)	CO	-43.17	-23.82	-
		H_2O	-52.85	-21.55	+13.15
		O_2	-31.18	-19.69	-353.52 (-282.75)
		CH_3OH	-74.03	-36.43	-193.02
$\mathbf{Ni_3Sn_2}$	(001)	CO	-70.18	-50.83	-
		H_2O	-81.48	-50.18	+7.37
		O_2	-73.35	-61.86	-88.16 (-351.33)
		CH_3OH	-109.36	-71.76	-369.61
$\mathbf{Ni_3Sn_4O_x}$	(100)	CO	+63.97	+83.32	-
		H_2O	+44.00	+75.30	-65.83
		CH_3OH	-60.91	-23.31	-202.09
$\mathbf{Ni_3Sn_2O_x}$	(100)	CO	-236.28	-216.93	-
		H_2O	-247.92	-216.62	-37.65
		CH_3OH	-265.45	-227.85	-550.19
$\mathbf{Ni_3Sn_2O_x}$	(001)	CO	-205.61	-186.26	-
		H_2O	+24.78	-56.02	-249.26
		CH_3OH	-88.04	-50.44	-636.01

*Values in parentheses correspond to the oxidation of entire surfaces of Ni_xSn_y (see panels d-f of Fig.5.3).

an exothermic process with the magnitude of enthalpies above 80 kJ/mol for all considered surfaces (see the last column of Tab.5.1). Decomposition of water on non-oxidized surfaces is an endothermic process with a rather low energy cost of the reaction (i.e., < 20 kJ/mol). Hence, pristine surfaces of Ni_xSn_y compounds are chemically unstable under ambient conditions. In oxygen-rich environments (including air), Ni_xSn_y surfaces are prone to oxidation (see panels d-f) in Fig.5.3), as indicated by enthalpies below 280 kJ/mol for all considered surfaces.

5.2.1.2 Chemical reactivity of Ni_3Sn_4: *In situ* XPS and HRTEM investigation

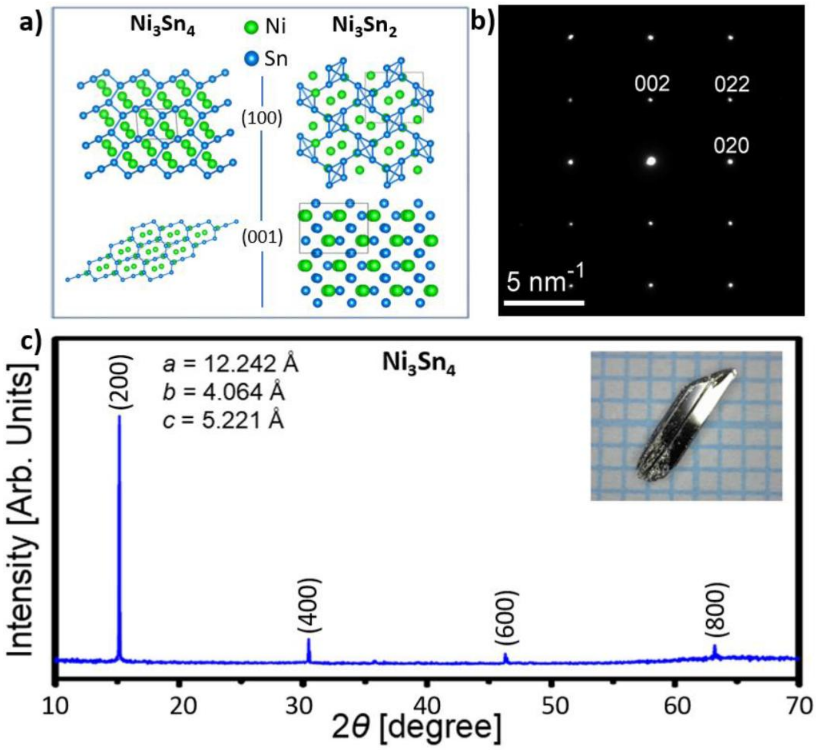

Figure 5.4: a) Atomic structure of Ni_3Sn_4 and Ni_3Sn_2 along the (100) and (001) planes; b) SAED pattern of the analyzed grain oriented along the [100] zone axis. The lattice fringes corresponding to the (002) and (020) families of planes spaced at 0.25 and 0.20 nm, respectively, are indicated on the HR-TEM micrograph in panel c) of Fig.5.6. c) XRD pattern of a Ni_3Sn_4 single crystal. A photograph of grown crystals is shown in the inset.

Ni_3Sn_4 (see panel a) of Fig. 5.4) belongs to the C2/m [No. 12] (monoclinic unit cell) space group. The single crystals were grown through the flux method described in the experimental section 5.4.1, and their atomic structure was validated by X-ray diffraction (XRD) (see panel c) of Fig. 5.4), High-resolution transmission electron microscopy (see panel c) of Fig.5.6), and small-area electron diffraction (SAED, see panel b) of Fig. 5.4). All structural experiments confirm the expected Ni_3Sn_4 structure (ICSD No. 105363), with lattice parameters a = 12.236 Å, b = 4.063 Å, 110 and c = 5.224 Å. For reasons that will be elucidated later in the discussion, panel a) of Fig. 5.4 also shows the crystal structure of Ni_3Sn_2 belonging to the Pnma [No. 62] (orthorhombic unit cell) space group.

The easy surface oxidation found in the theoretical results presented in the previous section was validated by experiments on surface chemical reactivity of Ni_3Sn_4 by *in situ* XPS, performed with Synchrotron radiation to *i)* have an improved energy resolution, to follow core-level shifts, and *(ii)* enhance surface sensitivity, to identify eventual modifications of the surface composition in an oxidative environment. The XPS survey of the as-cleaved Ni_3Sn_4 is shown in Fig.5.5 (panel a)), together with the O1s core level spectrum of the catalyst after after having exposed the Ni_3Sn_4 surface to $1 \cdot 10^4$ mbar of O_2 for $\simeq$ 22 min (corresponding to a dose of $10^5 L$, $1L = 10^6 Torr \cdot s$) and to air (for 5 min and 30 min). The absence of the O 1s signal in photoemission spectra of the as-cleaved Ni_3Sn_4 proves the quality of our grown crystals and the absence of contaminants on the surface.

Fig.5.6 shows the Ni 3p and Sn 3d core levels at the same experimental conditions of the spectra of Fig.5.5 (panel b) and after a prolonged air exposure of $\simeq$ 1 year. The fitting of the Ni 3p core level spectra of the as-cleaved Ni_3Sn_4 indicates the presence of two structures located at 66.5 and 68.0 eV, attributed to the Ni $3p_{1/2}$ and $3p_{3/2}$ components of metallic Ni (Ni^0)[36,37]. A consideration about the stoichiometric composition of the sample can be made, looking at the different intensities of the Ni 3p and Sn 3d core levels in the as-cleaved material, which are relatively close in energy. The areas of these peaks have been divided

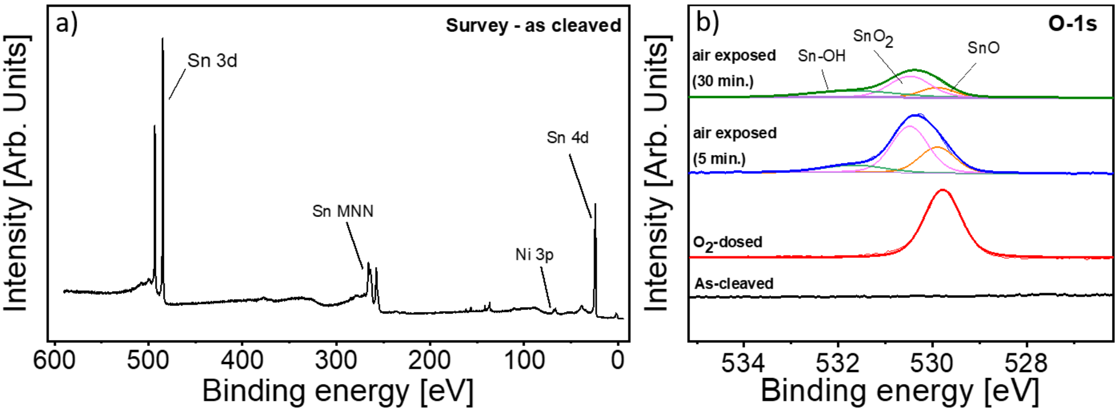

Figure 5.5: a) Survey spectrum of the as-cleaved Ni_3Sn_4. The photon energy is 690 eV; b) O 1s core levels for as-cleaved Ni_3Sn_4 and after exposure to O_2 (20 minutes, $1x10^{-4}$ mbar), and air for 5 and 30 min.

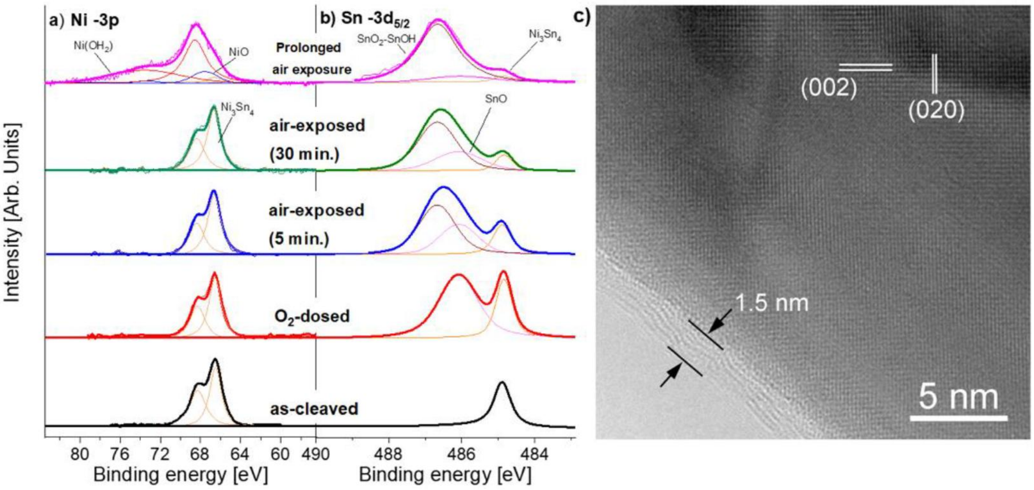

Figure 5.6: a) Ni 3*p* and b) Sn 3*d* core levels for as-cleaved Ni_3Sn_4 and after exposure to $10^5 L$ L of O_2 and air (for 5 min, 30 min, and 1 year). The photon energy is 690 eV, and the spectra were normalized to the maximum. c) HR-TEM micrograph of a Ni_3Sn_4 grain in B = [100] orientation, close to the grain border. An amorphous oxide skin with an average thickness of ≃1.5 nm is indicated by the two arrows.

for the cross sections (0.22 for the Sn 3d and 0.18 for the Ni 3p, considering a photon energy of 690 eV[38,39]) in order to calculate the relative concentration of the two elements, finding out that the Sn/Ni ratio is equal to 2.9 ± 0.1. Given the surface sensitivity of the XPS technique (which at 690 eV of photon energy should be about few atomic layers), this means that the analyzed sample surface stoichiometry is very different from the Sn/Ni ratio of 1.33 of the bulk, suggesting that the surface of the cleaved Ni_3Sn_4 is Sn-rich.

No changes in the Ni 3p spectra were detected after the different sample treatments (Fig.5.6 panel a)). Even after exposing the sample to air for 30 min, the spectroscopic features related to Ni^0 maintain the same shape and energy position. It is important to note that pure Ni surfaces partially oxidize, even in the presence of lower O_2 pressures[40,41]. Correspondingly, important modifications were detected in the Sn 3d core-level spectra (panel b) of Fig.5.6). Specifically, a new component in Sn 3$d_{5/2}$, attributed to SnO[42,43] appeared at 486.1 eV in the O_2-dosed surface (with a spectral weight of 70% of the total area). After 5 min of storage in air, another component ascribed to $SnO_2/SnOH$ species[44,45] emerged in Sn 3d core-level spectra at 486.6 eV (54% of the total spectral area), while the intensity of components related to SnO and Sn^0 decreased (spectral weights of 17% and 29%, respectively). The formation of oxides and hydroxides is also evident from the inspection of the O 1s (panel b) of Fig.5.5) core level. The pronounced formation of tin oxide in O-rich environments is consistent with the Sn-rich termination of Ni_3Sn_4. Moreover, one should also consider that selective Ni oxidation usually occurs in bimetallic surfaces often also with Ni segregation toward the surface[46–48]. After 30 min of air exposure, the intensity of $SnO_2/SnOH$ spectral component further increased, reaching 66% of the spectral weight. The component related to NiO only appeared in core-level spectra for prolonged storage in air extended up to $\simeq$ 1 year, although the main component of the Ni 3p spectrum was related to surface nickel-hydroxide (NiOH) species (81% of the total spectral weight)[49–51]. The formation of the oxide skin is confirmed by HR-TEM analysis (panel c) of

Fig.5.6), indicating the existence of an oxide layer with a thickness of $\simeq$ 1.5 nm. During the HR-TEM measurement we have also collected an EELS spectrum in the diffraction mode (Fig.5.7), on the thin border area of the grain shown in Fig.5.6.

The spectrum shows the signatures of the Sn $M_{4,5}$ and Ni $L_{2,3}$ edges at 485 eV and 855 eV, respectively. It is expected that the layer observed by HR-TEM is actually a native oxidation layer. Consequently, the oxygen EELS signal should be also present within the explored range, along with Sn and Ni. However, the oxygen K-edge at 532 eV (pointed by an arrow in Fig.5.7) overlaps the delayed maximum of the Sn $M_{4,5}$ edge, which makes not possible a reliable interpretation regarding the oxygen presence. Since XPS is one of the most surface sensitive spectroscopic techniques, having a probing depth of few atomic layers, especially at electron kinetic energies between 100 and 1000 eV[52], it is reasonable to think that the first atomic layers of the oxide skin evidenced by HR-TEM are SnO_x rich, while the underlying layers present a mixed composition of the two oxides.

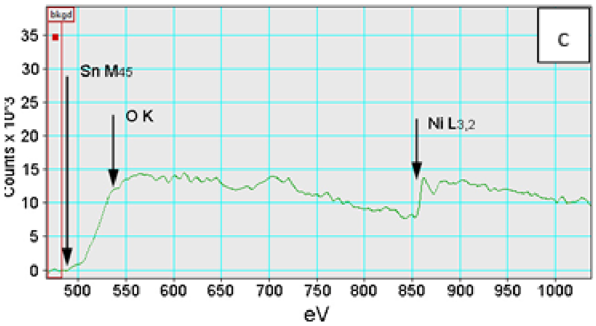

Figure 5.7: EELS spectrum acquired on the 1.5 nm surface layer observed with HRTEM.

5.2.2 Catalytic methanol decomposition monitored with *operando* NEXAFS

5.2.2.1 Experimental procedure

Once samples were loaded in the reaction cell described in section 3.2.1.3, the reactor was filled with He. The gases were injected inside the cell through the three flowmeters calibrated to a maximum total flow of 50 mL/min. In order to inject the methanol, a glass bubbler was added to the gas line, using He as an inert carrier gas. Both catalysts investigated in this study (Ni_3Sn_4 and Ni_3Sn_2) were subjected to two different kinds of experiments, with different initial pre-treatments. The first one consisted in the heating from room temperature to 250°C in inert atmosphere (100% of Helium). Then, the sample was exposed to a $He(90\%)/O_2(10\%)$ mixture for 30 minutes. After that, the oxygen was removed from the reaction mixture, until a steady state was reached. Successively, the connection to the bubbler was opened, allowing the methanol vapors to enter the reaction cell for approximately 30 minutes. Then, the methanol was removed, keeping the samples in He until a steady state was reached. The same procedure was repeated heating the samples from 250 to 300 °C. The second experiment was like the one just described, except for a pre-treatment in a $He(80\%)/H_2(20\%)$ flow mixture. For sake of clarity, a graphical summary of the experimental procedure is reported in Fig.5.8.

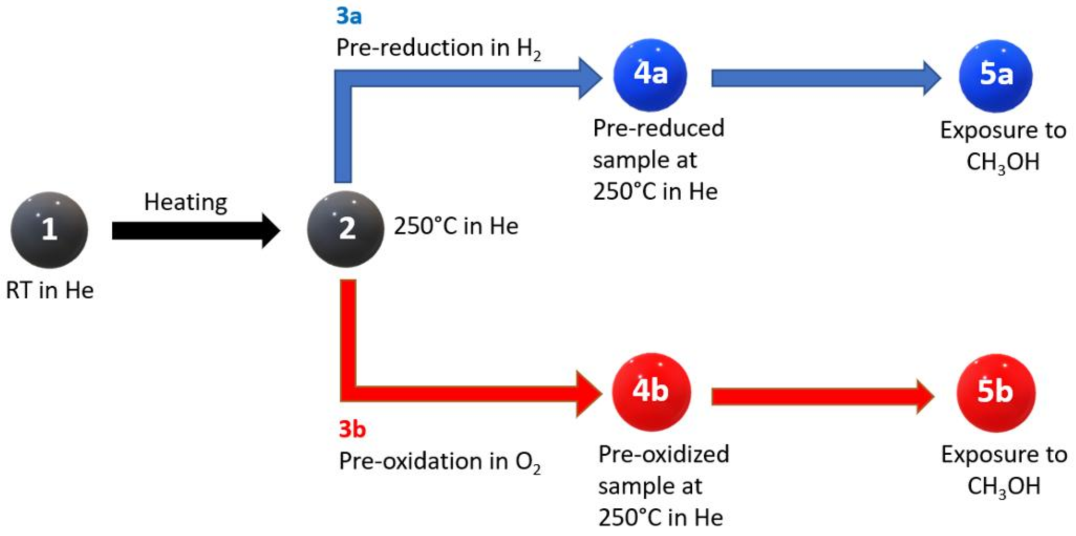

Figure 5.8: Scheme reporting the experimental procedure followed during the *operando* NEXAFS experiments. The same scheme from point 1 to 5 has been repeated reaching a temperature of 300°C, for both Ni_3Sn_4 and Ni_3Sn_2.

5.2.2.2 NEXAFS spectra analysis

By means of *operando* NEXAFS spectra, the methanol decomposition reaction at working conditions has been monitored. The experiment was conducted for the Ni_3Sn_4 and Ni_3Sn_2 catalysts following the experimental procedure reported in Fig.5.8. Specifically, during all the experimental steps we monitored the Ni L_2 and L_3 absorption edges at 871 and 853 eV, associated with dipole-allowed $2p_{1/2} \rightarrow 3d$ and $2p_{3/2} \rightarrow 3d$ electronic transitions[53]. In fact, they are particularly sensitive to local chemical modifications occurring in the immediate surroundings of the absorbing atoms, as d orbitals in Ni are involved in covalent bonds[54]. For both pristine Ni_3Sn_4 and Ni_3Sn_2, $L_{2,3}$ absorption edges spectra are shown in Fig.5.9.

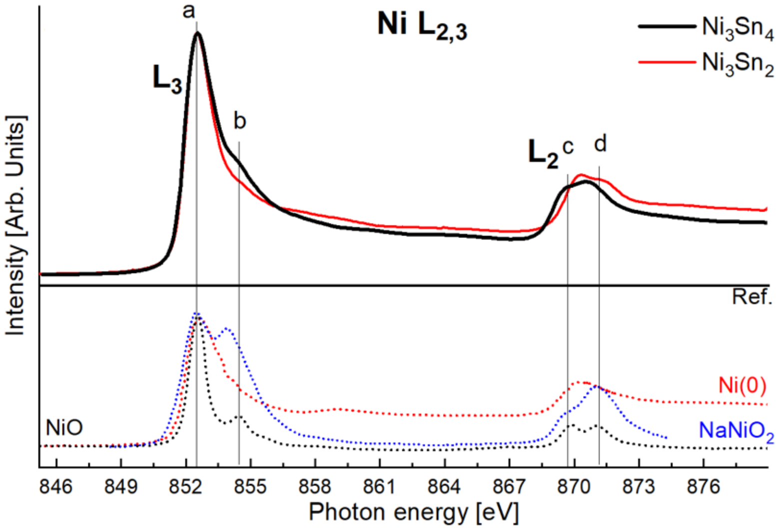

Figure 5.9: NEXAFS spectra of the Ni $L_{2,3}$ edges acquired at RT in He at 1 bar, for Ni_3Sn_4 (black) and Ni_3Sn_2 (red) samples. Bottom panel: reference spectra of Ni^0,Ni^{2+} and Ni^{3+} acquired at the APE-HE beamline.

Comparing the spectra with the references reported in the bottom panel of the figure, we can observe that structure b in the L_3 edge, characteristic of oxidized Nickel, is almost absent in both catalysts, while the broadened shape of the intense white line located at $\simeq$ 852 eV resembles the one of metallic Ni. Therefore, we can confirm also with NEXAFS spectroscopy that in $Ni-Sn$ compounds Ni atoms are preserved from oxidation when exposed to oxidizing atmospheres. Indeed, after being cleaved both samples were exposed to air during the sample mounting in the reaction cell. To evaluate the influence of surface modifications, we performed pre-oxidation and pre-reduction treatments for both samples. The results are shown in Fig.5.10 only for Ni_3Sn_4, since Ni_3Sn_2 behaves in the same way.

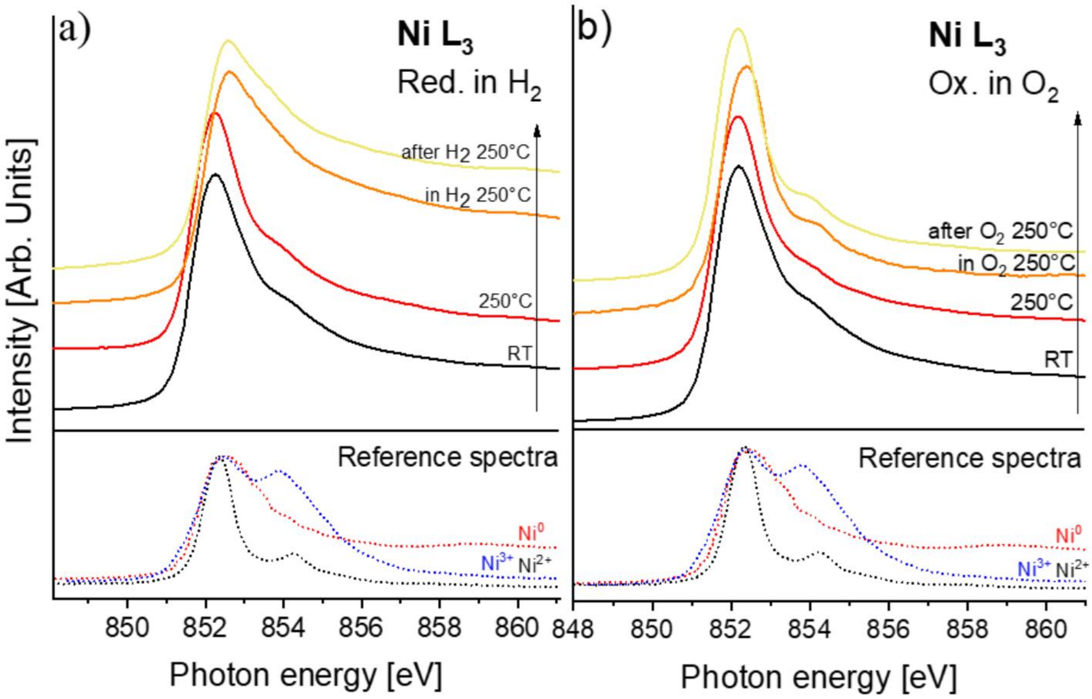

Figure 5.10: Operando NEXAFS spectral evolution of the Ni $L_{2,3}$ edges of Ni_3Sn_4 during a) pre-reduction and b) pre-oxidation treatments. Bottom panels show reference spectra of Ni^0, Ni^{2+} (NiO), and Ni^{3+} $(NaNiO_2)$.

Whenever the sample was heated from room temperature to 250 and 300 °C in He flow, no spectral modifications were detected in either of the cases (red curves in Fig.5.10 for the selected case of 250 °C). Successively, for the pre-reduction case (panel a) in Fig.5.10), a 80:20 He/H_2 gas mixture was introduced into the reaction cell for $\simeq$ 30 min with the sample kept at 250 °C. The corresponding NEXAFS spectrum (labeled in orange) showed an evident peak broadening, with an overall shift by $+0.4$ eV, due to a joint effect of *i*) the reduction of part of the surface Ni centers sites and *ii*) the charge transfer between Sn and Ni atoms, associated with the reduction of tin oxide phases.

Once removed from the H_2 flux, the NEXAFS spectrum still exhibited all spectral modifications occurring in the H_2 environment (panel a) in Fig.5.10), thus indicating the irreversibility of the reduction process. In the case of the pre-oxidation process (panel b) in Fig.5.10), an 90:10 He/O_2 gas mixture was introduced in the reaction cell. A partial (and irreversible) Ni oxidation was observed, as indicated by the increased intensity of the feature $\simeq$ 854 eV, ascribed to NiO. The slight energy shift by +0.2 eV is related to the charge transfer between surface NiO phases and the underlying Ni_3Sn_4 crystal.

After the above-mentioned pretreatments, both samples were exposed to CH_3OH for 30 min in the reaction cell. The CH_3OH decomposition reaction was followed by monitoring the Ni L_3 edges with a simultaneous detection of gaseous reaction products through micro gas chromatography. The results are shown in Fig.5.11.

When exposing Ni_3Sn_4 to CH_3OH at 250 °C, regardless of the surface pretreatment, the Ni L_3 edge spectral shape remained unchanged during and after the reaction (panel a) of Fig.5.11). Thus, for the pre-oxidized sample, Ni maintained a prevailing +2 oxidation state, while, for the pre-reduced sample, Ni kept its metallic character. However, a rigid spectral shift to higher photon energies by +0.2 eV was found, thus suggesting that CH_3OH weakly perturbs the local chemical environment of Ni atoms. Such a reversible energy shift could arise from a charge transfer associated with the methanol-tin oxide interaction. Correspondingly, H_2 was detected with the online micro gas chromatography, proving the effective decomposition of methanol to syngas. Upon CH_3OH interaction at 300 °C, the Ni L_3 edge was unchanged in the pre-oxidized sample, while NiO was formed in the case of the pre-reduced sample. Correspondingly, side-reaction gas products, such as H_2O or CO_2, were detected by the micro-gas chromatography. To evaluate the optimal Sn content in the $Ni-Sn$ alloy, we repeated the *operando* NEXAFS ex-

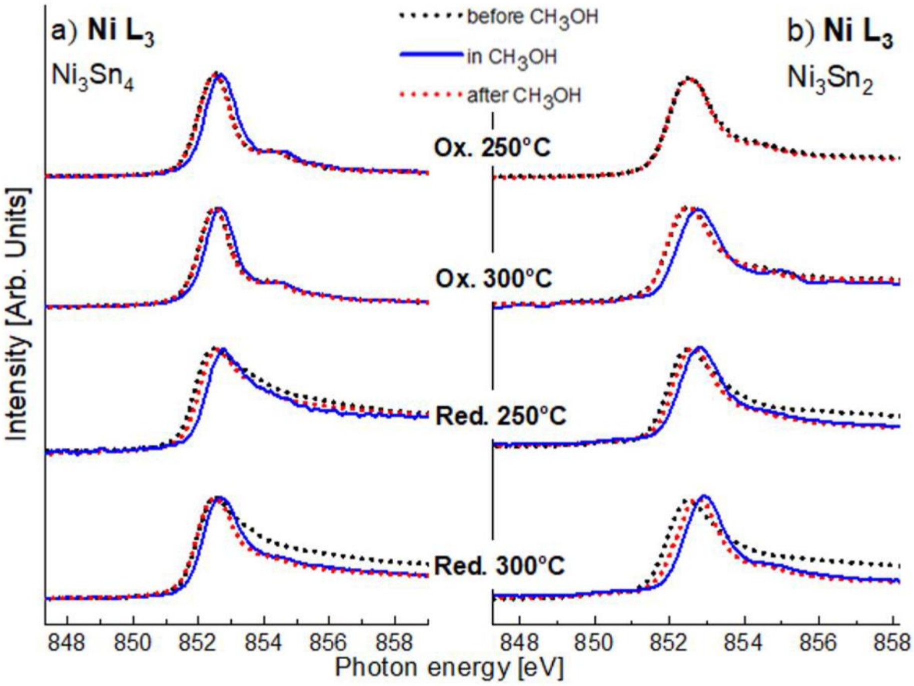

Figure 5.11: Operando NEXAFS spectra of the Ni L_3 edge acquired for a) Ni_3Sn_4 and b) Ni_3Sn_2 at various experimental conditions, during the sample exposition to CH_3OH. Black dotted, red dotted, and blue spectra denote spectra acquired before introducing the CH_3OH in the NEXAFS reaction cell, after having removed CH_3OH from the reaction cell, and during the exposition to CH_3OH, respectively.

periments for the case of Ni_3Sn_2 (panel b) of Fig.5.11), although acquired spectra indicated an easier catalyst deactivation. In fact, already at 250 °C we can detect an irreversible Ni oxidation upon methanol exposure for the pre-reduced spectrum (spectra shown in the third row in the figure). Morover, the rigid energy shift observed in the Ni_3Sn_4 is not totally reversible in the case of Ni_3Sn_2, especially for the pre-reduced sample.

5.2.2.3 Micro Gas Chromatography analysis

Panels b) and c) of Fig.5.12 report the typical signals detected by gas chromatography during the methanol decomposition reaction, which should be regarded as a qualitative identification of gaseous products.

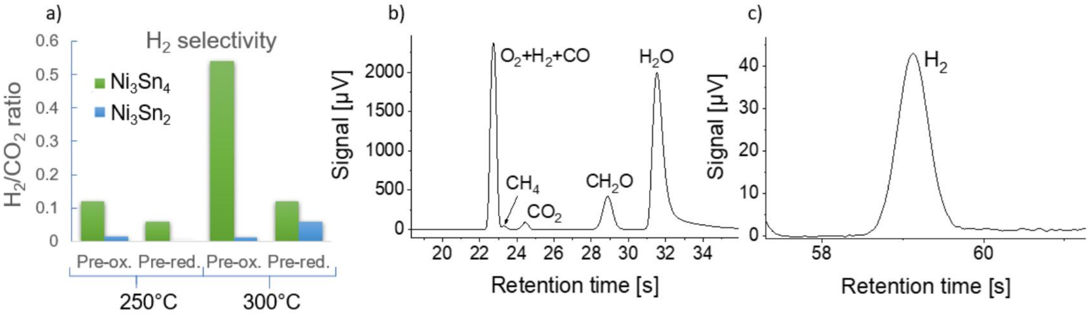

Figure 5.12: Online micro gas chromatography results obtained by detecting the gas products of the CH_3OH decomposition catalyzed by Ni_3Sn_4 and Ni_3Sn_2, after the sample pre-oxidation and pre-reduction, at 250 and 300 °C. The bar intensity represents the ratio between the areas of the H_2 and CO_2 peaks detected at different experimental conditions for the two samples. These values can be adopted as semi quantitative indicators for H_2 selectivity. b) and c) Representative micro chromatograms obtained in the presence of CH_3OH, using two different columns, with He and N_2 as gas carriers, respectively.

All the experimental conditions used gave rise to the same signals for both Ni_xSn_y samples, with observable modifications only in the peaks intensities (therefore we show only two illustrative chromatograms in the figure). Looking at the figure, the main gas products detected during the sample exposure to methanol are

CO_2, H_2O, CH_4 (that are by-products coming from side reactions, i.e. Boudouard, methanation and reverse water-gas shift reactions), CH_2O (coming from a partial decomposition of methanol) and H_2. CO signal was not recorded because is overlapped with the ones of O_2 and H_2. To overcome this issue, we were able to measure the isolated H_2 signal using another chromatographic column: the related chromatograph is reported in panel c) of Fig.5.12. It is important to underline that the chromatograms analysis can be only semi-quantitative, for two reasons: *i*) the system has not been calibrated with standard references, thus it is not possible to assign a defined gas volume to a specific peak area; *ii*) The design of the operando NEXAFS reaction cell is made in such a way that the gas flows pass through the sample surface tangentially. Nevertheless, it is possible to compare the different reaction conditions, sample pre-treatments and Sn content in terms of H_2 selectivity, considering the ratio between H_2 (the desired reaction product) and CO_2 (a secondary product) peaks areas. The results of this analysis are reported in the graph shown in panel a) of Fig.5.12. The direct comparison of gas chromatography results indicates that *i*) for all the tested experimental conditions and *ii*) throughout the entire investigated temperature range, Ni_3Sn_4 provided superior H_2 selectivity, with respect to Ni_3Sn_2. Thus, one can conclude that the higher Sn content has a beneficial effect on the suppression of the secondary reactions in the CH_3OH decomposition reaction path. Moreover, increasing the temperature from 250 °C to 300 °C improves the selectivity to H_2 by a factor of 4.5 and 2.0 for the pre-oxidized and pre-reduced $Ni_3Sn_{4,}$ respectively. On the other hand, such conclusions are not valid for the case of Ni_3Sn_2, thus indicating that low-temperature methanol decomposition is unfeasible for lower Sn contents in the Ni-Sn alloy. For the sake of completeness, we mention that in other studies[55] methanol decomposition for Ni_3Sn_2 was detected for a temperature quite higher (i.e., 325 °C). Unquestionably, the sample pretreatments deeply affect the H_2 selectivity. For the case-study example of Ni_3Sn_4, the oxidation pretreatment in O_2 improves the H_2 selectivity upon methanol exposure. Correspondingly, the quantification of direct CH_3OH conversion to H_2 provides results similar to those obtained for the H_2 selectivity (see Tab.5.2 and Fig.5.13), further supporting that the higher Sn content in Ni_3Sn_4, compared to Ni_3Sn_2, is capable of lowering the energy activation barrier for the methanol decomposition to H_2.

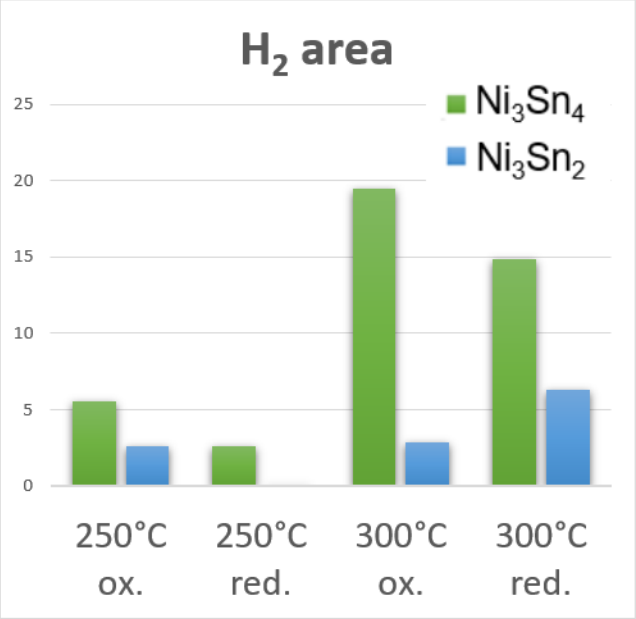

Figure 5.13: Online Micro-GC results obtained detecting the gas products of the CH_3OH decomposition catalyzed by Ni_3Sn_4 and Ni_3Sn_2, after the samples pre-oxidation and pre-reduction, at 250°C and 300°C. The bars intensity represents the areas of the H_2 peaks detected at the same experimental conditions for the two samples; these values can be used qualitatively as an index of the CH_3OH conversion to H_2.

Based on XPS (Figure 5.6) and DFT results, one can conclude that surface Sn sites are responsible for the different reaction paths of the CH_3OH on the sample surface. Explicitly, the surface tin-oxide skin could prevent the catalyst deactivation, avoiding the interaction between Ni atoms and the byproducts coming from secondary reactions.

Table 5.2: Summary of the online Micro-GC results obtained detecting the gas products of the CH_3OH decomposition catalyzed by Ni_3Sn_4 and Ni_3Sn_2, after the sample pre-oxidation and pre-reduction, at 250°C and 300°C. The values reported in the first two columns are the peak areas of the H_2 and CO_2 signals detected by the GC. The third column shows the ratio between the H_2/CO_2 areas, which is an index of the selectivity towards H_2 production.

	Ni_3Sn_4			**Ni_3Sn_2**		
Exp. condition	H_2 area	CO_2 area	H_2/CO_2	H_2 area	CO_2 area	H_2/CO_2
Pre-ox. 250 °C	5.58	45.9	0.12	2.62	169	0.015
Pre-ox. 300 °C	19.5	35.8	0.54	2.83	228	0.012
Pre-red. 250 °C	2.65	43.8	0.06	-	-	-
Pre-red. 300 °C	14.9	121	0.12	6.33	105	0.06

5.2.2.4 DFT Modeling of Methanol Decomposition and discussion

To further clarify the experimental results, theoretical DFT modeling of the methanol decomposition on the different catalysts surface has been performed. The reaction can be considered as a multistep process (eq.5.1 and 5.2):

$$CH_3OH \rightarrow * - OCH_3 + * - H \tag{5.1}$$

$$* - OCH_x \rightarrow * - OCH_{x-1} + * - H \tag{5.2}$$

where the asterisk symbol (*) represents the substrate. The final step of this reaction is related to the desorption of CO from the substrate. Hydrogen, adsorbed on the substrate during reactions 5.1 and 5.2, participate in the Tafel step of hydrogen evolution reaction in acidic media:

$$2 * H \rightarrow H_2 \tag{5.3}$$

Since methanol conversion occurs in liquid media, water decomposition similar to hydrogen evolution reaction in alkali media (see Tab.5.3) should be also considered. The results shown in Tab.5.3 demonstrate that the oxidation of the surfaces makes the processes described by reactions 5.1 and 5.2 more energetically favorable. The formation of hydrogen by Tafel reaction is an endothermic process for all non-oxidized surfaces, while it is an exothermic process for the oxidized (100) surface of Ni_3Sn_4 and the (001) surface of Ni_3Sn_2. Note that the Tafel step over the oxidized Ni_3Sn_4 surface is almost two times more favorable than over the oxidized (001) surface of Ni_3Sn_2 (0.94 eV vs 0.49 eV). All of these results are in qualitative agreement with experimental results (Fig.5.12). Thus, the increase of the H_2 selectivity over oxidized surfaces of Ni_xSn_y compounds can be caused by a combination of *i*) more favorable methanol decomposition and *ii*) hydrogen production by the Tafel reaction. Water decomposition ($H_2O \rightarrow *OH + *H$) can simultaneously occur with methanol conversion. This process is endothermic with an energy cost of <0.2 eV/mol for Ni_xSn_y surfaces and exothermic for oxidized Ni_xSn_yO surfaces (see Tab.5.3). Further desorption of hydroxyl groups from the surfaces requires an energy barrier exceeding 2 eV/mol. Thus, concurrent to methanol conversion, water decomposition will lead to the additional production of hydrogen, but also to robust passivation of active sites by hydroxyl groups, as indicated by the SnOH component in Sn $3d_{5/2}$ core-level spectra in Fig.5.6. Note that the energy of desorption of hydroxyl groups from the (100) surface of Ni_3Sn_4 is significantly lower than from the (001) surface of Ni_3Sn_2 (3.5 eV vs 4.4 eV). Therefore, the increase of the catalytic performance of oxidized Ni_3Sn_4 upon increasing the temperature from 250 °C to 300 °C (see Fig.5.12) can be explained by the increase in the number of active sites by the efficient removal of hydroxyl groups, forming chemical bonds with Sn atoms, by their recombination, with the successive desorption of water molecules. This hypothesis was experimentally validated through *operando* NEXAFS experiments in the O K edge region, as shown in panels a) and b) of Fig.5.14. Moreover, the figure shows the higher efficiency in water production of Ni_3Sn_4 compared to Ni_3Sn_2, also validated by gas chromatography (panel c) of Fig.5.14).

Table 5.3: Energies of the Steps of the Methanol Conversion and Hydrogen Evolution Reactions in Alkali and Acidic Media over Reduced and Oxidized Surfaces of Ni_xSn_y Compounds.

			Energy Cost (eV/mol)	
Reaction	**Substrate**	**Reaction products**	**Reduced substrate**	**Oxidized substrate**
Methanol Decomposition	**Ni_3Sn_4(010)**	substrate + CH_3OH	-1.08	-0.63
		$*OCH_3 + * - H$	-1.62	-2.09
		$*OCH_2 + * - H$	+0.98	+0.22
		$*OCH + * - H$	+1.15	-1.02
		$*OC + * - H$	+1.77	-2.04
		CO desorption	+0.68	-0.66
		H_2	+0.29	-0.94
	Ni_3Sn_2(010)	substrate + CH_3OH	-0.77	-2.75
		$*OCH_3 + * - H$	-2.00	-4.55
		$*OCH_2 + * - H$	-1.54	-1.79
		$*OCH + * - H$	-2.20	-2.40
		$*OC + * - H$	-1.88	-1.96
		CO desorption	+0.45	+2.45
		H_2	+0.17	+2.26
	Ni_3Sn_2(001)	substrate + CH_3OH	-1.13	-0.91
		$*OCH_3 + * - H$	-3.83	-6.59
		$*OCH_2 + * - H$	-3.74	-1.39
		$*OCH + * - H$	-2.66	-1.02
		$*OC + * - H$	-2.87	-1.45
		CO desorption	+0.73	+2.13
		H_2	+0.50	-0.49
HER in Alkali Media	**Ni_3Sn_4(010)**	substrate + H_2O	-0.77	+0.46
		$* - OH + * - H$	+0.19	-0.68
		OH desorption	+2.50	+3.50
		H_2	+0.29	-0.94
	Ni_3Sn_2(010)	substrate + H_2O	-0.55	-2.57
		$* - OH + * - H$	+0.13	-0.39
		OH desorption	+2.57	+3.13
		H_2	+0.17	+2.26
	Ni_3Sn_2(001)	substrate + H_2O	-0.84	+0.26
		$* - OH + * - H$	+0.07	-2.58
		OH desorption	+2.60	+4.43
		H_2	+0.50	-0.49
HER in Acidic Media	**Ni_3Sn_4(010)**	*-H	-0.29	+0.94
	Ni_3Sn_2(010)	*-H	-0.17	-2.16
	Ni_3Sn_2(001)	*-H	-0.50	+0.49

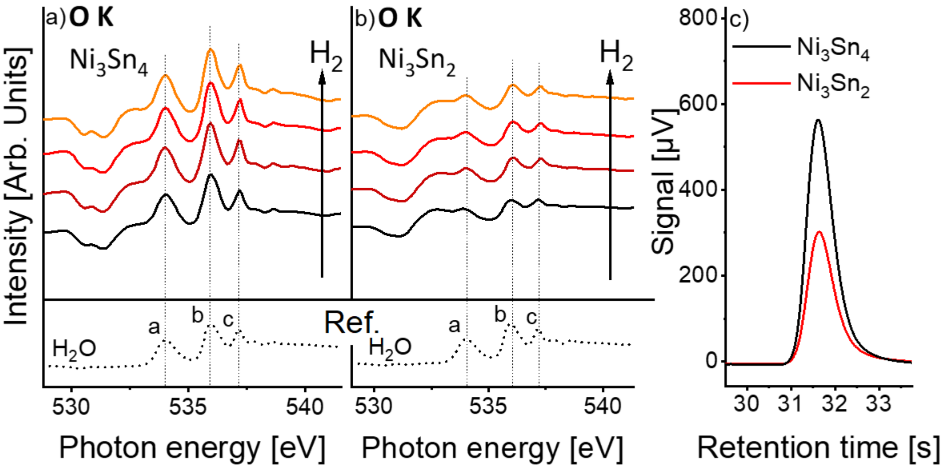

Figure 5.14: a-b) Top panels: *Operando* NEXAFS spectral evolution of the O K edges of a) Ni_3Sn_4 and b) Ni_3Sn_2 during the sample pre-treatment in a $He(90\%)/H_2(10\%)$ flow mixture for ≃ 30 min, at 250°C. Bottom panels: reference spectra of H_2O in gas phase, acquired at the APE-HE beamline. c) Chromatographic H_2O signal acquired for Ni_3Sn_4 and Ni_3Sn_2 during the $He(90\%)/H_2(10\%)$ pre-treatment.

Inspection of Tab.5.1 also suggests that both the differential Gibbs free energy (ΔG) and enthalpy (ΔH_{ads}) for CO and H_2O physisorption have positive values for oxidized Ni_3Sn_4, whereas, for oxidized Ni_3Sn_2, they are negative. This finding implies that increasing the Sn content makes the CO and H_2O physisorption (and, consequently, their decomposition) more difficult, which is consistent with the experimental data. Indeed, the micro gas chromatography results in Fig.5.12 show an improved selectivity to H_2 for oxidized Ni_3Sn_4. Since the *operando* NEXAFS results of Fig.5.11 show that Ni atoms in Ni_3Sn_4 are less subjected to irreversible electronic modifications, one can combine the information, concluding that the thicker tin-oxide skin formed at the Ni_3Sn_4 surface in an oxidative environment (including air) can protect subsurface Ni atoms from the interaction with molecules coming from secondary reactions, thus improving the selectivity to the methanol decomposition, which is responsible for the formation of syngas.

5.3 Conclusions and perspectives

This study shows the potentialities of combining synchrotron based *in situ* XPS, *operando* NEXAFS, and DFT calculations, in order to unveil the physicochemical mechanisms ruling low temperature (250 °C) CH_3OH decomposition in Ni_3Sn_4. The role of Sn content in Ni-Sn alloy was also assessed, through comparative experiments with Ni_3Sn_2. Definitely, in Ni_3Sn_4, secondary reactions in CH_3OH decomposition at low temperatures have a tendency to be suppressed, because of the higher Sn content in the compound. We clarified the role of surface tin-oxide phases naturally formed in oxidative environments (including air). Our results indicate that the tin-oxide skin protects the subsurface Ni atoms from their irreversible deactivation, thus improving catalyst durability. Moreover, it favors CH_3OH decomposition through subsequent deprotonations compared to the pristine $Ni - Sn$ alloys. Concurrently, H_2 and CO desorption is favored, enabling a more efficient CH_3OH conversion. Apart from this decomposition path, the adsorbed H atoms in oxidized Ni_3Sn_4 can produce H_2 through recombination, following the Tafel step of hydrogen evolution reaction in acidic media, which represents another source of hydrogen production. Our findings about the catalytic mechanism represent a fundamental basis for the future design and engineering of new low-cost $Ni - Sn$ catalysts for hydrogen production via direct methanol decomposition at low temperatures, with the perspective of exploiting them for scalable applications, in the optics of the imminent energy transition. A possible way to optimize the design of this intermetallic catalyst could be the synthesis of supported nanoparticles, in this way exploiting the metal-support interactions, as shown in the right panel of Fig.5.2. To this purpose, an oxide support with high O^{2-} mobility would be beneficial, as capable of supplying oxygen atoms to the surface tin oxide skin (such as CeO_2). Another possible way to exploit the role of the surface tin oxide skin could be the synthesis of core-shell nanoparticles, in which a Ni-based core is protected by the tin oxide layer. Fundamental for the next studies will be the addition of quantitative measurements of the catalytic performances (methanol conversion and selectivity to syngas) of the optimized catalysts.

5.4 Experimental

5.4.1 Single Crystal Growth

The crystal growth was performed in collaboration with the group of Prof. Antonio Politano (Università degli studi dell'Aquila). Single crystals of Ni_3Sn_4 were produced via the solution-growth method. Nickel powder (99.95%) and Sn ingots (99.99%) were mixed in a Ni:Sn atomic ratio of 1:20 and sealed in evacuated silica tubes. The sealed tube was heated to 750 °C at a rate of 100 °C/h, held at this temperature for 20 h, and then slowly cooled to 550 °C at a rate of 1 °C/h. Excess Sn flux was separated from the crystals using a centrifuge and diluted HCl. The obtained single crystals had a rodlike shape along the b-axis, with typical dimensions of 1.5 mm × 2 mm × 5 mm. The crystals were characterized by powder XRD on a Bruker D2 Phaser X-ray 414 diffractometer with Cu K radiation. The crystal orientation and crystal quality were confirmed by a Laue X-ray diffraction method.

5.4.2 *In Situ* XPS characterization

Synchrotron-based *In Situ* XPS experiments were performed at the Advanced Photoelectric Effect - High Energy (APE-HE) beamline at Elettra Synchrotron using a Scienta R3000 hemispherical electron energy analyzer in normal emission configuration (described in detail in section 3.2.1.2). The photon energy was set to 690 eV, with an energy resolution of 0.1 eV. The Ni 3p and Sn 3d core levels were fitted using Doniach-Sunjic and Voigt line-shapes, respectively. The softwares used for the data analysis are Origin Lab.[56] and CasaXPS[57].

5.4.3 *Operando* NEXAFS characterization

The measurements were performed at the APE-HE beamline of Elettra Synchrotron in Trieste. The beamline is equipped with a proper setup designed to acquire NEXAFS spectra continuously at 1 bar, as described in detail in section 3.2.1.3. The reaction cell is directly connected to a micro gas chromatography apparatus. This allows *operando* measurements to be performed, since it is possible to monitor the gaseous products obtained from the catalytic reactions occurring inside the reaction cell. The spectra were acquired in TEY mode.

5.4.4 Micro Gas Chromatography

The *operando* NEXAFS reaction cell is equipped with an Agilent 490 Micro Gas Chromatography System with two chromatographic columns, connected to the gas-line output, with the possibility to detect the reaction products, while measuring the NEXAFS spectra. The first column is a Volamine, heated to 40 °C. It uses He as carrier gas, enabling the detection of the main products of the methanol decomposition (i.e. CO_2, CH_2O, CH_4 and H_2O). The second column is a Molecular Sieve, heated to 110 °C, with N_2 as a carrier gas, and it is used to detect H_2. The chromatograms were acquired continuously during the reaction, with a time range of 180 s.

5.4.5 High Resolution TEM

The HR-TEM measurements have been performed in collaboration with the group of Dr. Corneliu Ghica (National Institute of Materials Physics, Romania). Samples were prepared through the fine powder crushing method. The fine powder was dispersed in pure ethanol and a droplet from the liquid suspension was dripped onto a TEM grid provided with a lacey carbon membrane. For the HR-TEM investigation of the grains surface, we selected crystal grains hanging freely in the carbon membrane holes, with no membrane support underneath. The selected grains were tilted to the nearest available zone axis orientation. HR-TEM micrographs were acquired from the thinnest regions at the grain border.

5.4.6 Computational details

The calculations have been carried out by Prof. D. W. Boukhvalov (Nanjing Forestry University, College of Science). Energy cutoffs were 25 and 400 Ry for the plane-wave expansion of the wave functions and the charge density, respectively. To model the Ni_xSn_y surface, we considered the slabs constructed from $3x3x3$ supercells (Fig. 5.3). The values of the enthalpies of physisorption were calculated by the standard formula:

$$\Delta H_{phys} = [E_{host+mol} - (E_{host} + E_{mol})] \tag{5.4}$$

where E_{host} is the total energy of the surface before adsorption, and E_{mol} is the energy of a single molecule of the considered species in an empty box. In the case of water adsorption, only adsorption the gaseous phase was considered. The energy of chemical adsorption is defined as the difference between the total energy of the system after and before decomposition of physisorbed molecules on the surface. For the case of physisorption, we also evaluated the differential Gibbs free energy by the formula:

$$\Delta G = \Delta H - T\Delta S, \tag{5.5}$$

where T is the temperature and ΔS is the change of entropy of the adsorbed molecule estimated by the change of entropy in the process of gas-to-liquid transition by the standard formula:

$$\Delta S = \Delta H_{vaporisation}/T, \tag{5.6}$$

where $\Delta H_{vaporization}$ is the measured enthalpy of vaporization.

5.5 Bibliography

[1] Marc Armbrüster. Intermetallic compounds in catalysis-A versatile class of materials meets interesting challenges. *Science and Technology of Advanced Materials*, 21(1):303–322, 2020.

[2] Shinya Furukawa and Takayuki Komatsu. Intermetallic compounds: promising inorganic materials for well-structured and electronically modified reaction environments for efficient catalysis. *ACS Catalysis*, 7(1):735–765, 2017.

[3] Anish Dasgupta and Robert M Rioux. Intermetallics in catalysis: an exciting subset of multimetallic catalysts. *Catalysis Today*, 330:2–15, 2019.

[4] Vijaykumar S Marakatti and Sebastian C Peter. Synthetically tuned electronic and geometrical properties of intermetallic compounds as effective heterogeneous catalysts. *Progress in Solid State Chemistry*, 52:1–30, 2018.

[5] Marta Michalska-Domańska, Jerzy Bystrzycki, Bartłomiej Jankiewicz, and Zbigniew Bojar. Effect of the grain diameter of Ni-based catalysts on their catalytic properties in the thermocatalytic decomposition of methanol. *Comptes Rendus Chimie*, 20(2):156–163, 2017.

[6] AP Tsai, S Kameoka, K Nozawa, M Shimoda, and Y Ishii. Intermetallic: a pseudoelement for catalysis. *Accounts of Chemical Research*, 50(12):2879–2885, 2017.

[7] Marc Armbrüster, Robert Schlögl, and Yuri Grin. Intermetallic compounds in heterogeneous catalysis—a quickly developing field. *Science and Technology of Advanced Materials*, 2014.

[8] Ayumu Onda, Takayuki Komatsu, and Tatsuaki Yashima. Characterization and catalytic properties of Ni-Sn intermetallic compounds in acetylene hydrogenation. *Physical Chemistry Chemical Physics*, 2(13):2999–3005, 2000.

[9] Meiqiang Fan, Ya Xu, Junya Sakurai, Masahiko Demura, Toshiyuki Hirano, Yuden Teraoka, and Akitaka Yoshigoe. Catalytic performance of Ni_3Sn and Ni_3Sn_2 for hydrogen production from methanol decomposition. *Catalysis letters*, 144(5):843–849, 2014.

[10] H Kohlmann. Encyclopedia of physical science and technology. *San Diego, CA: Academic*, pages 441–458, 2002.

[11] Raney Murray. Process of producing nickel catalysts, March 28 1961. US Patent 2,977,327.

[12] Simon Penner and Marc Armbrüster. Formation of intermetallic compounds by reactive metal-support interaction: a frequently encountered phenomenon in catalysis. *ChemCatChem*, 7(3):374–392, 2015.

[13] VCH Kroll, HM Swaan, and C Mirodatos. Methane reforming reaction with carbon dioxide over Ni/SiO_2 Catalyst: I. Deactivation studies. *Journal of Catalysis*, 161(1):409–422, 1996.

[14] Stefan Ewald, Michael Kolbeck, Tim Kratky, Moritz Wolf, and Olaf Hinrichsen. On the deactivation of Ni-Al catalysts in CO_2 methanation. *Applied Catalysis A: General*, 570:376–386, 2019.

[15] M El Doukkali, A Iriondo, JF Cambra, I Gandarias, L Jalowiecki-Duhamel, Franck Dumeignil, and PL Arias. Deactivation study of the Pt and/or Ni-based γ Al_2O_3 catalysts used in the aqueous phase reforming of glycerol for H_2 production. *Applied Catalysis A: General*, 472:80–91, 2014.

[16] Carolina Montero, Aingeru Remiro, Beatriz Valle, Lide Oar-Arteta, Javier Bilbao, and Ana G Gayubo. Origin and nature of coke in ethanol steam reforming and its role in deactivation of Ni/La_2O_3-αAl_2O_3 catalyst. *Industrial & Engineering Chemistry Research*, 58(32):14736–14751, 2019.

[17] De Chen, Rune Lødeng, Arne Anundskås, Ola Olsvik, and Anders Holmen. Deactivation during carbon dioxide reforming of methane over Ni catalyst: microkinetic analysis. *Chemical Engineering Science*, 56(4):1371–1379, 2001.

[18] MA Vannice and RL Garten. Metal-support effects on the activity and selectivity of Ni catalysts in COH_2 synthesis reactions. *Journal of Catalysis*, 56(2):236–248, 1979.

[19] Shohei Tada, Teruyuki Shimizu, Hiromichi Kameyama, Takahide Haneda, and Ryuji Kikuchi. Ni/CeO_2 catalysts with high CO_2 methanation activity and high CH_4 selectivity at low temperatures. *International Journal of Hydrogen Energy*, 37(7):5527–5531, 2012.

[20] Lea R Winter, Elaine Gomez, Binhang Yan, Siyu Yao, and Jingguang G Chen. Tuning Ni-catalyzed CO_2 hydrogenation selectivity via Ni-ceria support interactions and Ni-Fe bimetallic formation. *Applied Catalysis B: Environmental*, 224:442–450, 2018.

[21] Sofia A Khromova, Andrey A Smirnov, Olga A Bulavchenko, Andrey A Saraev, Vasiliy V Kaichev, Sergey I Reshetnikov, and Vadim A Yakovlev. Anisole hydrodeoxygenation over Ni-Cu bimetallic catalysts: The effect of Ni/Cu ratio on selectivity. *Applied Catalysis A: General*, 470:261–270, 2014.

[22] Blaise Bridier and Javier Perez-Ramirez. Cooperative effects in ternary Cu-Ni- Fe catalysts lead to enhanced alkene selectivity in alkyne hydrogenation. *Journal of the American Chemical Society*, 132(12):4321–4327, 2010.

[23] G. W. Huber, J. W. Shabaker, and J. A. Dumesic. Raney Ni-Sn Catalyst for H_2 Production from Biomass-Derived Hydrocarbons. *Science*, 300(5628):2075–2077, 2003.

[24] A. Penkova, L. Bobadilla, S. Ivanova, M.I. Domínguez, F. Romero-Sarria, A.C. Roger, M.A. Centeno, and J.A. Odriozola. Hydrogen production by

methanol steam reforming on $NiSn/MgO - Al_2O_3$ catalysts: The role of MgO addition. *Applied Catalysis A: General*, 392(1):184–191, 2011.

[25] L.F. Bobadilla, A. Penkova, F. Romero-Sarria, M.A. Centeno, and J.A. Odriozola. Influence of the acid–base properties over $NiSn/MgO - Al_2O_3$ catalysts in the hydrogen production from glycerol steam reforming. *International Journal of Hydrogen Energy*, 39(11):5704–5712, 2014.

[26] J.W. Shabaker, D.A. Simonetti, R.D. Cortright, and J.A. Dumesic. Sn-modified Ni catalysts for aqueous-phase reforming: Characterization and deactivation studies. *Journal of Catalysis*, 231(1):67–76, 2005.

[27] L.F. Bobadilla, F. Romero-Sarria, M.A. Centeno, and J.A. Odriozola. Promoting effect of Sn on supported Ni catalyst during steam reforming of glycerol. *International Journal of Hydrogen Energy*, 41(22):9234–9244, 2016.

[28] Luis F Bobadilla, Lola Azancot, Svetlana Ivanova, Juan J Delgado, Francisca Romero-Sarria, Miguel A Centeno, Anne-Cécile Roger, and José A Odriozola. In Situ DRIFTS-MS Methanol Adsorption Study onto Supported NiSn Nanoparticles: Mechanistic Implications in Methanol Steam Reforming. *Nanomaterials*, 11(12):3234, 2021.

[29] Meiqiang Fan, Ya Xu, Junya Sakurai, Masahiko Demura, Toshiyuki Hirano, Yuden Teraoka, and Akitaka Yoshigoe. Spontaneous activation behavior of Ni_3Sn, an intermetallic catalyst, for hydrogen production via methanol decomposition. *International Journal of Hydrogen Energy*, 40(37):12663–12673, 2015.

[30] Ya Xu, Huixin Jin, Toshiyuki Hirano, Yoshitaka Matsushita, and Jianxin Zhang. Characterization of Ni_3Sn intermetallic nanoparticles fabricated by thermal plasma process and catalytic properties for methanol decomposition. *Science and Technology of Advanced Materials*, 20(1):622–631, 2019.

[31] Luca Braglia, Martina Fracchia, Paolo Ghigna, Alessandro Minguzzi, Daniela Meroni, Raju Edla, Matthias Vandichel, Elisabet Ahlberg, Giuseppina Cerrato, and Piero Torelli. Understanding Solid–Gas Reaction Mechanisms by Operando Soft X-Ray Absorption Spectroscopy at Ambient Pressure. *The Journal of Physical Chemistry C*, 124(26):14202–14212, 2020.

[32] Liping Zhong, Mathias Barreau, Valérie Caps, Vasiliki Papaefthimiou, Michael Haevecker, Detre Teschner, Walid Baaziz, Elisa Borfecchia, Luca Braglia, and Spyridon Zafeiratos. Improving the catalytic performance of cobalt for CO preferential oxidation by stabilizing the active phase through vanadium promotion. *ACS Catalysis*, 11(9):5369–5385, 2021.

[33] Paolo Giannozzi, Stefano Baroni, Nicola Bonini, Matteo Calandra, Roberto Car, Carlo Cavazzoni, Davide Ceresoli, Guido L Chiarotti, Matteo Cococcioni, Ismaila Dabo, et al. QUANTUM ESPRESSO: a modular and open-source software project for quantum simulations of materials. *Journal of physics: Condensed matter*, 21(39):395502, 2009.

[34] John P. Perdew, Kieron Burke, and Matthias Ernzerhof. Generalized Gradient Approximation Made Simple. *Phys. Rev. Lett.*, 77:3865–3868, Oct 1996.

[35] John P. Perdew, Kieron Burke, and Matthias Ernzerhof. Generalized Gradient Approximation Made Simple. *Phys. Rev. Lett.*, 77:3865–3868, Oct 1996.

[36] A. N. Mansour. Nickel Monochromated Al K XPS Spectra from the Physical Electronics Model 5400 Spectrometer. *Surface Science Spectra*, 3(3):221–230, 1994.

[37] S Hüfner and GK Wertheim. Systematics of core line asymmetries in XPS spectra of Ni. *Physics Letters A*, 51(5):301–303, 1975.

[38] JJ Yeh. Atomic Calculation of Photoionization Cross-Section and Asymmetry Parameters Gordon and Breach Science Publishers. *Langhorne, PE (USA)*, 1993.

[39] JJ Yeh and I Lindau. Atomic subshell photoionization cross sections and asymmetry parameters: $1 < Z < 10^3$. *Atomic data and nuclear data tables*, 32(1):1–155, 1985.

[40] Sergio D'Addato, V Grillo, Salvatore Altieri, R Tondi, Sergio Valeri, and Stefano Frabboni. Structure and stability of nickel/nickel oxide core-shell nanoparticles. *Journal of Physics: Condensed Matter*, 23(17):175003, 2011.

[41] Geoffrey C Allen, Philip M Tucker, and Robert K Wild. Surface oxidation of nickel metal as studied by X-Ray Photoelectron Spectroscopy. *Oxidation of Metals*, 13(3):223–236, 1979.

[42] Michael A Stranick and Anthony Moskwa. SnO by XPS. *Surface Science Spectra*, 2(1):45–49, 1993.

[43] Jill Chastain and Roger C King Jr. Handbook of X-Ray Photoelectron Spectroscopy. *Perkin-Elmer Corporation*, 40:221, 1992.

[44] Davide Barreca, Simona Garon, Eugenio Tondello, and Pierino Zanella. SnO_2 nanocrystalline thin films by XPS. *Surface Science Spectra*, 7(2):81–85, 2000.

[45] Michael A Stranick and Anthony Moskwa. SnO_2 by XPS. *Surface Science Spectra*, 2(1):50–54, 1993.

[46] YT Law, T Dintzer, and S Zafeiratos. Surface oxidation of NiCo alloy: A comparative X-Ray Photoelectron Spectroscopy study in a wide pressure range. *Applied surface science*, 258(4):1480–1487, 2011.

[47] A Politano, M Caputo, A Goldoni, P Torelli, and G Chiarello. Segregation and Selective Oxidation of Ni Atoms in $Pt_3Ni(111)$ in a Low-Pressure Oxygen

Environment. *The Journal of Physical Chemistry C*, 117(51):27007–27011, 2013.

[48] Spiros Zafeiratos, Simone Piccinin, and Detre Teschner. Alloys in catalysis: phase separation and surface segregation phenomena in response to the reactive environment. *Catalysis Science & Technology*, 2(9):1787–1801, 2012.

[49] AN Mansour. Characterization of NiO by XPS. *Surface Science Spectra*, 3(3):231–238, 1994.

[50] AN Mansour and CA Melendres. Characterization of slightly hydrated $Ni(OH)_2$ by XPS. *Surface Science Spectra*, 3(3):247–254, 1994.

[51] AN Mansour and CA Melendres. Characterization of electrochemically prepared γ-NiOOH by XPS. *Surface Science Spectra*, 3(3):271–278, 1994.

[52] I Lindau and WE Spicer. The probing depth in photoemission and Auger-electron spectroscopy. *Journal of Electron Spectroscopy and Related Phenomena*, 3(5):409–413, 1974.

[53] R. D. Leapman, L. A. Grunes, and P. L. Fejes. Study of the L_{23} edges in the $3d$ transition metals and their oxides by electron-energy-loss spectroscopy with comparisons to theory. *Phys. Rev. B*, 26:614–635, Jul 1982.

[54] M. Barreau, D. Chen, J. Zhang, V. Papaefthimiou, C. Petit, D. Salusso, E. Borfecchia, S. Turczyniak-Surdacka, K. Sobczak, S. Mauri, L. Braglia, P. Torelli, and S. Zafeiratos. Synthesis of Ni-doped ceria nanoparticles and their unusual surface reduction in hydrogen. *Materials Today Chemistry*, 26:101011, 2022.

[55] Pan Wei, Lingtong Zhou, Wei Xia, Zhujian Li, Haifei Long, Jindan Chen, Ting Li, and Mei Qiang Fan. Catalytic Performance of Oxidized Ni_3Sn_2 for Hydrogen Production from Methanol Decomposition. *Journal of New Materials for Electrochemical Systems*, 17(4), 2014.

[56] Origin(pro), Version 2020. OriginLab Corporation, Northampton, MA, USA.

[57] Neal Fairley, Vincent Fernandez, Mireille Richard-Plouet, Catherine Guillot-Deudon, John Walton, Emily Smith, Delphine Flahaut, Mark Greiner, Mark Biesinger, Sven Tougaard, et al. Systematic and collaborative approach to problem solving using X-Ray Photoelectron spectroscopy. *Applied Surface Science Advances*, 5:100112, 2021.

Chapter 6

Conclusions and Perspectives

In this thesis work we illustrated the potentialities of using a *knowledge-based* approach in order to speed up the optimization of heterogeneous catalysts, in the optic of the imminent global energetic transition. To this purpose, we reported the promising results obtained by exploiting the *operando* Soft X-Rays NEXAFS spectroscopy at ambient pressure, an innovative technique available at APE-HE beamline of Elettra Synchrotron (Trieste). In order to extract the maximum of its potential, it was combined with other *in situ* spectroscopies and the results were supported by computational simulations. Exploiting this approach, we managed to directly monitor the catalysts surface electronic structure modifications at the real operating conditions, thus being able to elucidate the catalytic mechanism. As shown in Fig.6.1, this PhD project was focused on methanol valorization, in the perspective of a future possible methanol-based economy, that would be extremely convenient from an economic and environmental point of view. In the figure, we highlighted with red boxes the steps that have been carried out successfully in order to investigate catalytic methanol production and decomposition on different catalysts. As it can be observed, almost an entire iteration of the *knowledge-based* scheme has been performed in both cases. The missing step, marked in blue, is referred to the catalytic quantitative tests, that can be conducted separately in order to complete an entire iteration.

The main conclusions that can be drawn from the investigation of the direct partial oxidation of methane to methanol on a CeO_2/CuO catalyst, schematized in the top part of the figure, are the result of a successful combination of the *operando* NEXAFS and the *in situ* DRIFT spectroscopies. This multitechnique approach allowed to obtain a clear vision of the catalytic mechanism occurring on the surface of the catalyst, synthesized using a scalable and solvent free ball milling process. Combining the spectroscopic results we discovered the specificity of the synthetic method employed, through which peculiar interfaces between the two oxides are formed due to charge transfers phenomena induced by the mechanochemical energy provided during the synthesis. These active sites have shown to be able to promote the catalytic partial oxidation of methane. This study highlights how the use of conventional *ex situ* characterization techniques alone would not have allowed to discover the presence of the synthesis-specific active species in the ball milled catalyst with respect to a similar conventional impregnated CeO_2/CuO sample. Indeed, the *operando* and *in situ* spectroscopies allowed to detect reversible modifications at the catalyst surface, that after the reaction is totally restored. The findings of this study open up the perspective of ball milled mixed-oxides catalysts optimization for a future large-scale utilization: this could be done by trying to maximize the content of the peculiar catalyst active sites, by modifying the synthesis parameters or intervening on the precursors surface area.

For what concerns the investigation of the catalytic methanol decomposition to syngas catalysed by Ni-Sn intermetallic compounds, schematized in the bottom part of Fig.6.1, we exploited the *operando* NEXAFS technique coupled with the *in situ* XPS in order to evaluate the effect of Sn incorporation on the reaction selectivity. The possibility to detect the gas products while measuring the NEXAFS spectra during the reaction, coupled with surface reactivity XPS studies, allowed to discover a pivotal role of naturally formed tin-oxide skin in directing the re-

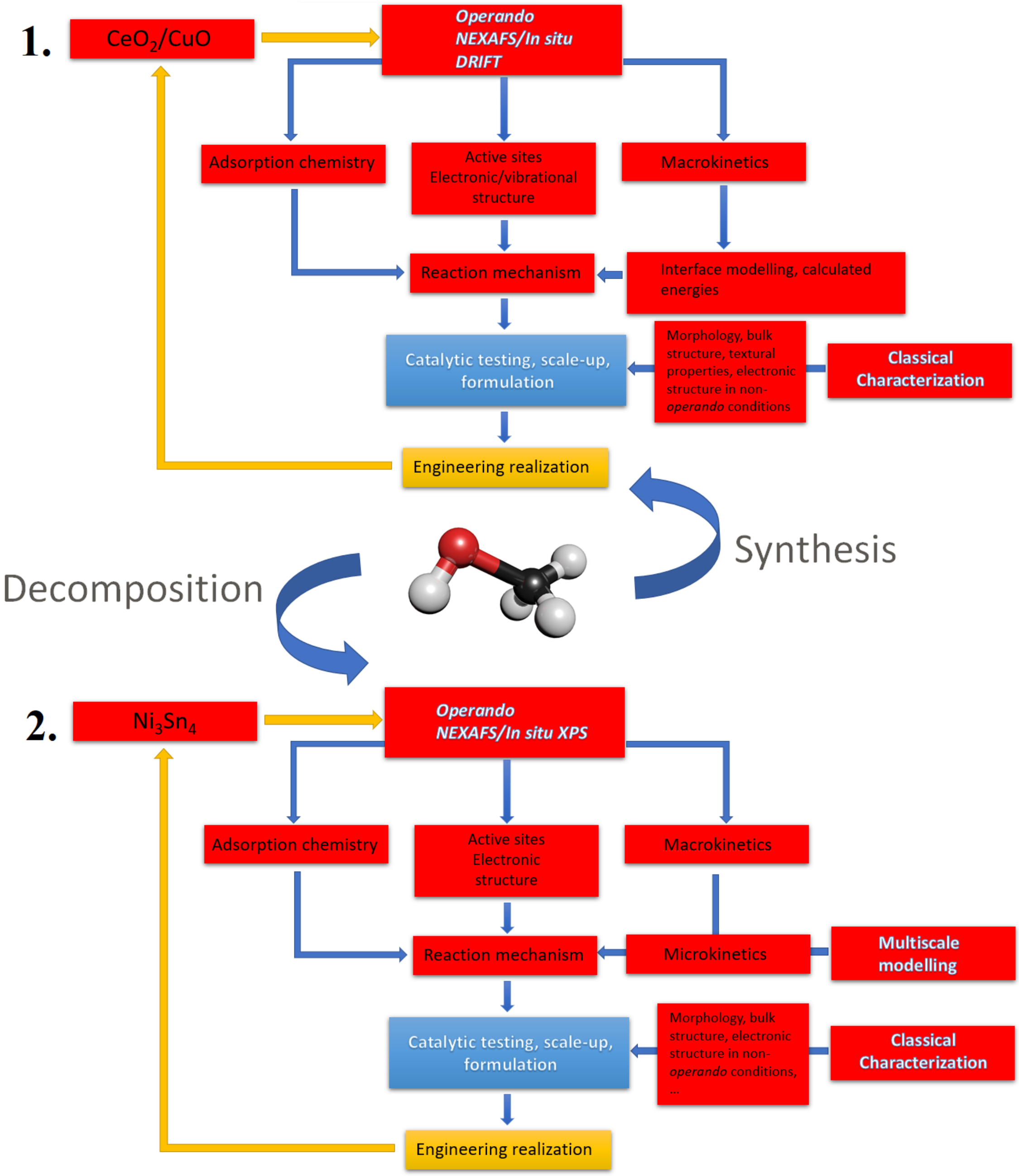

Figure 6.1: Graphic summary of the studies carried out in this thesis work, in the context of a *knowledge-based* approach. 1: Inverse ball milled $CeO_2 - CuO$ catalyst for partial oxidation of methane: a combined *in-situ* DRIFT/*operando* NEXAFS investigation. 2: Hydrogen Production Mechanism in Low-Temperature Methanol Decomposition Catalyzed by Ni_3Sn_4 Intermetallic Compound: A Combined Operando and Density Functional Theory Investigation. Center: ball and stick representation of methanol, whose valorization was the thread of the thesis.

action towards hydrogen production at low temperatures (250 °C), suppressing secondary undesired reactions and thus increasing the catalyst selectivity. The effect is further enhanced increasing the stoichiometric amount of Sn in the intermetallic catalyst. Also in this case, this molecular-oriented approach, validated by DFT calculations, allowed to direct the next step for the catalyst optimization, that could be the synthesis of supported $Ni - Sn$ nanoparticles in order to maximize the surface reactive area and exploit/address the role of the SMSI.

Given the important results obtained during this thesis project, the perspective of future instrumental implementations is natural. For example, we highlighted the great potentialities of combining *operando* NEXAFS and *in situ* DRIFT spectroscopies: although the measurements have been conducted under the same experimental conditions and gave strongly correlated results, they have been performed separately. The possibility to develop an experimental setup able to perform at the same time NEXAFS and DRIFT spectroscopy would give a great added value to the final results. Another possible perspective of instrumental development could be an *operando* NEXAFS reaction cell adapting in order to open the possibility to perform quantitative catalytic tests while measuring the spectroscopic modifications on the catalyst surface. These instrumental improvements would allow to further speed up the characterization of the catalysts reported in the knowledge-based schemes of Fig.6.1, drastically reducing the number of boxes (i.e. the number of experiments to be conducted). In conclusion, being an extremely new technique, the road that must be followed for the optimization of the *operando* Soft X-Rays NEXAFS spectroscopy is still long, but the results it has given so far confirm it as one of the most effective and informative for the study of reaction mechanisms occurring on the surface of heterogenous catalysts.

Acknowledgements

First of all, I would like to thank Professor Giorgio Rossi, coordinator of NFFA Trieste project, for giving me the opportunity to carry out my doctorate in a context of scientific excellence, where the possibility of exploiting advanced instruments has certainly contributed to the success of the works published during the three years. For the same reason, I also thank Elettra Sincrotrone and the CNR-IOM.

Given my academic formation as a computational chemist, starting this journey on the APE-HE beamline was a so-called "leap into the void" for me. I had practically never entered a physics laboratory. These premises lead me to especially thank my supervisor Dr. Piero Torelli, who supported me right from the start, without ever giving the impression of doubting my abilities. The thing I'm most grateful to him for, besides offering me the opportunity to work in an international and scientifically cutting-edge environment, was that he made me grow professionally and personally, instilling in me a level of self-esteem that I never managed to reach, having always been a very insecure person. He managed to do it by always pushing me to give my best, trusting me and assigning me responsibilities that sometimes even exceeded my role, but the results of which made me proud. Furthermore, I am grateful to him for having given me almost total freedom in choosing the research topic to be carried out, and I don't think this is so usual for a doctoral thesis. From a scientific point of view, I never thought I would learn so much in three years, and for this I am grateful to Dr. Luca Braglia who has followed me daily, teaching me with great patience how to work on a beamline, the right approach to perform the experiments, how to analyze data, but also how to interact with users, how to deal with the infinite problems related to work with home-made experimental

setups. More than anything else, I thank him for teaching me that a solution is always possible and most of the time at hand, even when everything seems to go wrong. Although not working closely with me, for the same reasons I would like to thank Dr. Giovanni Vinai, Vincent Polewczyk and "Sasha" Petrov, who have always helped me when I needed it, giving me precious teachings. In particular Vincent, who further contributed to increase my self-confidence. I was lucky enough to work in a young, close-knit research group, a real team where everyone helps each other without competing. For this reason I would like to thank all the people who are part of it, in particular the group that works with the high pressure cell: Andrea Fondacaro, Federico Salvador, Ferdinando Bassato, Sara Stolfi and Mario Rivera.

I would also like to thank all the professors and researchers with whom I have collaborated over the years (they are too many to make a complete list). In particular, Prof. Paola D'Angelo, who welcomed me into her research group for a month, providing me valuable teachings, with the added value of enjoying the beauty of living in Rome. Furthermore, I thank Prof. Alessandro Trovarelli and Prof. Antonio Politano, with whom we have established solid collaborations, allowing us to successfully complete the two studies presented in this research project.

A few lines of these long acknowledgements are for Rudy, my life partner, who has been fundamental for this thesis work, on a professional and obviously human level. We have done a wonderful job together, and this makes me even more proud of the results achieved.

I thank my best friends for helping me to live these three years peacefully, encouraging me in the moments of greatest stress and anxiety, and also my brother, who despite living far from here has always been close to me.

Finally, I want to dedicate this thesis work to my parents, because it is mainly thanks to them that I have managed to achieve this goal, teaching me since I was a child the values of perseverance, commitment and knowledge.

Ringraziamenti

Desidero ringraziare innanzitutto il Prof. Giorgio Rossi, coordinatore del progetto NFFA Trieste, per avermi dato la possibilità di svolgere il dottorato in un contesto di eccellenza scientifica, dove la possibilità di sfruttare strumentazioni all'avanguardia ha sicuramente contribuito al successo dei lavori pubblicati durante i tre anni. Per lo stesso motivo, ringrazio anche Elettra Sincrotrone ed il CNR-IOM.

Vista la mia formazione in ambito chimico computazionale, iniziare questo percorso sulla beamline APE-HE per me è stato un cosiddetto "salto nel vuoto". Non avevo praticamente mai messo piede in un laboratorio di fisica. Queste premesse mi portano a ringraziare in particolar modo il Dr. Piero Torelli, che in qualità di supervisore mi ha sostenuta fin dall'inizio, senza mai dare l'impressione di dubitare delle mie capacità. La cosa di cui gli sono più grata, oltre offrirmi la possibilità di lavorare in un ambiente di eccellenza, internazionale e all'avanguardia, è stata l'avermi fatta crescere a livello professionale e personale, infondendomi un livello di sicurezza e autostima che non ero mai riuscita a raggiungere, essendo da sempre una persona molto insicura. L'ha fatto spronandomi sempre a dare il massimo, dandomi fiducia e assegnandomi delle responsabilità a volte anche superiori al mio ruolo, ma i cui risultati mi hanno resa orgogliosa. Inoltre, gli sono grata per avermi dato la quasi totale libertà nello scegliere il tema della ricerca da portare avanti, e questo non credo sia così usuale per una tesi di dottorato. Dal punto di vista scientifico non avrei mai pensato di imparare così tanto in tre anni, e per questo sono grata al Dr. Luca Braglia che mi ha seguita quotidianamente insegnandomi con grande pazienza come si lavora su una beamline, l'approccio con cui condurre gli esperimenti, come analizzare i dati, ma anche come interagire con gli utenti, come affrontare gli infiniti problemi legati al lavorare con degli strumenti non convenzionali. Più di ogni altra cosa, lo ringrazio per avermi insegnato che una soluzione è sempre possibile ed il più delle volte a portata di mano, anche quando tutto sembra andare storto.

Pur non lavorando a stretto contatto con me, per gli stessi motivi mi sento di ringraziare i Dr. Giovanni Vinai, Vincent Polewczyk e "Sasha" Petrov, che mi hanno sempre aiutata nei momenti di necessità, dandomi preziosi insegnamenti. In particolare

Vincent, che ha contribuito ulteriormente a farmi avere più fiducia in me stessa. Ho avuto la fortuna di lavorare in un gruppo di ricerca giovane, affiatato, un vero team in cui tutti si aiutano l'un l'altro senza competere. Per questo mi sento di ringraziare tutte le persone che ne fanno parte, in particolare il gruppo che lavora con la cella ad alta pressione: Andrea Fondacaro, Federico Salvador, Ferdinando Bassato, Sara Stolfi e Mario Rivera.

Vorrei ringraziare anche tutti i professori ed i ricercatori con cui ho collaborato in questi anni (sono troppi per fare una lista completa). In particolare, la Prof. Paola D'Angelo, che mi ha accolta nel suo gruppo di ricerca per un mese, fornendomi preziosi insegnamenti, con il valore aggiunto di poter assaporare la bellezza di vivere a Roma. Inoltre ringrazio il prof. Alessandro Trovarelli ed il prof. Antonio Politano, con i quali abbiamo instaurato delle solide collaborazioni che hanno permesso di portare a termine con successo i due studi presentati in questo progetto di ricerca.

Qualche riga di questi lunghi ringraziamenti è per Rudy, il mio compagno di vita, che per questo lavoro di tesi è stato fondamentale sia a livello professionale che ovviamente umano. Abbiamo fatto un lavoro bellissimo insieme, e questo mi rende ancora più orgogliosa dei risultati raggiunti.

Ringrazio i miei amici di sempre per avermi fatto vivere serenamente questi tre anni, aiutandomi nei momenti di maggiore stress e ansia, e anche il mio fratellino, che pur vivendo lontano da qui, mi è sempre stato vicino.

Infine, dedico questa tesi ai miei genitori, perchè è soprattutto grazie a loro che sono riuscita a raggiungere questo obiettivo, insegnandomi fin da piccola il valore della costanza, dell'impegno e della conoscenza.

List of publications

1. **Mauri, S.**; Calligaro, R.; Braglia, L.; Boaro, M.; Trovarelli, A.; Torelli, P. **Low temperature methane activation over mechanochemical-induced Ce(IV)/Cu(I) interface: an *in situ* DRIFT / *operando* NEXAFS study.** *In preparation*
2. **Mauri, S.**; D'Olimpio, G.; Ghica, C.; Braglia, L.; Kuo, C.N.; Istrate, M.C.; Lue, C.S.; Ottaviano, L.; Klimczuk, T.; Boukhvalov, D.W.; Politano, A.; Torelli, P. **Hydrogen Production Mechanism in Low-Temperature Methanol Decomposition Catalyzed by Ni_3Sn_4 Intermetallic Compound: A Combined Operando and Density Functional Theory Investigation.** *Accepted in Journal of Physical Chemistry Letters.* DOI: 10.1021/acs.jpclett.2c03471.
3. Salusso, D.; **Mauri, S.**; Deplano, G.; Torelli, P.; Bordiga, S.; Rojas Buzo, S. **MOF-Derived CeO_2 and $CeZrO_x$ Solid Solutions: Exploring Ce Reduction through FTIR and NEXAFS Spectroscopy.** *Nanomaterials* 2023, 13(2), 272. `https://doi.org/10.3390/nano13020272.`
4. Barreau, M.; Chen, D.; Zhang, J.; Papaefthimiou, V.; Petit, C.; Salusso, D.; Borfecchia, E.; Turczyniak-Surdacka S.; Sobczak, K.; **Mauri, S.**; Braglia, L.; Torelli, P.; Zafeiratos, S. **Synthesis of Ni-doped ceria nanoparticles and their unusual surface reduction in hydrogen.** *Mater. today Chem.* 2022, 26, 101011, ISSN 2468-5194. `https://doi.org/10.1016/j.mtchem.2022.101011.`
5. Tavani, F.; Busato, M.; Braglia, L.; **Mauri, S.**; Torelli, P.; D'angelo P. **Caught while Dissolving: Revealing the Interfacial Solvation of the Mg^{2+} Ions on the MgO Surface.** *ACS Appl. Energy Mater.* 2022, 14, 33, 38370–38378. `https://doi.org/10.1021/acsami.2c10005.`

6. Felli, A.; **Mauri, S.**; Marelli M.; Torelli P.; Trovarelli A.; Boaro M. **Insights into the Redox Behavior of $\mathbf{Pr_{0.5}Ba_{0.5}MnO_{3-\delta}}$ Derived Perovskites for $\mathbf{CO_2}$ Valorization Technologies.** *ACS Appl. Energy Mater.* 2022, 5, 6, 6687–6699. `https://doi.org/10.1021/acsaem.2c00163`.

7. Toffoli, D.; Bernes, E.; Cossaro, A.; Balducci, G.; Stener, M.; **Mauri, S.**; Fronzoni, G. **Computational NEXAFS Characterization of Molecular Model Systems for 2D Boroxine Frameworks.** *Nanomaterials* 2022, 12, 1610. `https://doi.org/10.3390/nano12091610`.

8. Celeste, A.; Brescia, R.; Greco, G.; Torelli, P.; **Mauri, S.**; Silvestri L.; Pellegrini, V.; Brutti, S. **Pushing Stoichiometries of Lithium-Rich Layered Oxides Beyond Their Limits.** *ACS Appl. Energy Mater.* 2022, 5, 2, 1905–1913. `https://doi.org/10.1021/acsaem.1c03396`.

9. Braglia, L.; Tavani, F.; **Mauri, S.**; Edla, R.; Krizmancic, D.; Tofoni, A.; Colombo, V.; D'Angelo, P.; Torelli, P. **Catching the Reversible Formation and Reactivity of Surface Defective Sites in Metal–Organic Frameworks: An Operando Ambient Pressure-NEXAFS Investigation.** *J. Phys. Chem. Lett.* 2021, 12, 37, 9182–9187. `https://doi.org/10.1021/acs.jpclett.1c02585`.

10. Boukhvalov, D. W.; Kuo, C. N.; Nappini, S.; Marchionni, A.; D'Olimpio, G.; Filippi, J.; **Mauri, S.**; Torelli, P.; Shan Lue, C. S.; Vizza, F.; Politano, A. **Efficient Electrochemical Water Splitting with PdSn4 Dirac Nodal Arc Semimetal.** *ACS Catal.* 2021, 11, 12, 7311–7318. `https://doi.org/10.1021/acscatal.1c01653`.

"Deep rivers run quiet."

Haruki Murakami

Hard-Boiled Wonderland and the
End of the World